TIO2 THIN FILMS BY APCVD FOR PHOTOCATALYTIC APPLICATIONS

NANYANG TECHNOLOGICAL UNIVERSITY

TIO2 THIN FILMS BY APCVD FOR PHOTOCATALYTIC APPLICATIONS

CHUA CHIN SHENG

SCHOOL OF ELECTRICAL & ELECTRONIC ENGINEERING

2013

CHUA CHIN SHENG 2013

TiO_2 Thin Films by APCVD for Photocatalytic Applications

Chua Chin Sheng

School of Electrical & Electronics Engineering

A thesis submitted to the Nanyang Technological University

in partial fulfillment of the requirement for the degree of

Doctor of Philosophy

2013

Acknowledgements

I would like to express my deepest gratitude to my supervisor, Prof. Tan Ooi Kiang, for his encouragement, supervision and support to my PhD thesis. His critical comments and thoughtful insights have helped to enrich the content of this report. I am also grateful towards Prof. Tse Man Siu for his advice on the modification of my deposition system and experimental setup.

Also, I would like to extend my appreciation to my co-supervisors from SIMTech, Dr. Andrew Soutar and Ding Xing Zhao, for their useful discussion and patient guidance. Their comments have helped smoothened the path in my research.

I am grateful to Dr. Chen Xiaofeng for his advice, Dr. Huang Hui for his useful suggestions and Dr. Fang Xiaoqin for her help on XPS analysis. I gratefully acknowledge my friends in Sensor and Actuator Lab, Ms Tan Peiyun, Dr. Mohammad Ghaffari, Mr Chow Chee Lap, Mr Lim Chiew Keat, Ms Leiw Ming Yian, Ms Zhang Li, Ms Han Mandi, and Ms Luo Qiong, for their constant support for my study.

I would also like to express my sincere thanks to the technical staff Mr Chua Tong Sun, Mr Ng Yong Chiang from Sensor and Actuator Lab and Mr Anthony Yeo, Ms Ng Fern Lan, Ms Ma Cho Cho khin, Ms Mon Aye Aye, Ms Xie Hong, and Ms Liu Yu Chan for their valuable equipment support.

I would like to thank my family for the wonderful support over these years. Most importantly, I want to thank my wife, Ms Lim Sing Yee, for her unwavering support through the hardship and difficulties during my course of study.

Table of Contents

Summary

Photocatalyst has generated great interest since the discovery of water splitting with titanium dioxide (TiO_2) under UV light illumination. This technology has also been shown to be applicable in other areas such as antibacterial, indoor air quality control, water treatment and self-cleaning surface. Among the various photocatalytic materials, TiO_2 is the most popular photocatalyst owning to its good stability and high photocatalytic efficiency. In this thesis, TiO_2 coatings were deposited on soda lime glass using atmospheric pressure chemical vapor deposition (APCVD). The photocatalytic property of TiO_2 coating was successfully enhanced through embedding of particles and incorporation of dopants.

The deposition of TiO_2 films was carried out on an in-house built APCVD system where a conveyor belt system was used to improve the uniformity of the TiO_2 films. The system was capable of depositing uniform coating on a large substrate and can be scaled-up easily for industrial applications. X-ray diffraction analysis verified that the as-deposited films consisted of photocatalytic anatase phase. The photocatalytic effect was analyzed from the degradation of stearic acid where its degradation rate represented the photocatalytic effect of the films. The deposited TiO_2 films have also showed capability in degrading ethyl cellulose.

The second part of the thesis focuses on the effect of different modifications of the APCVD deposited TiO_2 films on the photocatalytic property. The first modification was carried out by annealing the films, under both conventional tube furnace annealing and rapid thermal annealing, in order to induce a partial phase transition

from anatase to rutile. A mix phase of anatase and rutile had been reported to have greater photocatalytic effect compared to pure anatase or rutile phase. In our work, however, both the annealing process resulted in a decrease of photoactivity because of the growth of grain size in the TiO_2 films and the resultant increase of electron-hole recombination sites.

The second modification was conducted by embedding photocatalytic particles into the TiO_2 films to improve the UV and visible light response of the deposited films. Some photocatalytic sensitive particles, such as anatase, rutile, P25 (commercial product from Degussa with 70% anatase and 30% rutile content) and $SrTi_{(1-x)}Fe_xO_3$, were dispersed in a solvent and sprayed onto the substrate by incorporating a modified module within the APCVD system. TiO_2 films were then coated over the particles, which act as a photocatalyst and a matrix binding the particles onto the film. Among these particle embedded TiO_2 films, P25 particles showed at least a 2 times improvement in the UV light photoactivity over plain TiO_2 films. While $SrTi_{(1-x)}Fe_xO_3$ particles was meant to improve the visible light photocatalytic effect, the formation of recombination sites and loss of oxidation power of the generated holes lead to a decrease in photoactivity under both UV and visible light illumination.

Lastly, tin dopants were incorporated into the TiO_2 films through an aerosol assisted CVD process in which a bubbler system was properly modified. An ultrasonic generator was added underneath the bubbler to generate tiny droplets of tin and titanium precursor mixture in the bubbler. The TiO_2 films, with 3.8 at.% tin, showed the greatest improvement to the UV light photocatalytic property. However, with

further increased in tin dopants, the photocatalytic property of the films declined as the dopants started to act as recombination centers. TiO_2/SnO_2 bilayer films were also deposited and tested. The existence of the SnO_2 layer promoted partial transformation from anatase to rutile phase in the top TiO_2 layer forming a heterojunction semiconductor between anatase and rutile phase. However, a gradual decrease in photoactivity was observed due to the accumulation of photogenerated electrons in the SnO_2 layer.

In summary, the methods of embedding P25 particles and tin doping had led to successful improvement in photoactivity of the TiO_2 films. The photoactivity of other modifications had been hampered by the large grain size and formation of electron hole recombination sites.

List of Figures

List of Tables

Chapter 1: Introduction

1.1 Motivation

Since the discovery of water splitting with titanium dioxide (TiO_2) electrode under UV illumination [1], photocatalysts have attracted much attention for their wide range of potential applications. These applications include hydrogen fuel production [2], indoor air quality control [3], antibacterial [4], water treatment [4] and self-cleaning [5]. Among these applications, self-cleaning has been commercialized with products such as Pilkington Activ self-cleaning glass [6] and Saint Gobain BIOCLEAN [7].

The photocatalytic effect has been observed for several decades with the chalking phenomena of titania-based paints. Under strong solar light, titania particles degrade the organic components in the paint (i.e. binder) leaving white titanium oxide powder on the paint surface. This degradation effect is caused by the absorption of photons by the titania particles. The absorbed photons generate electron-hole pairs which form $OH\cdot$ radicals and O^{2-} superoxide anions. These radicals react with organic compounds and break them down into water and carbon dioxide.

Commercial applications of photocatalyst preferably require the photocatalytic material to be attached to a substrate as loose particles so as to necessitate its recollection for repeated uses. Among the various methods of attaching photocatalytic materials on substrates (i.e. sol-gel and physical vapor deposition), Atmospheric Pressure Chemical Vapor Deposition (APCVD) is more preferred as it

can be incorporated into float glass production to produce photocatalytic glasses. This reduces the cost of production and yet deposits films of good quality. Commercial product, Pilkington Activ, was deposited using APCVD and is currently use for conservatories and windows.

For this research, the focus is to enhance the photocatalytic property of TiO_2 thin films deposited by APCVD. Various methods were investigated such as anatase-rutile heterojunction semiconductor effect, embedding $SrTi_{(1-x)}Fe_xO_3$ particles for visible light photocatalytic effect and doping tin ions into the TiO_2 films. To emulate the enhancement effect of mixed phase TiO_2 material, the anatase TiO_2 films were annealed at high temperature to purposely induce a partial phase transformation from anatase to rutile. Further studies on mixed phase TiO_2 films are carried out by embedding different particles into the TiO_2 films and deposition of undercoat SnO_2 layer to induce rutile growth. $SrTi_{(1-x)}Fe_xO_3$ particles were also embedded into the TiO_2 films for visible light photocatalytic effect while Sn^{4+} ions were doped into the TiO_2 films to improve its UV light photoactivity.

1.2 Objectives

The objectives of this project include:

1) To deposit photocatalytic TiO_2 thin films on glass substrate by APCVD.

   Photocatalytic TiO_2 are deposited on soda lime glass using the APCVD coater. The deposition parameters and films thickness are optimized to produce films with good photocatalytic property. The inclusion of a SiO_2 undercoat to reduce

sodium poisoning from the soda-lime glass is to be investigated. Photocatalytic property of the deposited films are confirmed through the degradation of 2 contaminants; stearic acid and ethyl cellulose.

2) To investigate the effect of mixed rutile and anatase phase TiO_2 thin films through thermal annealing

   TiO_2 thin films, deposited on quartz, are annealed to initiate a phase transition from anatase to rutile. Mixed phase TiO_2, such as Degussa P25, has been proven to have better photocatalytic properties [8]. The effects of mixed phase TiO_2 films on the photocatalytic property are investigated. The annealing of TiO_2 films is to be carried out using conventional tube furnace and rapid thermal annealing.

3) To embed particles in TiO_2 matrix and studied its effects on the photocatalytic property of the films.

   Particles are embedded into the TiO_2 matrix to investigate its effect on the photocatalytic property. A spray nozzle is incorporated into the APCVD system for spraying particle dispersion onto the substrate surface. TiO_2 films are coated over the particles to act as a matrix. Different particles such as anatase, rutile, P25 and $SrTi_{(1-x)}Fe_xO_3$ particles are embedded into the TiO_2 films. The effects of embedded these particles on the UV and visible light photoactivity are investigated.

4) To investigate the effects of incorporating tin dopants on the photocatalytic property of the TiO_2 films.

Tin dopants are incorporated into TiO_2 films through Aerosol Assisted Chemical Vapor Deposition (AACVD). The bubbler of APCVD system is modified and incorporated with an aerosol generator. Through generation of tiny droplets, tin-doped TiO_2 films are deposited. The effect of tin dopants on the absorption spectrum, surface topography and photocatalytic is investigated.

5) To investigate photocatalytic property of a bilayer TiO_2/SnO_2 films.

Bilayer TiO_2/SnO_2 films are deposited to induce formation of rutile phase in TiO_2 films. The effect of SnO_2 underlayer to the crystallinity and photocatalytic property of TiO_2 films are studied.

1.3 Major Contributions

The major contributions of this thesis are as follows:

Thin uniform TiO_2 films were successfully deposited onto soda-lime glass using SIMTech in-house built APCVD system. The anatase films showed good photocatalytic property with the degradation of stearic acid and ethyl cellulose. Further enhancement of its photoactivity was achieved through a SiO_2 barrier layer, which prevents sodium poisoning of the TiO_2 films. TiO_2 films deposited on soda lime glass pre-coated with SiO_2 barrier layer showed similar photoactivity to those deposited on sodium free quartz glass. A film thickness of 60 nm is required to achieve its maximum photoactivity.

The effect of post annealing on the photocatalytic property of TiO_2 films was studied and a mechanism was proposed for the observed detrimental effect. The

annealing treatment of TiO_2 films led to a decrease in its photoactivity at annealing temperate of >700 °C. The decrease in photoactivity occurred in 2 stages. The first stage was caused by an increase in grain size and formation of recombination sites in the annealed TiO_2 films (annealing temperature 700 to 800 °C). The second stage was due to the formation of large rutile grains which showed limited heterojunction semiconductor effect with the anatase films (annealing temperature 900 °C).

Anatase, Rutile, P25 and $SrTi_{(1-x)}Fe_xO_3$ were successfully embedded in TiO_2 films using a spray and APCVD system. For anatase, rutile and P25, the films show a particle surface coverage of more than 20% with 4 particle spray cycles. UV light photocatalytic property was shown to double with the incorporation of P25 particles in the film. Rutile particles did not show any improvement due to its large particle size. $SrTi_{(1-x)}Fe_xO_3$ particles, meant to improve the visible light photoactivity of TiO_2 film, instead cause a decrease in photoactivity under both UV and visible light. The decrease is likely to be due to lowered oxidation power and presence of recombination sites.

APCVD bubbler was modified and an aerosol generator was included to convert the APCVD system into an AACVD. With the AACVD system, tin was successfully doped into the TiO_2 film. The tin-doped TiO_2 film shows a red-shift in the UV-Vis absorption spectrum which demonstrates its capability in absorbing lower energy photons for electron-hole pair generation. At 3.8 at.% tin doping in the TiO_2 film, the photocatalytic reaction rate was found to have improved by 10%. Further increase in doping, however, leads to a reduction in photoactivity caused by recombination of electrons and holes.

Bilayer TiO_2/SnO_2 films were deposited through a combination of AACVD and APCVD. The underlying SnO_2 layer induces the formation of rutile phase in the TiO_2 layer, leading to a mix phase of anatase and rutile in the TiO_2 films. The composition of rutile phase formed ranges from 30-50%. While a red shift in the absorption spectrum was observed, the photocatalytic property of the deposited films was found to deteriorate. This deterioration is due to trapping of photogenerated electrons in the sandwich SnO_2 layer. As the decrease in photoactivity is less than the amount of rutile phase formation, it suggests possible heterojunction effect between rutile and anatase.

1.4 Organization of Report

This report is organized as follows:

Chapter 1: Introduction to photocatalytic semiconductor and its potential applications. Motivation and objective of this research are also presented.

Chapter 2: Literature review on photocatalytic oxidation mechanism, and various methods to enhance the photocatalytic property of TiO_2. This chapter also reviews on the various methods to achieve visible light photocatalytic effect and the various deposition methods for TiO_2 films. The various ways of embedding particles in APCVD deposited TiO_2 films are also discussed.

Chapter 3: Discussion on the APCVD system for deposition of TiO_2 films and modifications made to the system to deposit embedded particle films and tin-doped TiO_2 films. The various characterization tools used are outlined in this chapter.

Chapter 4: This chapter looks into the various deposition parameters for TiO_2 films with the in-house built APCVD coater. The effect of SiO_2 barrier layer and the TiO_2 film thickness is also studied. Repeatability and reproducibility of the stearic acid test is also examined.

Chapter 5: The effects of annealing (convention and rapid thermal annealing) on the photocatalytic property of TiO_2 thin films are investigated here. Annealing results in the phase transformation of anatase to rutile which affects the photocatalytic behavior of TiO_2 films.

Chapter 6: This chapter looks into embedding photocatalytic anatase, rutile, P25 and $SrTi_{(1-x)}Fe_xO_3$ particles into TiO_2 films. It looks at the effect of various embedded particles on the photocatalytic property of the films.

Chapter 7: This chapter examines the effect of Sn^{4+} dopants and SnO_2 layer on the crystallinity of TiO_2 films. The addition of Sn could induce formation of rutile phase in the TiO_2 films. Here, the effect of rutile and anatase heterojunction on the photocatalytic properties is examined.

Chapter 8: Conclusion and recommended future works.

Chapter 2: Literature review

2.1 Introduction

Photocatalysts are semiconductor materials that can degrade organic contamination under light illumination. These photocatalysts are usually metal oxides or metal sulfides. Some of the commonly studied photocatalysts include TiO_2 [9], ZnO [10], WO_3 [11], CdS [12] and ZnS [13]. The photocatalytic reaction initiates with the absorption of photons by a photocatalyst. The absorbed photons generate electron-hole pairs by exciting electrons from the valence band to the conduction band of the semiconductor. While some of electron-hole pairs would recombine to generate heat, others migrate to the surface and participate in redox reactions to form reactive radicals [14]. These reactive radicals react with the organic compound and decompose them into carbon dioxide and water. Figure 2.1 shows a graphical summary of the photocatalytic reaction. The insert shows the absorption of photons for generation of electrons and holes. Pathway A shows the recombination of electrons and holes which may occur within the bulk or on the surface of the semiconductor. Reactions B and C show the movement of electrons and holes to the surface where they participate in redox reaction to form reactive radicals.

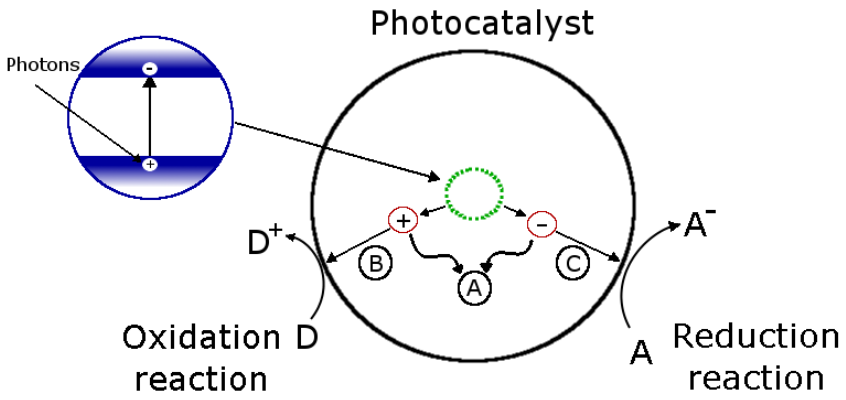

Figure 2.1 Overview of photocatalytic reaction; generation and recombination of electron-hole pair and redox reactions.

Equations 2-1 to 2-7 show the chemical reactions occurring on the photocatalyst surface with the photogenerated electrons and holes [15]. Holes react with hydroxyl ions and absorb water molecules to form hydroxyl radicals (equations 2-1 and 2-2). Electrons, on the other hand, reduce absorbed oxygen molecules and form superoxide anions, O_2^- (equation 2-3). The superoxide anion reacts with absorbed hydrogen ions to form HO_2•, which undergoes further reaction to form hydrogen peroxide. Under UV illumination, the hydrogen peroxide splits into two OH• radicals through photolysis in equation 2-6. With the formation of these reactive radicals, OH• (equations 2-1, 2-2 and 2-6) and HO_2• (equation 2-4), the organic contamination found on the surface of the photocatalyst, are decomposed into carbon dioxide and water. The overall reaction for the decomposition of the contamination is shown in equation 2-7.

$$h^+ + H_2O_{ad} \rightarrow OH\bullet + H^+ \qquad (2\text{-}1)$$

$$h^+ + OH_{ad}^- \rightarrow OH_{ad}\bullet \qquad (2\text{-}2)$$

$e^- + O_2 \rightarrow O_2^-$ (2-3)

$O_2^- + H^+ \rightarrow HO_2\bullet$ (2-4)

$H^+ + O_2^- + HO_2\bullet \rightarrow H_2O_2 + O_2$ (2-5)

$H_2O_2 + hv \rightarrow 2OH_{ad}\bullet$ (2-6)

Organic material $+O_2$ **Error! Objects cannot be created from editing field codes.**

$CO_2 + H_2O$ + mineral acids (2-7)

The main consideration of a good photocatalyst is its bandgap energy, potential of conduction and valence band, and its chemical stability [16]. The bandgap energy determines the energy of the photons that the photocatalyst can absorb for electron-hole pair generation. For a large bandgap material, only photons with high energy level are absorbed by the photocatalyst. These high energy photons have small wavelength and lies in the UV region and beyond. As indoor lightings possess little or no UV light, these large bandgap photocatalysts have limited application for indoor. One of the best photocatalyst, anatase TiO_2, has a large bandgap of 3.2 eV. As such, it can only absorb photons in the UV region (wavelength < 390nm).

Another important factor is the potential of the conduction and valence band as this determines the oxidation and reduction potential of the generated electrons and holes. For photocatalytic reaction to proceed, the valence band has to be more oxidative than the formation of $HO_2\bullet$ while the conduction band is more reductive than the formation of hydroxyl radicals. Figure 2.2 shows the valence band and conduction band potential of some of the commonly known photocatalyst and the

oxidation and reduction potential of HO_2• and OH• radicals [14]. Among these photocatalysts, anatase and rutile TiO_2, strontium titanium ($SrTiO_3$) and cadmium sulfide (CdS) fit the oxidation and reduction potential criteria. In addition to the list, both zinc oxide (ZnO) and cadmium selenium (CdSe) also fit the criteria [17].

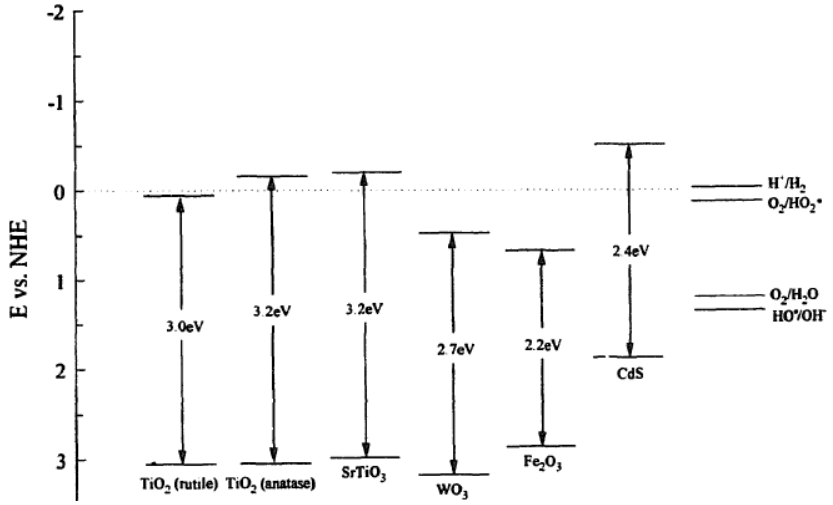

Figure 2.2 Conduction and valence band position of various photocatalysts. The oxidation potential of *OH*• and reduction potential of *HO_2*• is shown on the right [14].

Stability is another important consideration as most photocatalysts tend to suffer from photocorrosion. Photocorrosion occurs when the generated holes react with the photocatalyst and results in a decomposition of the photocatalytic material. Photocatalyst that can photocorrode includes ZnO [18], CdS [19], CdSe [20], Cu_2O [21] and WO_3 [22]. For CdS and CdSe, the photocorrosion process releases Cd^{2+} ions which are extremely toxic to the environment (Cadmium is banned by European Union's Restriction on Hazardous Substances). Therefore, while CdS and CdSe have visible light absorption capabilities, it cannot be used for practical applications. The photocorrosion process for ZnO is shown in equation 2-8 [23].

$ZnO + 2h^+ \rightarrow Zn^{2+} + ½ O_2$ (2-8)

Among the various photocatalyst, TiO_2 is widely preferred as it has shown good stability with high photocatalytic capabilities. In addition, TiO_2 is cheap, non-toxic and has been shown to degrade several organic compounds such as ethanol [24], stearic acid [25], or phenol [26]. However, its large bandgap allows only UV light absorption which limits its application.

2.2 TiO_2 photocatalyst

TiO_2 crystallizes in three different phases; rutile, anatase and brookite. Among the three phases, brookite is least studied for it photocatalytic property due to its wide bandgap (3.29 eV) and difficulties in preparing pure brookite particles. Anatase, on the other hand, is well-studied as it has the highest photocatalytic property among the three phases. Its large bandgap of 3.2 eV, however, allows only absorption of photons with wavelength < 390 nm. This falls beyond the visible light region and in the UV region. For rutile, it was thermodynamically more stable compared to the other two phases. It has a smaller bandgap of 3.0 eV and can absorb photons at higher wavelength (< 410 m,). However, the photocatalytic property of rutile is much lower compared to anatase. The lower photoactivity is caused by a smaller density of hydroxyl group on the surface of rutile. This results in poorer adsorption of oxygen molecules which is necessary for the photocatalytic process (equation 2-3) [27, 28]. Another explanation is that rutile, being a direct bandgap semiconductor, has a higher electron-hole recombination rate [29]. Anatase, on the

other hand, is an indirect bandgap semiconductor [30], and, thus, has a higher photocatalytic property.

Research has shown that mix phase of anatase and rutile (Degussa P25) exhibits greater photocatalytic property over its respective pure phase [31]. The synergetic effect of P25 was initially attributed to better electron hole pair separation as electrons are accumulated in rutile while holes are accumulated in anatase [32]. The accumulation of electrons in rutile is due to the conduction band position which is more positive for rutile (Figure 2.2). Hurum et al. [8], however, showed that rutile plays a more active role in enhancing the photoactivity of P25. Electrons generated in rutile are transferred to lower energy trapping sites in anatase, which is then transferred to the surface for photocatalytic reaction. Such transfer of electrons reduces recombination of photogenerated charges as the generated holes are left behind in the rutile phase. Furthermore, the presence of rutile allows absorption of higher wavelength photons. This extends the useful range of photoactivity towards the visible region, which increases the amount of electrons and holes to be generated. Thus, with a reduction in recombination effect and an increase in the amount of generated charges, the photoactivity of a mixed anatase and rutile phase is better than its pure phase.

2.3 Methods of improving photocatalytic property of TiO_2

Several methods have been employed to improve the photocatalytic property of TiO_2; (1) increasing the surface area, (2) metal loading, and (3) heterojunction semiconductor effect. Surface area increases the number of active sites for the

transfer of electrons and holes, while both metal loading and heterojunction semiconductor effect serve to reduce recombination of electrons and holes and improve photocatalytic effect. Here the effect of improving the photocatalytic property of TiO_2 is discussed.

2.3.1 Effect of surface area on photocatalytic reaction

Surface area plays an important role to the photocatalytic reaction as only electrons and holes generated near the surface can participate in the photocatalytic reaction. Due to the short characteristic lifetime of these photogenerated electrons and holes [33], those generated in the bulk are more probable to have recombined before reaching to the surface for photocatalytic reaction. Almquist et al. [34] synthesized anatase nanoparticles of various particle size and showed that a smaller particle size (30-60 nm)favors a faster photocatalytic reaction (Figure 2.3). This is due to the fact that small particles have a bigger surface area which allows greater interaction with the organic contamination. Further decrease in particle size (<30 nm) however has an adverse effect on photoactivity as there is an increase in bandgap energy due to quantum effect. Due to the effect of surface area, several methods are used to increase the surface area of the photocatalyst such as mesoporous TiO_2 [35], synthesize of large surface area nanocrystalline TiO_2 particles [36], or fabricating titania nanotubes [37].

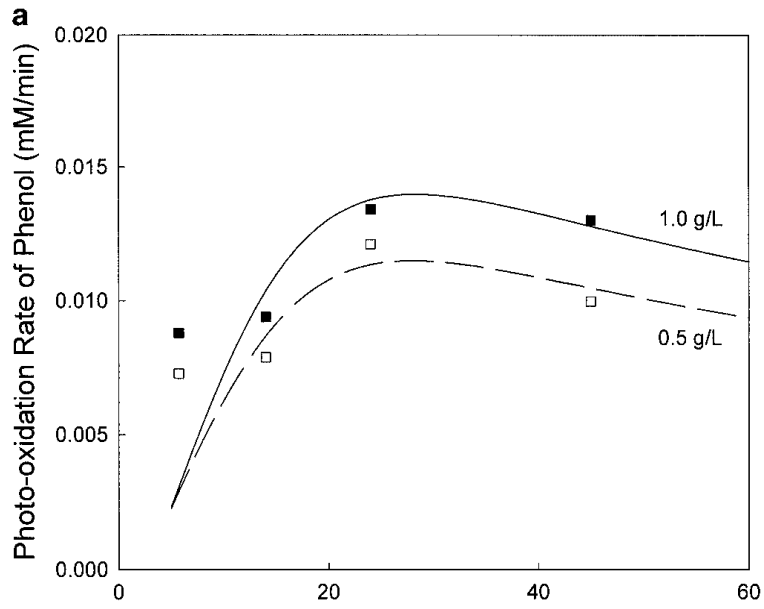

Figure 2.3 Photo-oxidation rate of phenol for flame synthesized TiO_2 [34].

2.3.2 Effect of metal loading

Metal loading has the effect of separating electrons and holes through migration of electrons to the metal while leaving the holes behind in the photocatalyst. This reduces their recombination and allows more electrons and holes to be available for photocatalytic reaction [38]. Such enhancement to the photocatalytic reaction had been observed with several noble metals such as platinum [39-41], silver [39], gold [40, 41], or palladium [41, 42].

The effect of metal loading is affected by the particle size of the metal attached to the photocatalyst. The attached metal has an effect of shifting the Fermi energy of the photocatalyst towards the conduction band of TiO_2 [43]. A smaller metal particle size induces a greater shift in the Fermi energy as it is more electronegative

[44]. This allows a greater amount of electrons to be accumulated in the metal-TiO_2 system, thus, improving its photoactivity.

The metal loading effect is, however, limited by the formation of recombination centers in the metal-TiO_2 system. Under prolong illumination, photocurrent generated by the metal-TiO_2 system is found to decrease. The decrease is caused by oxidation of the attached metal by the generated hydroxyl radicals [45]. This creates electron-hole recombination centers and results in the decrease in photoactivity. As such, while metal loading helped to improve photoactivity through separation of electrons and holes, the attached metal can also introduced electron hole recombination centers to the system.

2.3.3 Heterojunction semiconductor effect

Similar to the effects of metal loading, heterojunction semiconductor effect serves to improve photoactivity through separation of electrons and holes between two different photocatalysts. The separation of electrons and holes occurs via difference in the potentials of the conduction and valence band of the two semiconductors. Figure 2.4 shows the heterojunction system of CdS and TiO_2, where electrons generated in CdS migrate to the TiO_2 while holes migrate to CdS.

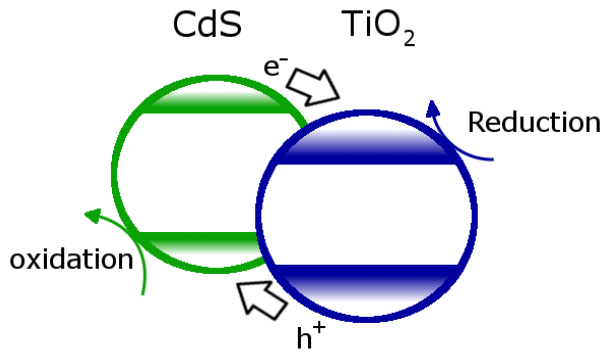

Figure 2.4 Band diagram of CdS/TiO_2 heterojunction semiconductor system.

Several heterojunction semiconductor photocatalysts had been reported, WO_3/TiO_2 [46], $SrTiO_3/TiO_2$ [47] and Fe_2O_3/TiO_2 [48]. Among these heterojunction semiconductors, CdS/TiO_2 generates greater interest as in addition to the separation of electrons and holes, CdS photocatalyst also has visible light photocatalytic property. This gives an added functionality to the heterojunction semiconductor photocatalyst. However, such heterojunction semiconductor system could not adequately address the toxicity issue of Cd^{2+} and the photocorrosion of CdS [49].

Another heterojunction semiconductor that has generated great interest is anatase/rutile heterojunction semiconductor. With the high photocatalytic behavior of Degussa P25, several researches have looked at fabricating anatase rutile composite material to enhance the photocatalytic effect under UV illumination. The synergetic effect between anatase and rutile requires 2 conditions to be fulfilled [8]; small rutile particle size and intimate contact between anatase and rutile. Various methods has been carried out to fabricate the anatase/rutile composite material, heat treatment for partial anatase rutile phase transformation [50], homogenized particle mixture through mechanical grinding [51], or through core-shell structure [52].

While some methods had shown positive effects to its photocatalytic property, others had shown a decrease instead due to a decrease in surface area [50].

2.4 Methods of achieving visible light photocatalyst

Most researchers focus on finding a stable photocatalyst with visible light absorption capabilities. Visible light photocatalyst has a wider application especially for indoor application where UV light intensity is almost negligible. For outdoor application, visible light photocatalyst offers a higher efficiency as 40 % of the solar spectrum falls within the visible light spectrum. This compares favourably to only 5 % for UV region. Currently, visible light photocatalysts, such as CdS, suffers from photocorrosion under illumination. Thus, researchers have focused on narrowing the bandgap of existing photocatalytic materials or finding new novel materials for visible light applications.

For narrowing of bandgap of existing photocatalyst, some of the widely used methods include doping with transition metals [53], or non-metal doping [54] and creating oxygen vacancies [55] in the photocatalyst. These three methods work by introducing band states in the bandgap of the photocatalyst, thus narrowing its bandgap. This allows lower energy photons to be absorbed for photocatalytic reaction to proceed. Here, a review on the visible light photocatalytic effect of $SrTi_{(1-x)}Fe_xO_3$ is also carried out.

2.4.1 Transition metal doping

Transition metal doping narrows the bandgap of TiO_2 through the introduction of band states in its bandgap. The band states act as electron or hole traps and allow the absorbance of visible light for the generation of electron-hole pairs. Figure 2.5 shows the energy level of the metal dopants in rutile TiO_2 [56]. Various metal dopants such as Fe^{3+} [57, 58], Cr^{3+} [59], V^{4+} [60], and Sn^{4+} [61], are reported to have visible light photocatalytic effect when doped into TiO_2.

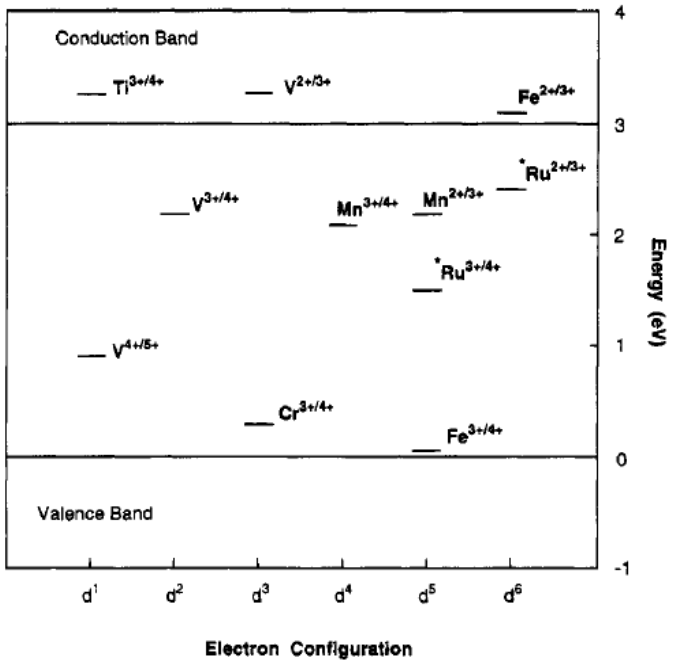

Figure 2.5 Energy levels of impurity ions in rutile [56].

While metal doping is capable of reducing the bandgap of TiO_2, at high doping concentration, the metal dopants form recombination centers which adversely affect the photoactivity. Such adverse reaction at high doping concentration has been observed in many metal-doped TiO_2 photocatalyst [56, 57, 62]. Thus, while the

metal dopants can reduce the bandgap of TiO_2, the amount of metal doping is limited by the formation of recombination centers.

2.4.2 Non-metal doping

Non-metal doping has gain widespread recognition in 2001 with the visible light degradation of acetaldehyde and methylene blue by nitrogen doped TiO_2 [63]. Since its discovery, numerous reports had surfaced reporting on the visible light photocatalytic effect of N-doped TiO_2 [64-66]. Other anion doping, such as carbon [67] and sulphur [68], are also reported to have similar bandgap narrowing effect and visible light photoactivity.

The mechanism of non-metal doping is similar to metal doping where band states were introduced in the bandgap of TiO_2. For non-metal doping, band states are formed above the valence band of TiO_2 [69, 70], resulting in the bandgap narrowing effect. This allows absorption of visible light for photocatalytic reaction. However, similar to metal doping, non-metal doping also introduce recombination centers which cause a decrease in quantum efficiency as the doping concentration are increased [69].

2.4.3 Oxygen vacancies

Oxygen vacancies are defect sites in TiO_2 which introduce defect energy states in its bandgap. These vacancies can be generated through plasma treatment of TiO_2 in a reducing gas ambient [71]. The defect energy states are situated at about 0.75-1.18 eV below the conduction band of TiO_2 as shown in Figure 2.6 [72]. With these

oxygen defect states, electrons are promoted to the conduction band through absorption of visible light. However, these vacancies can re-oxidize under atmospheric condition, which make its visible light photocatalytic effect non-lasting [73].

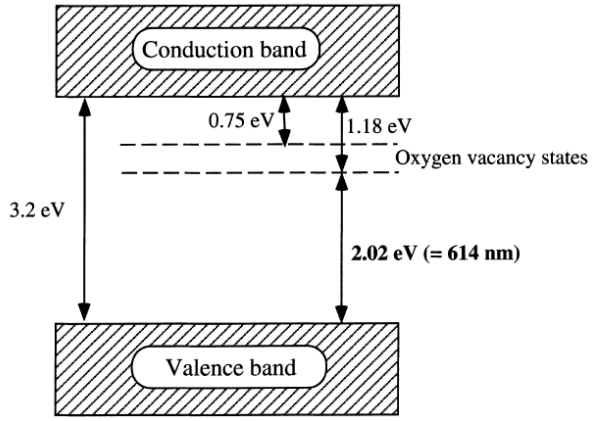

Figure 2.6 Oxygen vacancy states in TiO_2 bandgap [72].

2.4.4 Strontium titanium ferrite $SrTi_{1-x}Fe_xO_{3-\delta}$

Strontium titanium ferrite, $SrTi_{1-x}Fe_xO_{3-\delta}$, is a continuous solid solution of $SrTiO_3$ and $SrFeO_{3-\delta}$. $SrTiO_3$ is a wide bandgap photocatalyst (3.2 eV) with similar conduction and valence potential as TiO_2 (Figure 2.2). It has been shown to have photocatalytic capabilities with the degradation of methylene blue [74], nitrogen monoxide [75], Rhodamine B [76] and phenol [77]. Various metal and non-metal dopants are also carried out on $SrTiO_3$ to reduce its large bandgap [78, 79]. $SrFeO_{3-\delta}$, on the other hand, is a small bandgap material (1.9 eV) and is less known for its photocatalytic property. However, it has shown photocatalytic capabilities with the degradation of methyl orange [80] and methylene blue [81].

For a solid solution of $SrTiO_3$ and $SrFeO_{3-\delta}$, the bandgap of $SrTi_{1-x}Fe_xO_{3-\delta}$ can be tuned according to the amount of Fe ions. Through measurement of the electronic conductivity, Rothschild et al. [82] calculated and showed that the bandgap of $SrTi_{1-x}Fe_xO_{3-\delta}$ decreases with increasing iron content in the material (Figure 2.7). They also propose that the bandgap varies according to the equation 2-9. The bandgap narrowing effect arises from the introduction of Fe^{3+}/Fe^{4+} energy states, which lies at 1 eV above the valence band of $SrTiO_3$. In this research, the visible light effect of $SrTi_{1-x}Fe_xO_{3-\delta}$ particles embedded in TiO_2 films will be investigated.

$$\text{Bandgap} = 3.26 - 1.93x + 0.54x^2 \text{ (eV)} \quad (2\text{-}9)$$

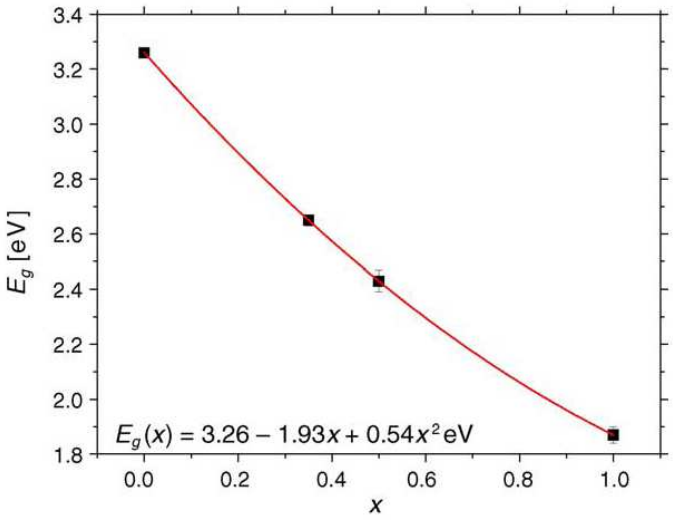

Figure 2.7 Variation of $SrTi_{1-x}Fe_xO_{3-\delta}$ bandgap with iron content [82].

2.5 Various methods of depositing TiO_2 thin films

Photocatalytic thin films offer better applications than particles as it ensures that the photocatalytic material are not lost after each application. Various deposition

methods are used in the deposition of TiO_2 thin films. Amongst these deposition techniques, sol-gel [35], chemical vapor deposition (CVD) [9] and physical vapor deposition (PVD) [83] are the most popular techniques for photocatalytic TiO_2 thin films.

Sol-gel offers a relatively cheap method of depositing a thin film. TiO_2 films may be applied onto a surface by spray, dip-coat or spin coat the sol-gel solution onto the substrate. Its biggest advantage is its low cost and ease of deposition on substrate with complex geometries. Due to its low cost, several researches have focus on using sol gel for photocatalytic applications [35, 84]. Chemical vapor deposition, on the other hand, produce films of better quality and adhesion compared to sol-gel. The CVD system may comprises of simple equipment to highly sophisticated ones such as atomic layer chemical vapor deposition. One disadvantage of CVD deposition is the possible release of toxic gas (i.e. HCl) as a by-product. Physical vapor deposition deposits films with good uniformity and high quality. Due to its high vacuum system, films deposited with PVD have much lower contamination. However, PVD systems are usually very sophisticated and costly. It also requires a long pump down time for its vacuum.

Comparing the photocatalytic efficiency of TiO_2 films deposited by different methods, Mills et al. [85] shows that sol-gel deposited films has a higher quantum yield with 22×10^{-4} molecules of stearic acid destroyed per photon absorbed. This compares favorably to APCVD deposited films with only 3.5×10^{-4} molecules of stearic acid destroyed per photon absorbed. Further comparison with magnetron sputtered TiO_2 films shows that sol-gel films exhibit the fastest degradation of

stearic acid followed by PVD sputtered films and CVD deposited films [86]. The high photoactivity of sol-gel films is ascribed to the greater porosity, allowing greater interaction with the organic contaminants [87]. However, further studies have shown that CVD deposited films could similarly achieved high photocatalytic property. Evans et al. [9] reported that CVD deposited TiO_2 films could achieve stearic acid degradation rate of 0.07 $cm^{-1}min^{-1}$ which was higher than that previously reported for sol-gel films [86]. Recently, Vergohl et al. [88] have examined the photoactivity of TiO_2 films deposited by magnetron sputtering, evaporation, CVD, sol-gel and other deposition methods. High photoactive films were achieved by CVD, sol-gel and magnetron sputtering with CVD showing the highest photoactivity.

The deposition of TiO_2 films via CVD has an added advantage. CVD can be incorporated into float glass production line which reduces the cost of production and allows mass production of TiO_2 coated glass. Also, less toxic precursor may be used in the deposition of TiO_2 films, thus, ensuring safety to the operator. As such, the deposition of TiO_2 films via CVD deposition is of interest.

2.6 Chemical Vapor Deposition (Theory)

CVD deposits a film through reaction of gaseous precursor on the substrate surface. The deposition mechanism, shown in Figure 2.8, can be described in the following sequence.

1) Flow of precursor gases into the deposition chamber

2) Diffusion of precursor to the substrate surface through the boundary layer (boundary layer is the region where the flow velocity of gas changes from zero at the walls to the bulk velocity.)

3) Adsorption of precursor onto the substrate

4) Chemical reaction on the surface

5) Surface migration of atoms to growth sites

6) Desorption of by-products from surface

7) Diffusion of by-products to main flow region

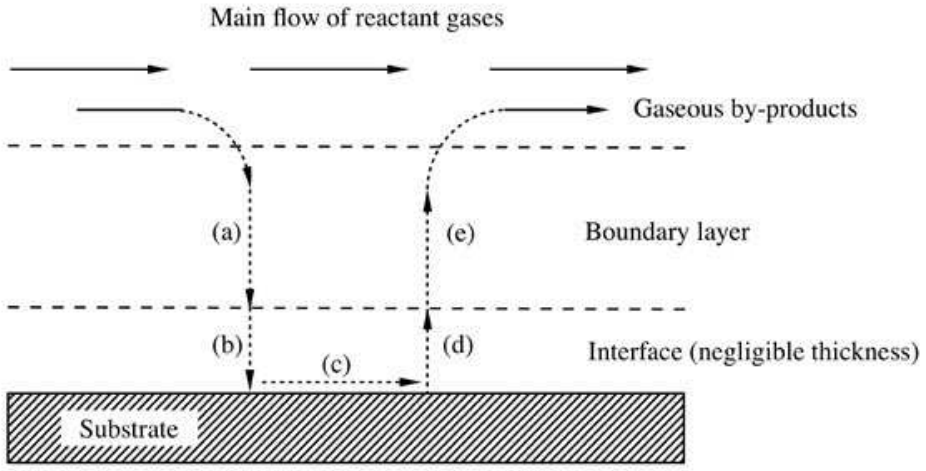

Figure 2.8 Sequences of events, (a) to (e), occurring during CVD [89]. (a) Diffusion of precursor gas through boundary layer. (b) Adsorption of precursor on substrate. (c) Chemical reaction of precursor. (d) Desorption of by-product. (e) Diffusion of by-product to main flow region.

The growth rate of CVD deposited films is limited either by surface reaction kinetics or mass transport of precursor to the substrate surface. For surface reaction kinetics, the growth rate is determined by the adsorption of precursor, its chemical reaction and the surface migration to its binding sites. Surface reaction kinetics usually dominates when the deposition temperature and pressure are low. This is due to low precursor reaction rate (low temperature) and fast diffusion rate of precursor to the substrate surface (thinner boundary layer).

For mass transport limited growth rate, the rate is determined by the diffusion rate of precursor and by-product across the boundary layer. This occurs at high deposition temperature and pressure where the fast reaction rate depletes the reactants on the surface and the thick boundary layer decrease the diffusion rate through the boundary layer.

Figure 2.9 shows the Arrhenius plot for the deposition of silicon layer [90]. Surface reaction rate dominates at low temperature where the growth rate increases with temperature. At high temperature, the growth rate is constant with temperature and is limited by the mass transport of reactants to the substrate surface.

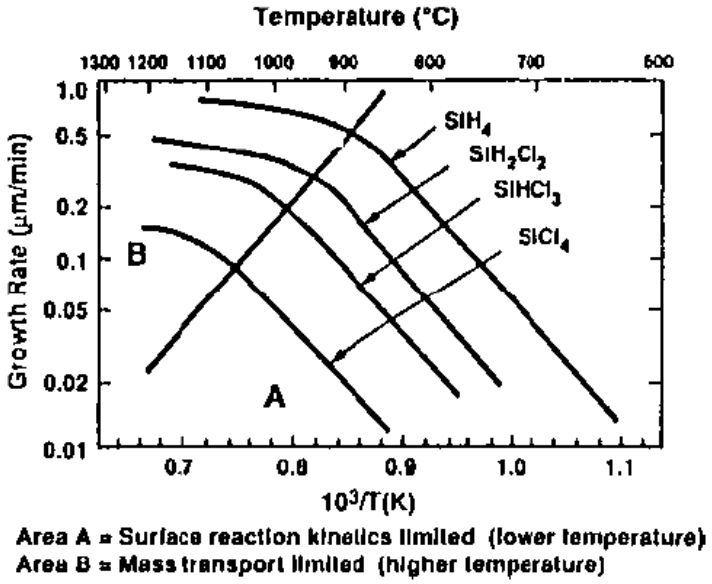

Figure 2.9 Arrhenius plot for silicon deposition using various precursors [90].

2.7 Various methods of embedding particles in APCVD deposited TiO_2 thin films

Different methods have been employed to embed particles into APCVD deposited films. Some require simple methods such as depositing the particles via conventional spray before coating the film over the particles, while others require more sophisticated method like AACVD or ion implantation onto the deposited films. Here, we look at the advantages and disadvantages of these methods in embedding particles in films.

2.7.1 Embedding particles via spray with APCVD

Particles can be embedded in APCVD films through conventional spray and APCVD [91]. The particles, to be embedded, are first dispersed in a solvent. The

liquid dispersion is atomized through a spray nozzle and deposits particles onto the substrate. The substrate is then heated to remove the solvent. A thin film is then deposited on top of the particles via APCVD. Such deposition method is relatively simple and provides better control on the particle concentration.

2.7.2 Embedding particles via AACVD

Aerosol assisted chemical uses a one-step deposition method to embed particles in CVD films [92]. The particles are dispersed in a solvent and ultrasonic agitation is applied to atomize the particle dispersion into tiny droplets. Such method has been used in the deposition of gold [93], CeO_2 [94] and WO_3 [95] particles in TiO_2, of which, films embedded with WO_3 particles had shown improved photoinduced superhydrophilicity due to its unique microstructure.

2.7.3 Embedding particles via ion implantation on APVCD deposited films

Ion implantation embeds particles by impinging ions into thin films. The impinged ions form supersaturated solid solution, which then precipitate out forming particles. Such deposition method has deposited titanium, chromium, tungsten, copper, silver and platinum particles into glass substrate [96]. While ion implantation was found to embed nano-sized metal cluster, the embedded particles is mostly limited to metal ions. As such, particles such as $SrTi_{1-x}Fe_xO_{3-\delta}$ could not be embedded through ion implantation. Furthermore, ion implantation is more costly due to the sophisticated equipment required for the implantation process.

2.7.4 Summary

Table 2.1 summarizes the advantages and disadvantages of various deposition methods for embedded particle films. Among the three processes, ion implantation is more suited for embedded metal particles. AACVD, on the other hand, has a poor control of particle concentration as particles can be lost in the gas delivery system or in the deposition head if incorporation into the conveyor belt APCVD system. As such, in this thesis, spray and APCVD is used for the deposition of particles embedded TiO_2 films.

Deposition method	Cost	Particle Uniformity	Control on amount of embedded particle
Spray with APCVD	Low	Moderate	Good
AACVD	Low	Moderate	Moderate
Ion Implantation	High	Good	Poor

Table 2.1 Summary of various deposition methods for embedding particles in CVD deposited films.

Chapter 3: Experimental Procedures

This chapter describes the deposition system and characterization methods for TiO_2 thin films. TiO_2 films were deposited using in-house built APCVD system. The APCVD system uses a conveyor belt system which ensures better uniformity on the coated TiO_2 films. Particles were embedded in the TiO_2 films through a spray system that was incorporated into the APCVD system. The particles were sprayed onto the glass substrate before coating a layer of TiO_2 film over it for binding the particles onto the substrate. Doping of TiO_2 films were carried out using AACVD. The APCVD system was converted into AACVD by changing the bubbler and adding an ultrasonic disk beneath the bubbler. Through ultrasonic agitation, tiny liquid droplets were generated in the bubbler. This allowed precursor mixture to be used for the deposition process. Other equipments used for experiment and characterization of the deposited films are also described in this chapter.

3.1 APCVD equipment used for TiO_2 films deposition

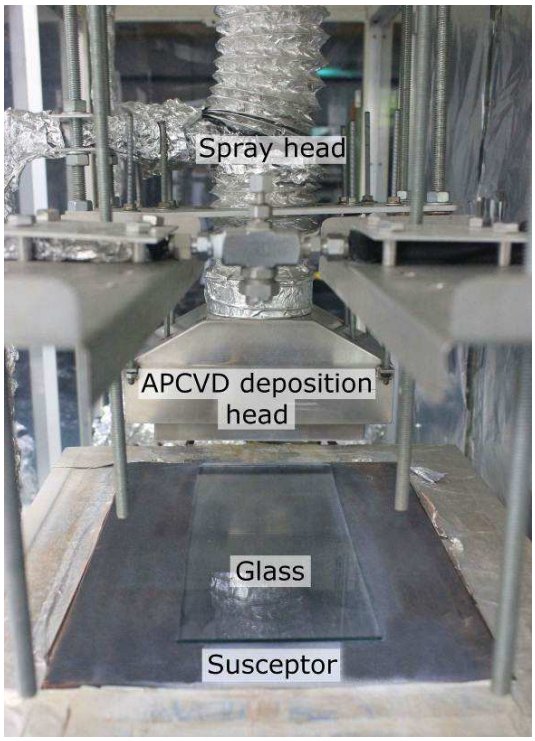

Figure 3.1 Picture of APCVD deposition head and susceptor.

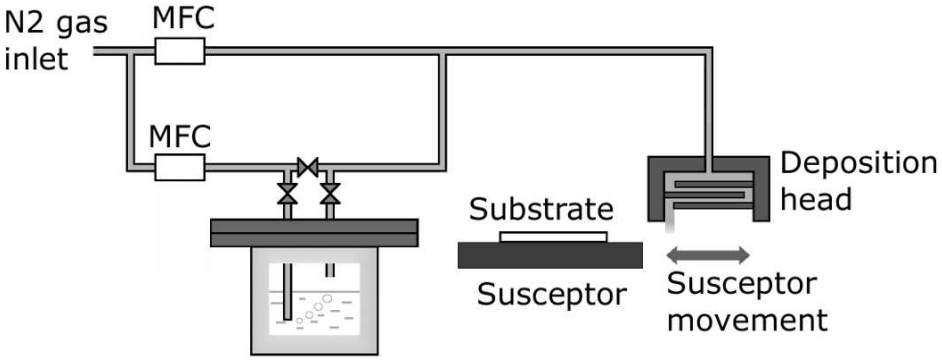

Figure 3.2 Schematic diagram of APCVD. (MFC: Mass flow controller).

TiO_2 films were deposited using in-house built APCVD system. The APCVD equipment (Figure 3.1 and Figure 3.2) consists of 3 main components: bubbler, deposition head and a conveyor belt susceptor where substrates are placed. Liquid precursor titanium tetraisopropoxide (TTIP, 97 % purity, Aldrich) is stored in the air-tight bubbler which has an inlet and outlet gas pipe. The inlet gas pipe is submerged in the liquid precursor while the outlet pipe is situated above the precursor level. N_2 carrier gas is injected into the bubbler and bubbled through the liquid precursor. This allows the carrier gas to be saturated with gaseous precursor before exiting from the bubbler. The saturated precursor mixture is then transported to the deposition head. Along the way, N_2 dilution gas is added to the carrier gas mixture for spreading of precursor gas in the deposition head and to achieve better film uniformity.

At the deposition head, a series of metal plates are placed horizontally across the flow path of the gas mixture. The metal plates force the gas to swirl around them, resulting in horizontal spreading of the gas mixture across the deposition head. The gas mixture then exits from the deposition head as a horizontal stream of precursor gas.

The hot susceptor moves through the precursor gas stream in a to and fro manner. This allows the precursor gas to interact with glass substrates placed on top of the susceptor. Through adsorption, diffusion and decomposition of precursor on the substrate, a thin TiO_2 film is formed on the glass substrate.

3.2 Embedding particles in TiO_2 films by particle spray followed by APCVD deposition

To embed particles in TiO_2 films, a two-step deposition method was used; particle spray followed by TiO_2 film deposition via APCVD. For the particle spray process, a spray system was incorporated into the APCVD system situated behind the deposition head but along the path of motion of the susceptor. Figure 3.3 shows the schematic diagram of the spray nozzle with APCVD system. The particles, dispersed in a solvent, were sprayed onto the substrate with a layer of TiO_2 film coated over the particles for binding of particles onto the substrate. Through the consistent to and fro motion of the susceptor, repeatability in the spray process is achieved.

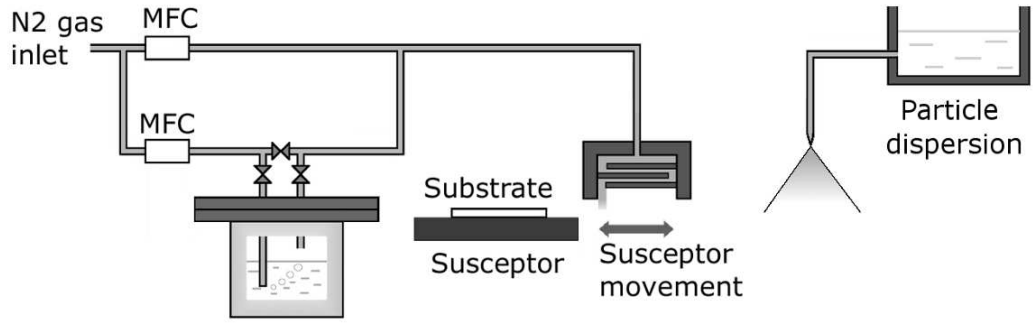

Figure 3.3 Schematic diagram of spray with APCVD.

3.3 AACVD deposition of tin-doped TiO_2 films

For doping of tin into the TiO_2 films, AACVD was employed as it allows better control of the doping concentration through a single-source precursor mixture. For

the AACVD system, an ultrasonic disk was added beneath the bubbler for generation of aerosol in the bubbler. The bubbler is made of plastic material so as to allow ultrasonic waves to propagate through and agitate the precursor inside it. Figure 3.4 shows the schematic diagram of the AACVD. With ultrasonic agitation, tiny droplets of liquid precursor were generated inside the bubbler. These droplets were transported by N_2 carrier gas to the deposition head and deposited the tin-doped TiO_2 coating on the substrate. The precursor used consisted of a mixture of titanium (TTIP) and tin precursor (tetrabutyl tin, Merck). Prior to film deposition, aerosol was generated in the bubbler for 15 minutes to ensure sufficient liquid droplets to be present in the bubbler.

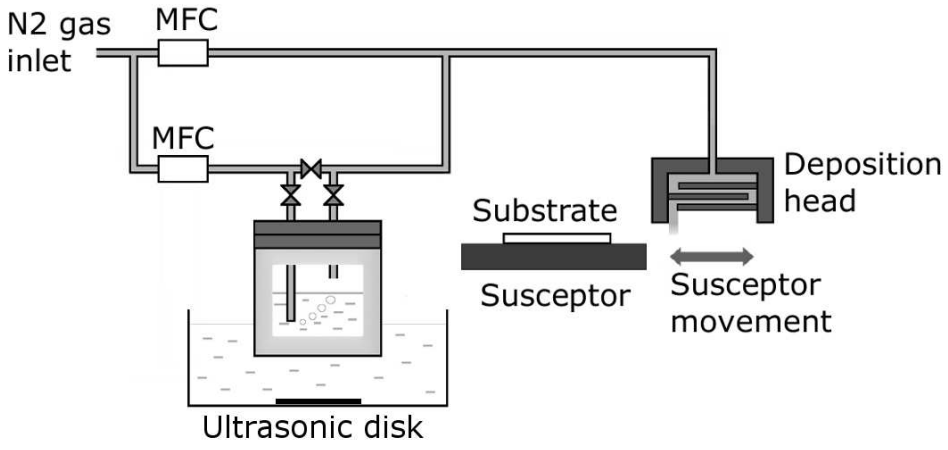

Figure 3.4 Schematic diagram of AACVD. An ultrasonic disk was placed underneath the bubbler for the generation of aerosol in the bubbler.

3.4 Synthesize of $SrTi_{(1-x)}Fe_xO_3$ particles

$SrTi_{(1-x)}Fe_xO_3$ particles were synthesized through high temperature solid state reaction. The starting materials, $SrCO_3$ (Sigma Aldrich), TiO_2 (Alfa Aesar) and Fe_2O_3 (Alfa Aesar), were ground and mixed together in stoichiometric ratio according to the x value of the particles to be synthesized. The particle mixture was sintered at 1200 °C for 24 hr, after which, the mixture was ground and sintered again for another 24 hr at 1200 °C. Using high temperature solid state reaction, reasonably pure $SrTi_{(1-x)}Fe_xO_3$ particles were achieved.

3.5 Particle size measurement and stability of dispersion

Particle size distribution of dispersion was determined from Malvern Instrument Zetasizer Nano-ZS using dynamic light scattering technique. This technique uses fluctuation in scattered light intensity caused by Brownian motion of the particles and determined its diffusion speed. Together with the Stokes-Einstein (equation 6-1), the hydrodynamic diameter of particles can be determined. Hydrodynamic diameter refers to the diameter of a sphere with a similar hydrodynamic drag as the particle;

$$r = \frac{kT}{6\pi\eta D} \qquad (6\text{-}1)$$

where r is radius of the spherical particle, k is Boltzmann's constant, T is absolute temperature, η is viscosity and D is the diffusion constant.

The stability of dispersions was analyzed using a settling test and by measurement of the zeta potential. Settling test measures the particle size of the dispersion after leaving the dispersion standstill for a certain period of time. It provides a measure of how fast particles agglomerate over a period of time. On the other hand, zeta potential provides an indication of the surface charge or the repulsive force between the particles. The use of zeta potential for measurement of particle dispersion stability has been outlined in ASTM standard D 4187-82 (Table 3.1). Particle dispersion with absolute zeta potential of > 30mV can be considered as stable dispersion according to the ASTM standard.

Zeta potential (mV)	Stability behavior of the colloid
From 0 to ±5,	Rapid coagulation or flocculation
From ± 10 to ±30	Incipient instability
From ± 30 to ±40	Moderate stability
From ± 40 to ±60	Good stability
More than ±61	Excellent stability

Table 3.1 Assessment of the stability of dispersions from zeta potential measurement.

3.6 Optical bandgap measurement

TiO_2 film's bandgap was determined from the transmittance spectrum measured from UV-Vis spectrophotometer (Shimadzu UV-3101PC). From the transmittance

spectrum, absorption coefficient (α) was calculated according to Beer-Lambert's law as shown below.

$$\alpha = (\ln T) / d \quad (6\text{-}2)$$

where T is transmittance and d is thickness of the film.

The absorption coefficient measures the fraction of light absorbed by a material of unit thickness. With the absorption coefficient, a Tauc plot can be plotted through the following relation:

$$(\alpha hv)^n = A(hv - E_g) \quad (6\text{-}3)$$

From the Tauc plot (αhv vs. energy), the bandgap of the material was determined by extrapolating the slope of the curve to the photon energy axis. Figure 3.5 shows an example of the Tauc plot and the measurement of its bandgap.

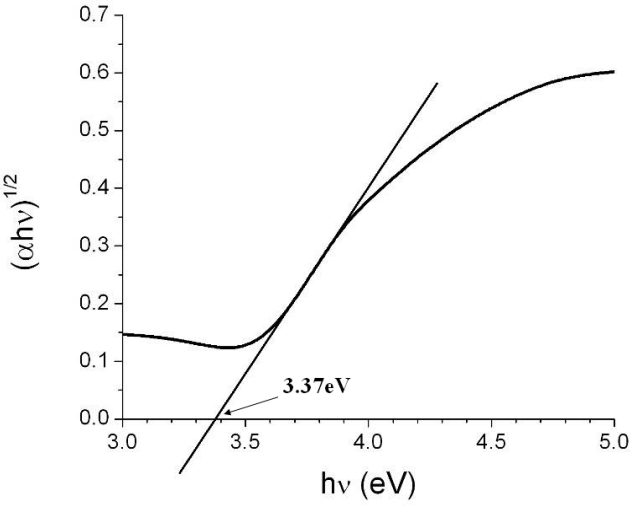

Figure 3.5 Bandgap measurement using Tauc plot. The bandgap (3.37 eV) is determined from the intersection between the x-axis and the extrapolation of the curve.

3.7 Percentage surface area measurement of TiO_2 films

Percentage surface area difference shows the percentage increase in surface area over a perfectly flat plane with the same projected area. As photocatalytic reaction rate is affected by surface area, it is thus crucial to measure the surface and analyze its effect on the photoactivity of the films. The percentage surface area difference was calculated from Atomic force microscope (AFM, Nanoscope IIIa, Digital Instrument) measurement. First, the area scanned by AFM was divided into small triangles where the coordinates each triangle vertexes were scanned by the AFM. With the x, y and z coordinates and simple trigonometry equation, the area of each triangle can be calculated. Through summation of the area of triangles, the film's surface area and percentage surface area difference were determined. Such technique had similarly been used in the calculation of surface area of membrane [98], pyrite [99], calcite surface [100] and PET surface [101].

3.8 Surface coverage of particles embedded in TiO_2 films

Surface area coverage of particles in the TiO_2 films was determined using scanning electron microscope (SEM, Carl Zeiss Ultra Plus Field-Emission Scanning Electron Microscope) image and an imaging software. The imaging software used is ImageJ, which was developed by National Institutes of Health. First, ImageJ was used to differentiate the pixels belonging to particle from the substrate pixels. This was carried out using the threshold function which differentiated the pixels according to its brightness. Next, using the particle analyze function, the software calculated the total number of pixels, area fraction occupied by the particles and average diameter

of the particles. Such analytical method had been used for measuring the particle size of silicon carbide [102], Fe/Fe oxide particles [103] and the fractional coverage of gold island on glass [104].

3.9 Photocatalytic test – decomposition of stearic acid

Photocatalytic activity of TiO_2 films was determined using stearic acid test. The degradation test was carried out by measuring the decrease in stearic acid remaining on the sample. First, the sample was radiated overnight under UV illumination (Hitachi FL15BL-B, intensity 0.5 mW/cm^2 at 365 nm). Next, a Fourier Transform Infrared Spectrometer (FTIR, IRPrestige-21 Shimadzu) baseline measurement was recorded for the sample. Stearic acid, concentration of 10 mmol in methanol, was spin-coated onto the sample. The spin speed for stearic acid coating was 1000 rpm with an acceleration of 1000 rpm^2 for 1 minute duration. Methanol was removed from the substrate by heating it on a hot plate at 50 °C for 5 minutes. The FTIR spectrum of the stearic acid was measured and integrated area under the peak at a range of 2830-2975 cm^{-1} was recorded. After which, the sample was placed under UV or visible light illumination to initiate the photocatalytic reaction. The integrated area under the FTIR spectrum was recorded periodically and was plotted against its illumination time. The degradation rate of stearic acid was measured by calculating the rate of decrease in the integrated area. A typical variation of the FTIR spectrum with illumination time was presented in Figure 3.6. The two observed peaks are the antisymmetric (2920 cm^{-1}) and symmetric (2850 cm^{-1}) stretching vibration of CH_2 bond. Figure 3.7 shows an example of the decrease in

integrated area of the FTIR spectrum with illumination time. The degradation rate of stearic acid is determined from the magnitude of its gradient.

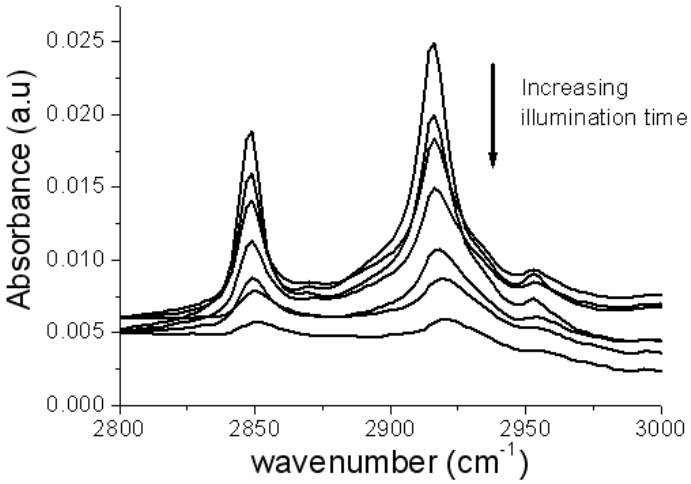

Figure 3.6 Decrease in C-H peaks with UV illumination time. Interval between each measurement is 2 minutes.

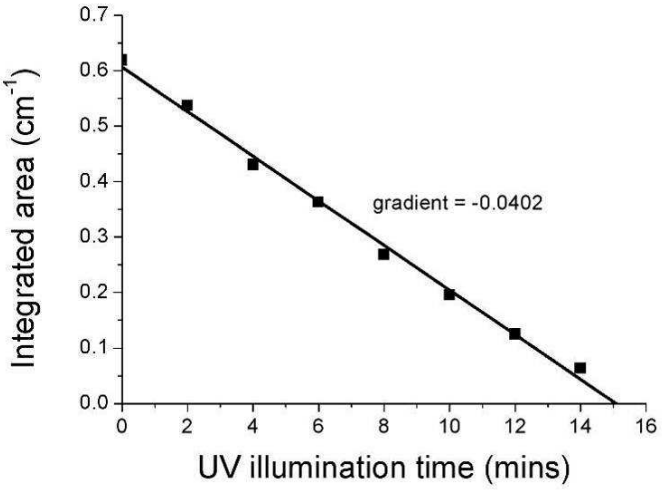

Figure 3.7 Decrease in integrated area with UV illumination time. The magnitude of the gradient shows the degradation rate of stearic acid.

3.10 Photocatalytic test – decomposition of ethyl cellulose

Ethyl cellulose was the second organic pollutant used to reaffirm the photocatalytic property of APCVD deposited TiO_2 films. The experimental procedure for ethyl cellulose degradation test followed closely to that of stearic acid. The TiO_2 films were radiated overnight under UV light illumination. Baseline measurement was recorded with FTIR and ethyl cellulose, at a concentration of 1.43 g/liter, was spin-coated onto the TiO_2 films. The films were periodically illuminated under UV light for photocatalytic reaction and analyzed with FTIR to determine the amount of ethyl cellulose remaining on the films. For analysis of FTIR spectrum, the integrated area was measured at a range of 2830-3010 cm^{-1}. Figure 3.8 shows the typical variation of FTIR spectrum of ethyl cellulose with UV illumination time. Other than the two CH_2 peaks, FTIR detected peaks such as CH_3 peaks (2920 and 2850 cm^{-1}), CH peak (2890 cm^{-1}), and possibly C-CH_3 (2872 cm^{-1}). The degradation rate of ethyl cellulose was measured from the decrease in integrated area with illumination time.

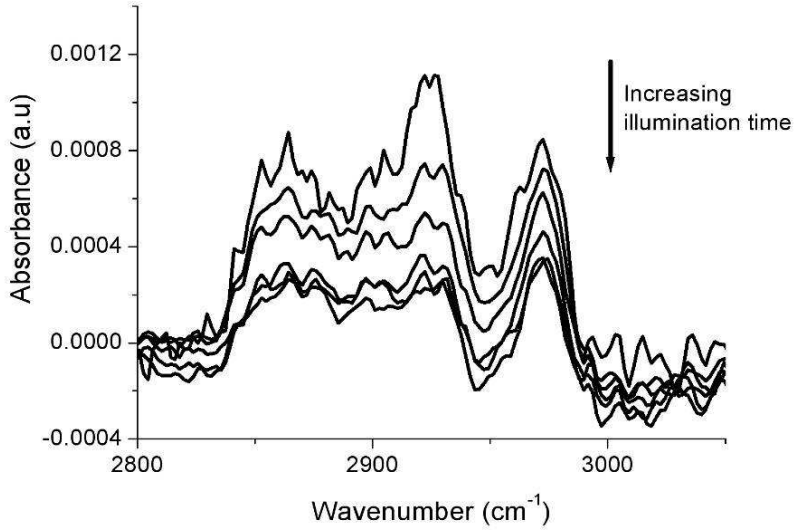

Figure 3.8 Decrease in ethyl cellulose peaks with UV illumination time. Interval between each measurement is 2 minutes.

3.11 Photocatalytic test for particles – decomposition of methylene blue

The photocatalytic property of particles ($SrTi_{1-x}Fe_xO_{3-\delta}$) was determined using methylene blue. 1.56 mmols of particles was ground in 50 ml of distill water using mortar and pestle. 10.8 ppm of methylene was added to the particle dispersion and the dispersion was ultrasound for 30 minutes. The concentration of methylene blue in the dispersion was analyzed using UV-VIS spectrophotometer. Florescent light (intensity 2500 lux) was used as the light source with an UV filter (cut-off wavelength at 435 nm) placed between the light source and the dispersion. The dispersion was sampled every hour to determine the amount of methylene left in the dispersion.

3.12 Other equipments

Other equipment used for this thesis includes Lindberg Blue M tube furnace and Jipelec JETfirst rapid thermal annealing for thermal annealing process. For characterization, Malvern Instrument Zetasizer Nano-ZS was used for particle size and zeta potential measurement of dispersion, X-ray diffractormeter (XRD, D8 Bruker Discover) was used to analyze crystal structure of the synthesized particles and films, Ellipsometry (HS-190 J.A.Wollam) was used to measure the film thickness, and X-ray photoelectron spectroscopy (XPS, Kratos-Axis spectrometer) was used for determining the chemical state and elemental composition of the deposited films.

Chapter 4: Deposition and characterization of TiO_2 films by APCVD system

The deposition of TiO_2 films was carried out using an in-house built APCVD system. The APCVD system (as described in Chapter 3), is capable of depositing thin uniform film and can be incorporated into a float glass production line. In this chapter, the deposition of photocatalytic TiO_2 films with APCVD equipment was described. The deposition parameters were varied one at a time to determine its individual effect on the growth rate of TiO_2 films. XRD and AFM were used to determine crystallinity and surface morphology of the deposited TiO_2 films. Photocatalytic property of TiO_2 films was determined using stearic acid as the organic contaminant. The effect of a SiO_2 diffusion barrier layer and TiO_2 film thickness on the photodegradation rate of stearic acid was also studied. Further test were carried out to ensure repeatability and reproducibility of the stearic acid test. Lastly, the photocatalytic property of deposited TiO_2 films was reaffirmed through the degradation of a second organic pollutant, ethyl cellulose.

4.1 Studies on APCVD deposition parameters

The effect of deposition parameters on the TiO_2 film's deposition rate was studied by varying one parameter at a time. The parameters studied included susceptor temperature, precursor temperature, bubbler gas flow rate and N_2 dilution flow rate. Other parameters such as the speed of the susceptor and gas line temperatures were

kept constant. Table 4.1 shows the initial value of the various parameters used for the TiO_2 film deposition.

APCVD deposition Parameters	Value
Susceptor temperature	575 ºC
Precursor temperature	65 ºC
Bubbler gas flow rate	0.78 slm
N_2 dilution flow rate	5 slm
Gas line temperature	65-80 ºC
Susceptor speed	0.225 m/min

Table 4.1 Initial deposition parameters for TiO_2 film deposition.

Figure 4.1 presents the variation of susceptor temperature on the growth of TiO_2 film per deposition cycle. Each deposition cycle is represented by a to-and-fro motion of the susceptor or a total of 2 passes underneath the deposition head. At temperature below 400 °C, a low deposition rate was observed as there was insufficient heat energy from the susceptor to initiate the decomposition reaction of the TTIP precursor. At susceptor temperature between 400 and 575 °C, the deposition rate showed an increase with increasing susceptor temperature. At this temperature range, the film deposition is in surface reaction kinetics limited regime and is limited by the surface reaction of TTIP precursor. Film deposition at this temperature range is less desirable as the deposition rate is affected by the susceptor

temperature. Any variation in susceptor temperature would cause a change in the TiO_2 film thickness.

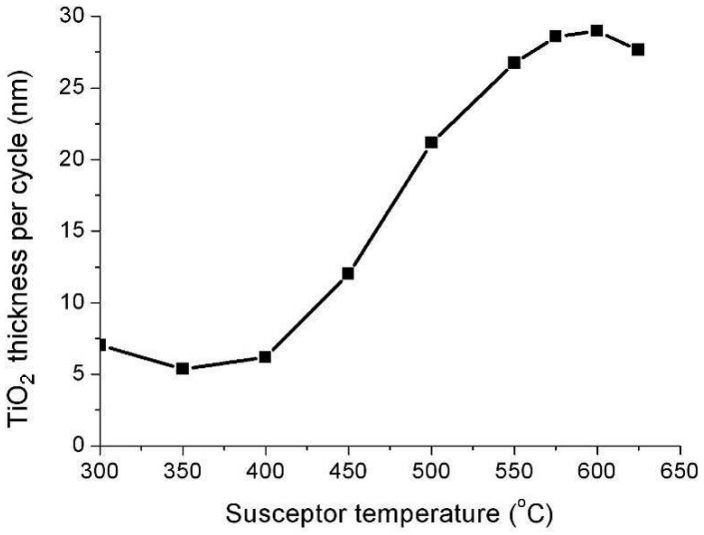

Figure 4.1 Deposition rate of APCVD with respect to the susceptor temperature.

At susceptor temperature above 575 °C, the deposition rate remained fairly constant. This temperature range represents the mass transport limited regime, where the reaction rate is limited by the amount of reactants carried onto the substrate surface. This temperature range is more suitable for film deposition as less variation in film thickness is expected. At 625 °C, a slight dip in deposition rate was observed. This dip is caused by parasitic effects such as gas phase nucleation or TiO_2 film deposition on the walls of deposition head [105]. Further increase in temperature would enhance the parasitic effect and lead to further decrease in TiO_2 film deposition rate.

From this study, a susceptor temperature between 575 - 625 °C was found to be suitable for TiO_2 film deposition. The deposition rate at this temperature range was

unaffected by fluctuation in the susceptor temperature and yet achieved a high deposition rate. Thus, the susceptor temperature of 575 °C was initially chosen for TiO_2 film deposition. However, it was later found that at this susceptor temperature, slight bowing of glass substrate can be observed. The bowing effect was caused by thermal stress within the glass substrate due to temperature difference between the top side (expose to air) and bottom sides (in contact with heated susceptor) of the glass. This bowing effect was more apparent during the deposition of embedded particle films where evaporation marks were observed on the glass substrate. Such evaporation marks caused the films to lose its uniformity. Due to the bowing effect, the susceptor temperature was lowered to 500 ºC where the bowing effect was less apparent.

Next, the variation of the liquid precursor temperature on the film's deposition rate was studied. Liquid precursor, stored within the bubbler, was heated up to promote the evaporation of precursor into gaseous phase. This ensured that sufficient gaseous precursors were present in the bubbler for transportation into the deposition chamber. Figure 4.2 shows the change in deposition rate with varying precursor temperature. An increase in deposition rate was observed with increasing precursor temperature. However, at precursor temperature of 75 and 85 °C, non-uniformity in the TiO_2 films was observed. This non-uniformity was caused by the huge amount of precursor gas transported into the deposition chamber, which was not effectively spread across the deposition head. As such, a precursor temperature of 65 °C was preferred.

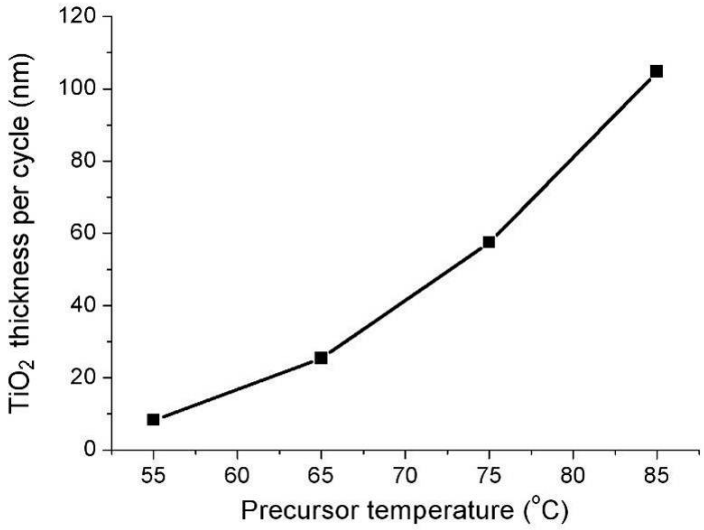

Figure 4.2 Deposition rate of APCVD with respect to the precursor temperature.

The effect of N_2 carrier gas flow rate on the TiO_2 deposition rate is presented in Figure 4.3. With an increase in N_2 gas flow into bubbler, more precursor gas was carried into the deposition chamber which increased the film deposition rate. Figure 4.3 shows a linear relation between carrier gas flow rates with TiO_2 film deposition rate. A linear regression line was plotted which has a coefficient of determination of 0.9964 and a linear equation of y = 38.1 x. The linear relation allowed easier control on the TiO_2 film deposition rate. A mid-range value of 0.48 slm was chosen for the N_2 flow rate as it provided more leeway for future adjustment on the deposition rate.

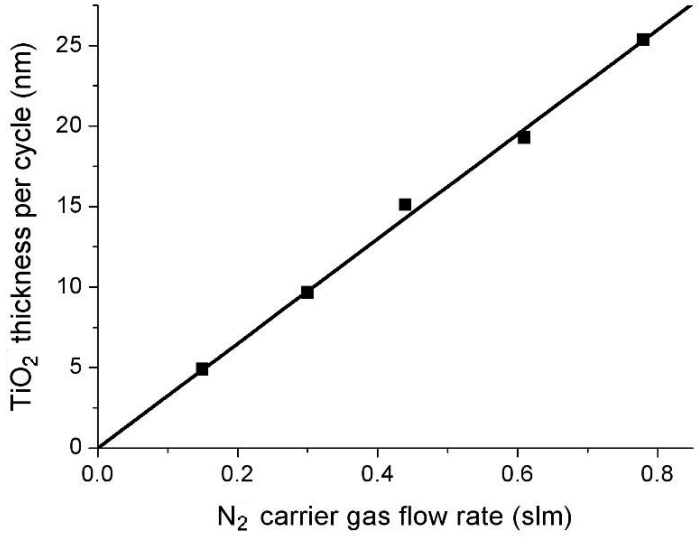

Figure 4.3 Deposition rate of APCVD with respect to flow rate of carrier gas.

Precursor saturated N_2 carrier gas was diluted by subsequent addition of N_2 gas into the distribution pipes to facilitate the spreading of precursor within the deposition head. The introduction of extra N_2 gas also had the effect of reducing the precursor concentration in the gas mixture, which inadvertently resulted in lower deposition rate. Figure 4.4 shows the effect of dilution of the N_2 flow rate on the deposition rate of TiO_2. The graph shows an inverse linear relationship between dilution flow rate and the film deposition rate. The linear regression line has a coefficient of determination of 0.9857 with an equation of $y = -2.77x + 40.7$. At a gas flow rate of 2 slm, non-uniformity of TiO_2 coating was observed due to insufficient carrier gas to spread the precursor gas uniformly. A gas flow rate of 5 slm was preferred as it has been used as the default settings for the film deposition and could yet achieve a high film deposition rate.

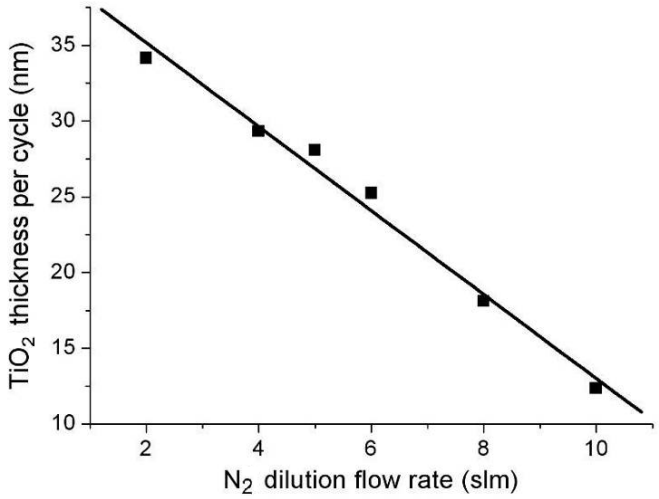

Figure 4.4 Deposition rate of APCVD with respect to the N_2 dilution flow rate.

From the APCVD deposition parameters studies, based purely on coating characteristic, the parameters recommended for TiO_2 deposition were, susceptor temperature 500 ºC, precursor temperature 65 ºC, carrier gas flow 0.48 slm, dilution gas flow rate 5 slm. Table 4.2 shows the parameters use for TiO_2 film deposition.

APCVD deposition Parameters	Value
Susceptor temperature	500 ºC
Precursor temperature	65 ºC
Carrier gas flow rate	0.48 slm
Dilution gas flow rate (N_2)	5 slm

Table 4.2 Parameters used to coat TiO_2 films.

4.2 XRD characterization for APCVD coated TiO_2 films

The crystallographic phase of APCVD deposited TiO_2 films were characterized with glazing angle XRD. The XRD analysis (Figure 4.5) confirmed that the APCVD deposited TiO_2 films comprised of photocatalytic anatase phase with peaks observed at 2θ value of 25.4°, 48.1°, 55.1°, 62.7°. These peaks corresponded to (101), (200), (211) and (204) planes for TiO_2 anatase phase. The (101) plane, being the dominant plane, provided the oxidative sites for photocatalytic reaction [106]. It was more easily formed on the coated surface due to its low surface formation energy [107].

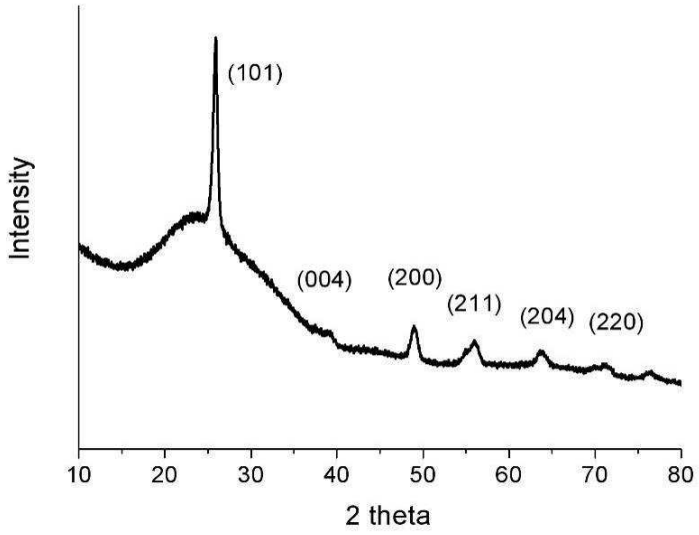

Figure 4.5 XRD analysis of APCVD-deposited TiO_2 films. Only anatase phase was detected by the XRD analysis. The broad peak at 2 theta =15-35° is caused by background noise from the soda lime glass substrate.

4.3 Growth mode of TiO_2 films deposited on soda lime glass

The growth of TiO_2 films on soda lime glass may proceed via two growth modes; Volmer Weber (island growth) and Stranski-Krastanov (layer plus island growth). Volmer Weber growth occurs when the cohesive energy between the atoms in the film is greater than that between the atoms and substrate surface. This results in the formation of islands on the film surface. For Stranski-Krastanov, the growth occurs with the layer by layer deposition followed by the formation of islands on the surface as the cohesive energy between the atoms in the film and substrate surface decreases with increase in film thickness

To elucidate the growth mode of TiO_2 films, its surface morphology was analyzed using AFM. Figure 4.6 shows that the surface of TiO_2 films consisted of several small grains having a diameter of 40-60 nm. The surface roughness of the film increased from plain glass substrate of 0.54 nm to 3.92 nm for TiO_2 films. This showed that the TiO_2 films grow via island growth. With the high deposition temperature, the growth was more likely to be Volmer Weber as the TiO_2 molecules readily diffused on the substrate surface forming clusters around nucleation sites. These clusters grew vertically up forming the islands as observed in the AFM images (Figure 4.6). Literature reports had similarly attributed TiO_2 films growth via Volmer Weber mechanism [108, 109].

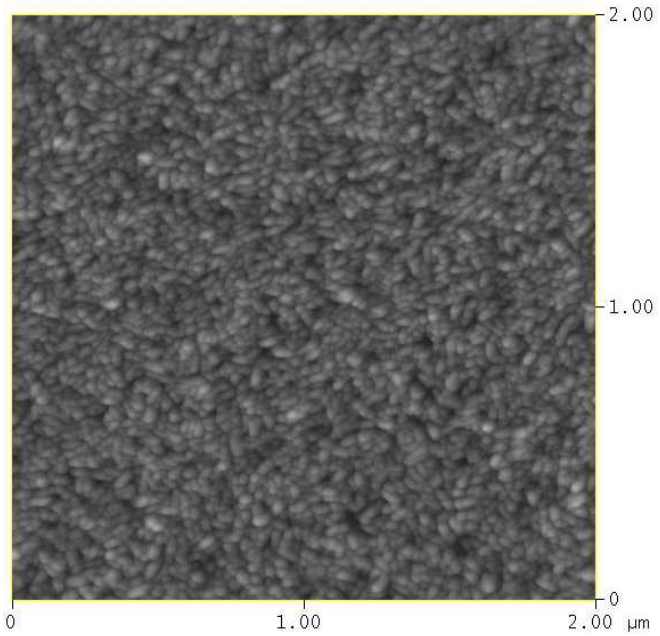

Figure 4.6 AFM analysis of APCVD-deposited TiO_2 films.

4.4 SiO_2 barrier layer

Photocatalytic property of TiO_2 thin films was adversely affected by sodium ion impurities, which can be found in soda lime glass substrate. The sodium impurities diffused into active TiO_2 layer, resulting in the following effects: formation of recombination centers for photogenerated electron hole pairs [110], and formation of inactive compounds such as $NaTiO_3$ [111]. Such detrimental effect is termed as "sodium poisoning" [112]. While sodium free glass (i.e. quartz) is available, these glasses are considerably more expensive and less commonly available than soda lime glass. To mitigate the effects of sodium ions, barrier layers such as SiN_x [112], or SiO_2 [113] can be coated to prevent the diffusion of sodium ions into the TiO_2 layer. In this research, SiO_2 films were used as the barrier layer, as it can be coated easily by dip-coating of the glass substrate in a SiO_2 sol-gel precursor. The effect of

SiO_2 layer thickness on the photocatalytic properties of TiO_2 films was studied to determine the appropriate thickness to prevent Na^+ ions diffusion into TiO_2 layer.

The SiO_2 sol-gel precursor was prepared by mixing tetraethyl orthosilicate (TEOS, 98 % purity, Sigma-Aldrich) with ethanol and water in a molar ratio of 1:6:4. The pH of the mixture was adjusted to 3 using acetic acid and stirred overnight. Prior to the dip-coating process, the glass substrate was cleaned through ultrasonic action in ethanol for 15 minutes. The glass substrate was then dip-coated into the pre-mixed sol-gel solution using MTS Synergie 200 system. The deposited film thickness was varied by changing the withdrawal speed of the dip coater system. After deposition, the substrate was cured at 400 °C for 1 hour to form the SiO_2 layer.

The deposited SiO_2 thickness can be approximated using the following Landau-Levich equation.

$$h = 0.94 \frac{(\eta v)^{2/3}}{\gamma_{LV}^{1/6} (\rho g)^{1/2}} \qquad (4\text{-}1)$$

where h = coating thickness

η = viscosity

v = withdrawal speed of substrate

γ_{LV} = liquid-vapor surface tension

ρ = density

g = gravity

For the same sol-gel solution composition and glass substrate, the Landau-Levich equation may be approximated to $h \propto (v)^{2/3}$, where a faster withdrawal speed of the glass substrate leads to a thicker deposited films. Table 4.3 presents the thickness of SiO_2 layer with varying withdrawal speed of the glass substrate. The deposited layer thickness was measured from an average thickness of 3 coated samples for each withdrawal speed using Ellipsometry.

Withdrawal Speed (cm/min)	5.08	7.62	10.16	12.70	15.24	17.78	20.32
Average thickness of SiO_2 (nm)	150±2	174±3	218±3	240±4	258±3	284±4	307±4

Table 4.3 Variation of thickness of SiO_2 deposited by dip coating with substrate withdrawal rate.

To determine the required thickness for the SiO_2 barrier layer, TiO_2 films were deposited on top of the barrier layer and photocatalytic test was carried out on the films. The test was initially carried out for TiO_2 films deposited at susceptor temperature of 575 °C as it was first used as the optimum parameter for deposition of TiO_2 films. This was later repeated on films deposited at susceptor temperature of 500 °C.

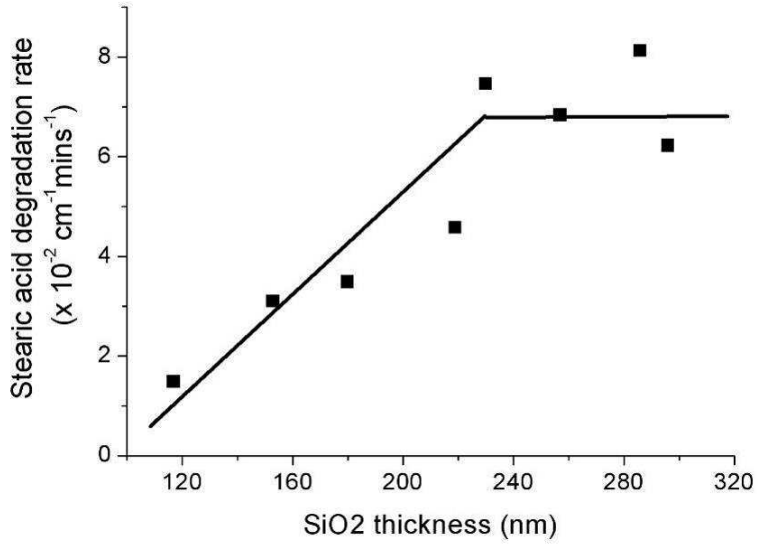

Figure 4.7 Effect of SiO_2 barrier layer on photocatalytic reaction of TiO_2 films deposited at 575 °C.

The photocatalytic test carried out on films deposited at 575 °C was conducted at an UV intensity of 1.5 mW/cm^2. Figure 4.7 shows variation of the stearic acid degradation rate with SiO_2 barrier layer thickness. Initially, with increasing SiO_2 barrier thickness, there was an increased in degradation rate of stearic acid. The degradation rate reached a plateau at a barrier thickness of around 240 nm, which was obtained at a withdrawal speed of 12.7 cm/min. Thus, for films deposited at susceptor temperature of 575 °C, a SiO_2 barrier layer of 240 nm was required to prevent sodium diffusion.

Further test was carried out for films coated at susceptor temperature of 500 °C at UV illumination of 0.5 mW/cm^2 (Table 4.4). A lower UV intensity was used to slow down the degradation of the stearic acid on the films. With a lowered susceptor temperature, a barrier layer thickness of 150 nm was found to be

sufficient to prevent the diffusion of sodium ions into the TiO_2 layer. This was lower than the 240 nm thickness required for in the previous test since the lower susceptor temperature reduced the sodium diffusion rate into the TiO_2 films. Stearic acid test carried out on TiO_2 films deposited on quartz glass also showed similar degradation rate. As such, this showed that a barrier layer of 150 nm thickness was effective in hindering sodium diffusion for films deposited at susceptor temperature of 500 °C.

From the SiO_2 barrier layer test, SiO_2 barrier layer thickness of 240 nm was effective in preventing sodium contamination in TiO_2 films deposited under both susceptor temperature of 500 and 575 °C. Thus, 240 nm SiO_2 layer was used as the barrier layer to prevent sodium diffusion into APCVD deposited TiO_2 films.

	Soda lime glass					Quartz
Average thickness of SiO_2 (nm)	150±2	174±3	218±3	240±4	258±3	-
Average thickness of TiO_2 (nm)	62±2	60±2	60±1	60±1	61±1	61±0.8
Stearic acid degradation rate (x $10^{-2}cm^{-1}min^{-1}$)	4.2±0.5	4.2±0.1	3.8±0.1	4.3±0.2	3.9±0.2	4.0±0.2

Table 4.4 Thickness of SiO_2 deposited with different dip coating withdrawal speed.

4.5 Effect of TiO_2 thickness on stearic acid degradation rate

Figure 4.8 shows the effect of TiO_2 film thickness on stearic acid degradation rate. The degradation rate was observed to increase with increasing film thickness at thickness below 60 nm. This increase in degradation rate was due to an increase in the concentration of photogenerated electron-hole pairs generated by the thicker TiO_2 films. Similar increase was also observed for sol-gel films [114] and CVD films coated using $TiCl_4$ as precursor [85].

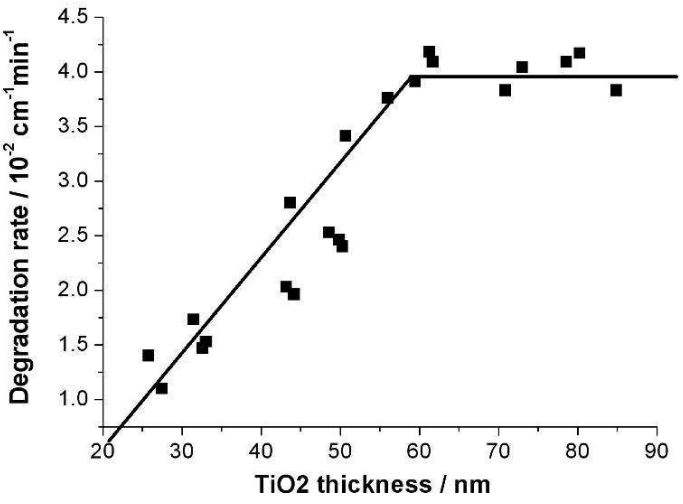

Figure 4.8 Effect of TiO_2 film thicknesses on photocatalytic reaction rate.

Beyond film thickness of 60 nm, the degradation rate was found to have plateau. 2 reasons could explain for the plateau in degradation rate: recombination of electron-hole pairs generated deep beneath the film's surface and lack of UV light absorbed by TiO_2 atoms underneath its surface. Using a model for diffusion of photogenerated electrons and holes, Tada et al. [114] showed that only electrons and holes generated within 100 nm from the film's surface could diffuse to the

surface for photocatalytic reaction. Mills et al. [85], on the other hand, found that most of the UV light were absorbed by TiO_2 films near to the surface. As such, little UV light reaches the TiO_2 films beneath the surface, leading to a saturation of photocatalytic reaction rate. The variation of stearic acid degradation in Figure 4.8 showed that the optimum thickness for the deposited TiO_2 film was 60 nm.

4.6 Reproducibility and repeatability studies of TiO_2 films and its photodegradation capabilities

Reproducibility tests were carried out on the TiO_2 films (with barrier layer) to study the reproducibility of APCVD coated films and their stearic acid photocatalytic test. 3 batches of TiO_2 films were prepared separately with 3 samples for each batch. UV light stearic acid test was carried out on these samples to determine the photocatalytic reaction rate.

Table 4.5 shows the stearic acid degradation rate of the three batches of TiO_2 films tested. The result showed good reproducibility of the stearic acid test with a degradation rate of 4.0×10^{-2} $cm^{-1}min^{-1}$. A standard error of 2.5 % was recorded. To minimize the errors in the degradation rate, stearic acid test should be carried over 3 different samples.

	Batch 1	Batch 2	Batch 3
Average TiO_2 film thickness (nm)	62.3±0.3	59±1.5	62.7±0.7
Average stearic acid degradation rate (x 10^{-2} $cm^{-1}min^{-1}$)	4.0±0.1	3.9±0.1	4.1±0.1
Overall average stearic acid degradation rate (x 10^{-2} $cm^{-1}min^{-1}$)			4.0±0.1

Table 4.5 Stearic acid reproducibility test on TiO_2 films.

Repeatability test was carried out on the same TiO_2 films to ensure that its photocatalytic property was not lost after the photodegradation process. The test was carried out on three TiO_2 films and repeated for three times on each sample. Table 4.6 shows the average stearic acid degradation rate of the TiO_2 films with each repeated test. The degradation rate for the three repeated test showed similarity to the average stearic degradation rate determined in Table 4.5. This showed that the photocatalytic property of the TiO_2 films was preserved and not lost after the photodegradation process. Further repeatability test was carried out on TiO_2 films with a storage period of 6 months in a box. Table 4.6 shows that the TiO_2 films remained photoactive despite a long storage period. XRD analysis (Figure 4.9) carried out on TiO_2 films after the stearic acid degradation process showed no change in the crystallinity of the TiO_2 films. Thus, this showed that the photocatalytic reaction process did not result in any detrimental effects to TiO_2 films.

	1st test	2nd test	3rd test	After 6 months
Average stearic acid degradation rate (x 10^{-2} $cm^{-1}min^{-1}$)	4.0 ±0.1	4.1 ±0.2	4.2 ±0.1	4.1 ±0.1

Table 4.6 Repeatability study of TiO_2 films – repeated measurement on the same sample.

From the repeatability test, it can be observed that the photoactivity and crystallinity of the TiO_2 films was not affected through repeated use for degrading organic contaminations on the film surface. This demonstrated the robust nature of APCVD deposited TiO_2 films.

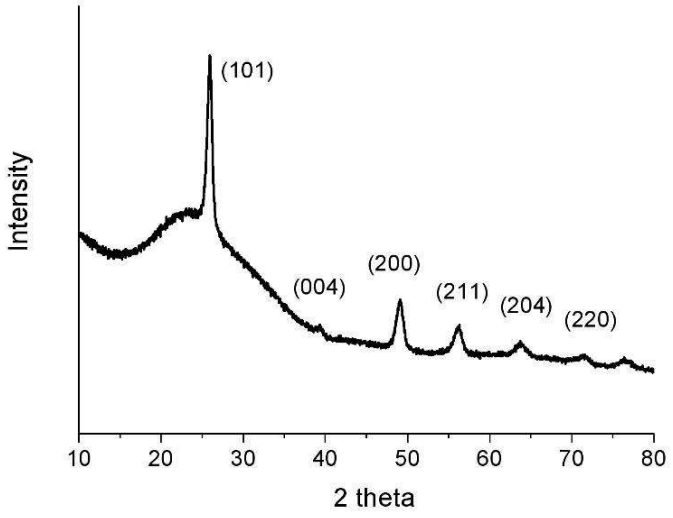

Figure 4.9 XRD analysis of TiO_2 films after stearic acid degradation.

4.7 Photocatalytic degradation of ethyl cellulose with TiO_2 films

The photocatalytic property of APCVD deposited TiO_2 films was reaffirmed using ethyl cellulose as a second organic pollutant. The experimental procedure for ethyl cellulose degradation test followed that of stearic acid test. Figure 4.10 shows the decrease in integrated area of ethyl cellulose peaks with UV illumination time. A blank piece of microscope slide was used as a control sample which showed little effect to the degradation of ethyl cellulose under UV illumination. On the other hand, a steady decrease in integrated area was observed for ethyl cellulose deposited on TiO_2 films. The average degradation rate of ethyl cellulose was calculated to be $5.3 \pm 0.1 \times 10^{-3}$ $cm^{-1}min^{-1}$. With the degradation of ethyl cellulose and stearic acid, the photocatalytic property of APCVD deposited TiO_2 films was assured.

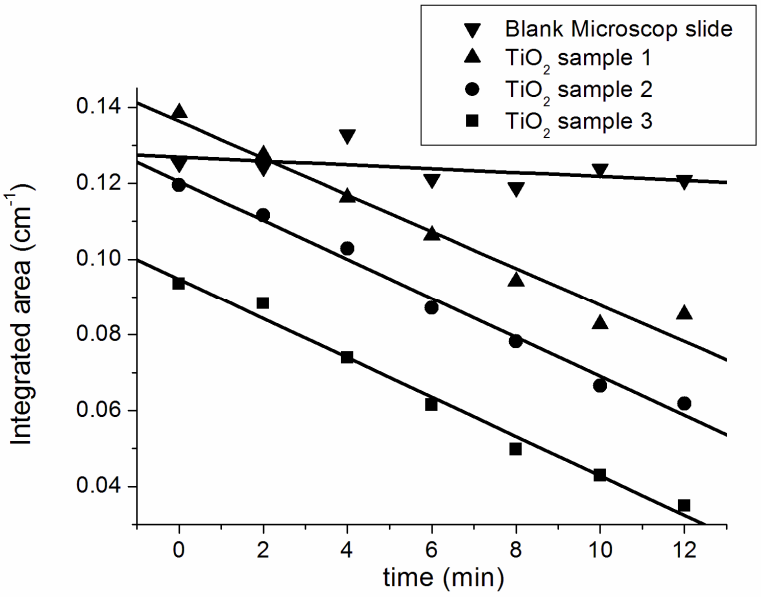

Figure 4.10 Degradation of ethyl cellulose on TiO_2 films under UV light illumination.

4.8 Conclusion

The effect of various deposition parameters on the growth rate of TiO_2 films was studied and optimized. The deposited films showed only anatase phase and grew via Volmer Weber mode. 240 nm SiO_2 barrier layer was pre-coated onto the soda lime glass to prevent sodium poisoning of TiO_2 films. Stearic acid test showed that the photocatalytic reaction rate reached a plateau with 60 nm of TiO_2 film. The TiO_2 films showed good repeatability and reproducibility of the stearic acid test. Photocatalytic test carried on TiO_2 films using ethyl cellulose reaffirmed the photocatalytic property of TiO_2 films.

Chapter 5: Effect of thermal annealing on photocatalytic effect of TiO_2 films

Anatase TiO_2 experiences a phase transformation to rutile phase with annealing under high temperature. Research had shown that a mix phase of anatase and rutile, such as Degussa P25, exhibited enhanced photocatalytic property compared to the respective pure phase [115]. The higher photoactivity is ascribed to the improved charge separation of electrons and holes, which reduced the recombination of the electron-hole pairs [8]. In this chapter, the effect of post-annealing on the microstructure and photocatalytic properties of the APCVD deposited TiO_2 films was investigated. The TiO_2 films were annealed with both conventional tube furnace and rapid thermal annealing process. Crystallinity and surface morphology were characterized using XRD and AFM. Optical bandgap of the TiO_2 films was calculated through the UV-Vis measurements. XPS was used to determine the chemical state of the annealed films and stearic acid test was used to characterize the photocatalytic property of the films.

5.1 Conventional tube furnace

60 nm of TiO_2 film were deposited on quartz glass through the APCVD system as described in Chapter 4. The films were annealed under simulated air ambient, at N_2 to O_2 ratio of 4:1, using Lindberg Blue M tube furnace. The annealing was carried out at preset temperatures (600-900 °C) for 1 hour at a ramp rate of 5 °C/min.

5.1.1 XRD analysis of annealed TiO_2 films

The X-ray diffraction (XRD) patterns of the annealed TiO_2 films are presented in Figure 5.1. For all the annealed TiO_2 films, anatase peaks were observed and was the dominant phase. Rutile peaks were only observed for films annealed at 900 ºC where a small rutile peak at 2 theta = 27º ((100) plane) could be observed.

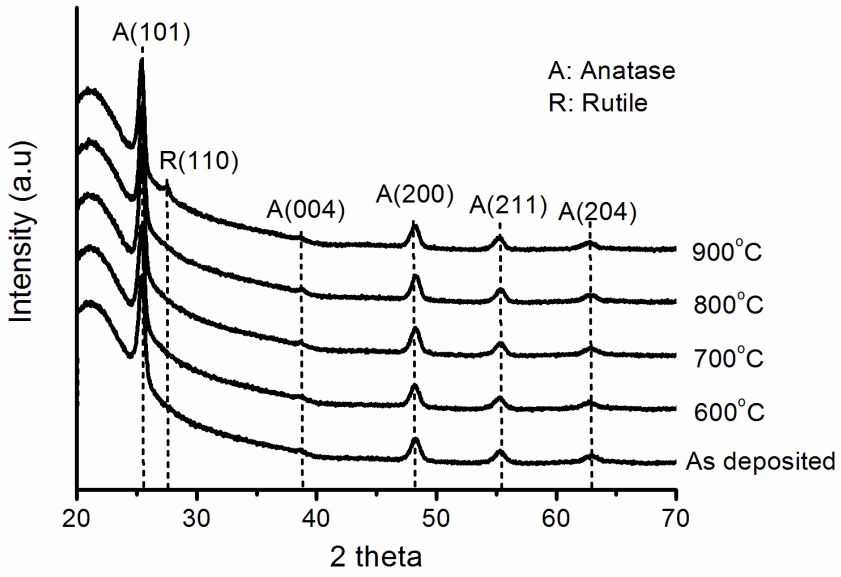

Figure 5.1 XRD spectra of the TiO_2 films after annealed at different temperatures.

The annealing temperature for the anatase to rutile phase transformation process has been reported at a wide range of temperature. It has been reported from a low annealing temperature of 500 °C [116] to as high as 1000 °C [117]. This phase transformation temperature is dependent on the experimental parameters such as deposition methods, deposition temperature and the type of substrate used [118,

119]. For the APCVD deposited TiO_2 films, phase transformation process was only observed at annealing temperature of 900 ℃.

Anatase crystallite sizes, calculated from XRD pattern using Scherrer's equation, are presented in Table 5.1. A small increase in crystallite size from 19.4 nm to 21.0 nm was observed with annealing temperature of 900 °C. This showed that thermal treatment of TiO_2 films has only a marginal effect on the crystal size of anatase.

Samples	Anatase crystallites size (nm)	Surface roughness (rms)
As-deposited	19.4	4.92
600 ºC	19.2	4.98
700 ºC	20.4	5.47
800 ºC	21.7	6.41
900 ºC	21.0	6.08

Table 5.1 Crystallite size of anatase and rutile phase, surface roughness and optical bandgap of the TiO_2 films after annealed at different temperatures.

5.1.2 Optical bandgap measurement of annealed TiO_2 thin films

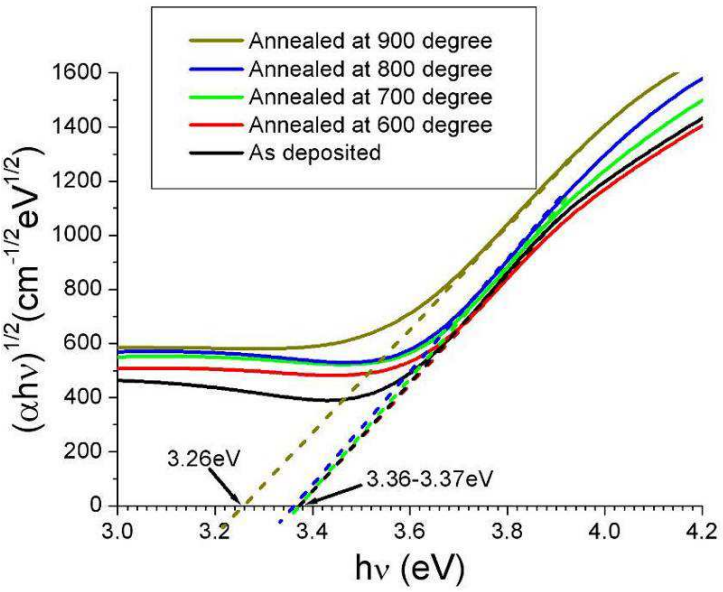

Figure 5.2 UV-Vis absorbance of annealed TiO_2 films at different annealing temperature.

Figure 5.2 presents the bandgap of the respective annealed TiO_2 films. The as-deposited films showed a bandgap of 3.37eV, which was higher than the bulk TiO_2 (3.2 eV). This was due to quantum effect from nanocrystalline TiO_2 thin films [97]. With annealing, the bandgap remained constant up to an annealing temperature of 800 ºC. At 900 ºC, a decrease in bandgap was observed. This was attributed to the presence of rutile phase within the films. This result reaffirmed that the phase transformation from anatase to rutile occurred only at annealing temperature of 900 ºC.

5.1.3 Surface topography of the annealed TiO_2 films

Surface morphology of the annealed TiO_2 films was observed via AFM (Figure 5.3). The as-deposited films showed Volmer-Weber growth with an average grain size of 40 nm. The grains remained unchanged for films annealed at 600 ºC but were observed to grow at annealing temperature of 700 ºC. Further increase in grain size was observed with films annealed at 800 and 900 ºC reaching an average diameter of more than 100 nm.

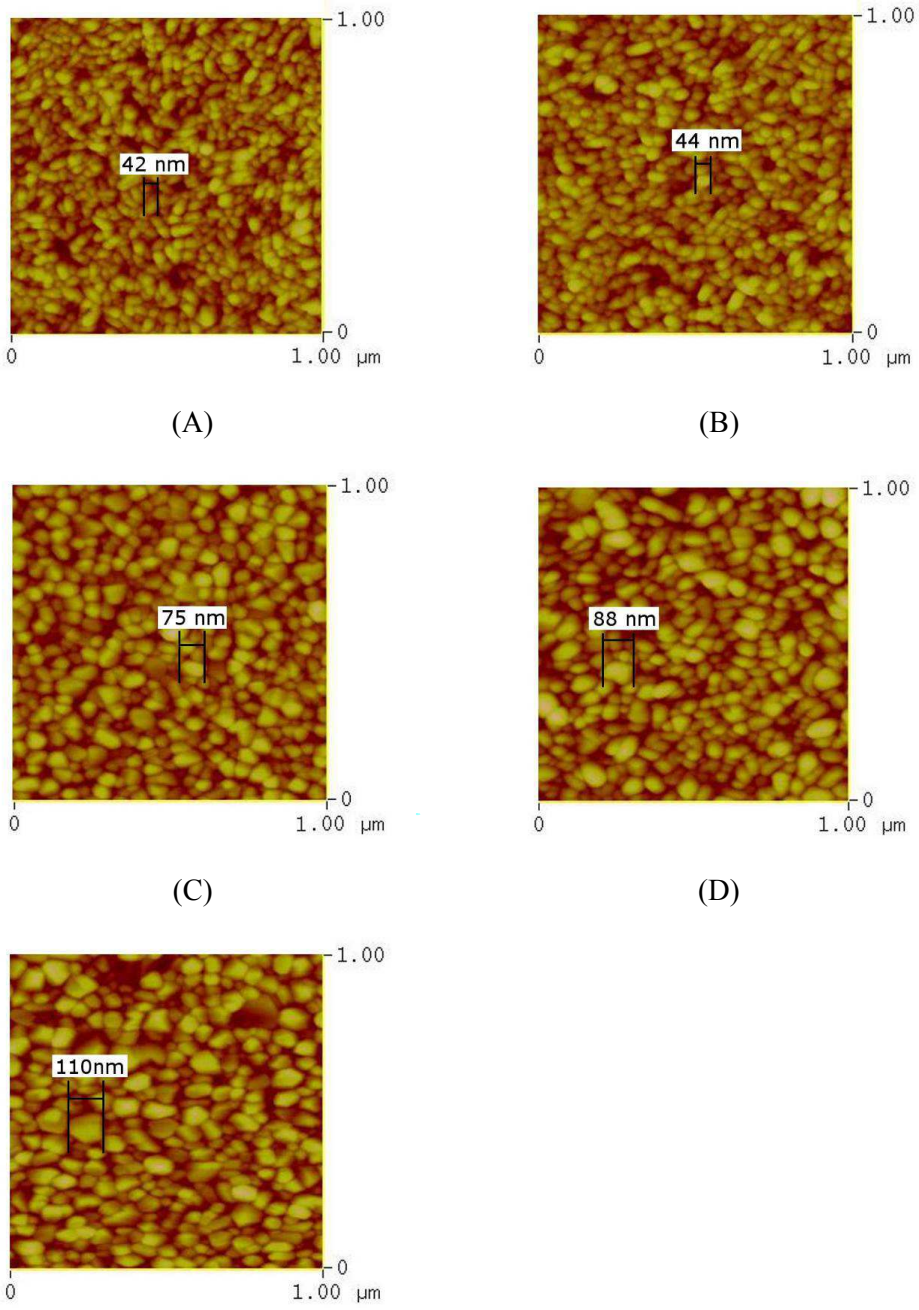

Figure 5.3 AFM images of the as-deposited films (A), and films after annealing at different temperature: 600°C (B), 700°C (C), 800°C (D), and 900°C (E).

Table 5.1 presents the surface roughness of the annealed TiO_2 calculated from the AFM images. Surface roughness remained relatively unchanged with annealing at 600 ºC. However, as the annealing temperature increased to 700 ºC, an increase in surface roughness was observed. This increase was due to growth of anatase grains. The surface roughness reached a maximum at annealing temperature of 800 ºC before decreasing at 900 ºC as rutile grains were formed.

SEM image (Figure 5.4) over a larger region captured the presence of large grains which was only observed for films annealed at 900 ºC. These grains were likely to be rutile phase as it coincided with the appearance of rutile peaks detected by XRD (Figure 5.1)

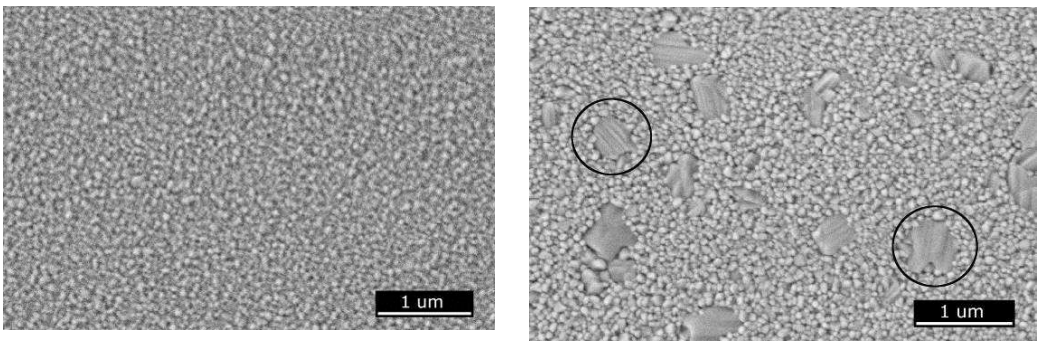

(A) (B)

Figure 5.4 SEM image of TiO_2 films annealed at 800 °C (A), and 900 °C (B). Films annealed at 900 °C shows large grains which are likely to be rutile grains (circle).

5.1.4 XPS analysis of annealed TiO_2 films

Detailed Ti 2p and O 1s XPS spectra of the as-deposited TiO_2 films and the films after annealed at 900 ºC are shown in Figure 5.5 and Figure 5.6. Peaks were observed at 458.6 and 464.3 eV for the as-deposited films, which corresponded to

Ti $2p_{3/2}$ and $2p_{1/2}$ [17]. No additional peaks or peaks shift was observed for the annealed samples. This showed that Ti^{3+} ions were not produced during the thermal treatment.

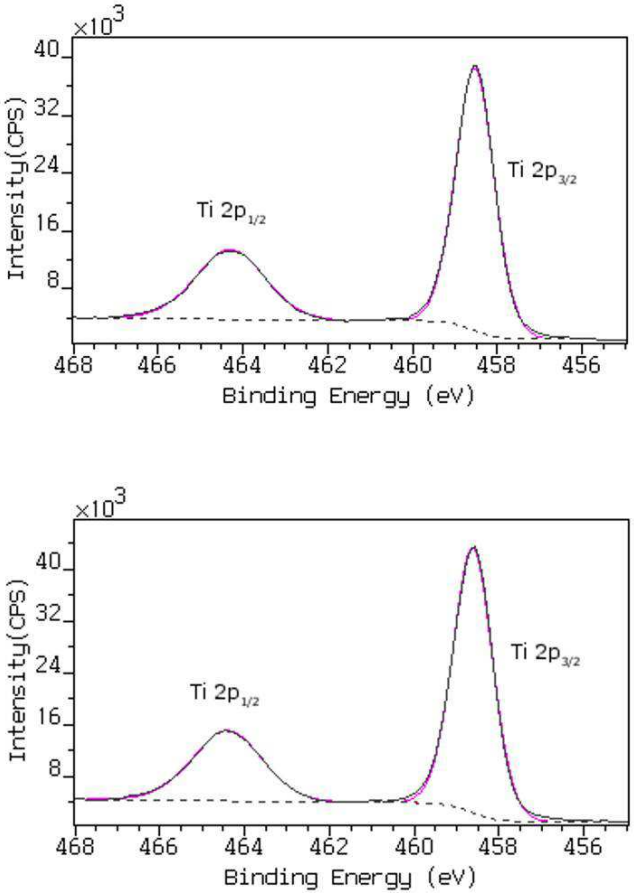

Figure 5.5 High resolution Ti 2p XPS spectra of the as-deposited TiO_2 films (top) and the films after annealed at 900°C (bottom), respectively. CPS: counts per second.

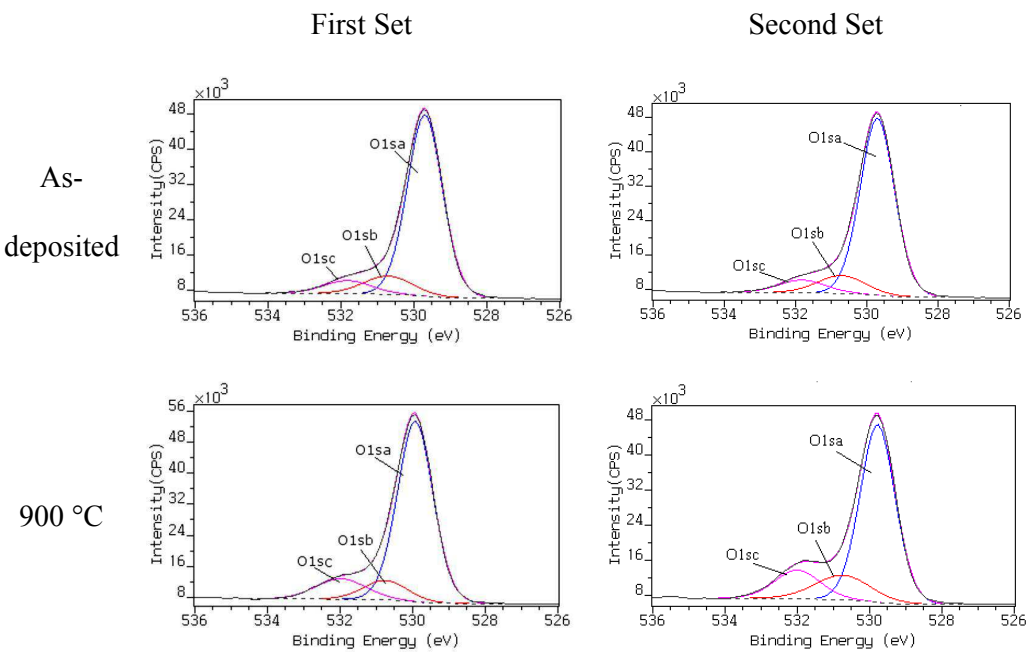

Figure 5.6 High resolutions O 1s XPS spectra of the as-deposited TiO_2 films and the films after annealed at 900 °C, respectively. CPS: counts per second.

Two sets of experiments were carried out for the O 1s spectra (Figure 5.6). The O1s spectra can be deconvoluted into three peaks, with binding energy at 529.6 eV, 530.7 eV and 531.8 eV respectively. According to Dupin et al. [120], the peak at 529.6 eV was assigned to TiO_2 lattice oxygen, O^{2-}, while the other two minor peaks were assigned to hydroxyl ions (530.7 eV) and O^- subsurface defects (531.8 eV). Both sets of experiments (Figure 5.6) shows that the high temperature annealing of TiO_2 films result in an increase of O^- subsurface defects in the TiO_2 film. This is observed from the increase in the O1sc peaks relative to the lattice O^{2-} peaks (O1sa).

The percentage atomic concentration of the respective oxygen species were presented in Table 5.2. From the as-deposited sample to the sample annealed at 600

ºC, a decrease in the OH^- concentration was observed. This decrease was due to the removal of hydroxyl groups from the film's surface [121]. Little change was observed with annealing temperature of 700 ºC. However, at 800 and 900 ºC, a decrease in O^{2-} concentration was observed. This decrease was due to an increased concentration of OH^- and O^- ions in the annealed TiO_2 films.

Samples	O1sa	O1sb	O1sc
As-deposited	80.7	11.4	7.9
600 ºC	84.5	7.4	8.0
700 ºC	83.9	7.8	8.3
800 ºC	70.0	15.4	14.6
900 ºC	77.3	10.3	12.4

Table 5.2 Atomic concentration (%) of O1sa (O^{2-}), O1sb (OH^-) and O1sc (O^-).

The increase in O^- ions in the annealed TiO_2 films was caused by two phenomena occurring: 1) thermal generation of electron-hole pairs [122] and 2) diffusion of Ti^{3+} ions to the films surface forming new TiO_2 layers. During annealing, electrons and holes generated thermally reacted with lattice oxygen and titanium to form O^- and Ti^{3+} ions (equations 5-1 and 5-2) [123].

$$O^{2-} + h^+ \rightarrow O^- \quad (5\text{-}1)$$

$$Ti^{4+} + e^- \rightarrow Ti^{3+} \quad (5\text{-}2)$$

While the process is reversible upon cooling, however, during the high annealing process, Ti^{3+} ions could diffuse through the TiO_2 films. Oxygen ions, on the other hand, remain relatively immobile in its lattice position [124]. The diffused Ti^{3+} ions react with oxygen from the atmosphere and form new TiO_2 layers on its surface. Such formation of new TiO_2 layers was first observed in rutile as single crystal rutile was more readily available [125]. With similar oxidation of Ti^{3+} to Ti^{4+} observed for anatase, the same mechanism for new TiO_2 layers formation has been proposed for anatase [126]. As a result of Ti^{3+} diffusion and formation of new TiO_2 layers, an increase in O^- ions was detected by XPS while Ti^{3+} ions remained undetected.

The increase in O^- subsurface defects also promotes the formation of OH^- ions. Through incorporation of protons, O^- defects situated near to the surface are stabilized, and form hydroxyl ions [127]. This increase in OH^- ions was similarly observed by XPS (Table 5.2) for films annealed at 800 and 900 ºC. Thus, the XPS analysis showed that thermal treatment of TiO_2 films has led to defect formation (O^- and OH^-) within the films.

5.1.5 Photocatalytic reaction of annealed TiO_2 films

The degradation rates of stearic acid by the TiO_2 films annealed at different temperature are presented in Figure 5.7. The error bars in Figure 5.7 and other figures in this thesis represent the standard error of the sampling distribution and are obtained from 3 repeated measurements. Three samples were prepared and tested for each annealing temperature. The stearic acid degradation rate showed similar photoactivity for the as-deposited films and films annealed at 600 ºC. A decrease in

photoactivity was observed as the annealing temperature increased to 700, 800 and 900 ºC. This decrease in photoactivity occurred despite the fact that rutile phase was not observed in films annealed at 700 and 800 ºC.

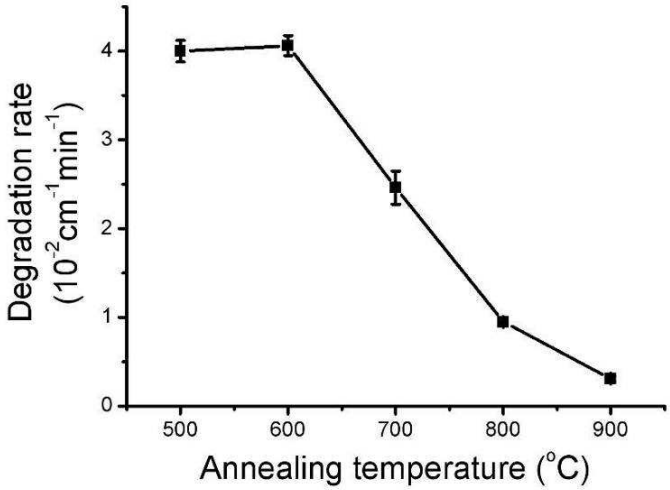

Figure 5.7 Stearic acid degradation rates as a function of annealing temperature.

From the photocatalytic test, the decrease in photoactivity for the annealed TiO_2 films occurred in two stages. The first stage occurred before the anatase to rutile phase transformation at annealing temperature of 700 and 800 ºC. The second stage occurred with the formation of rutile phase, which further reduced the photoactivity of the films. For the second stage, the reduction of photoactivity was caused by the formation of large rutile grains (diameter > 200 nm) in the anatase films. The large rutile grains limited the transfer of electrons and holes between anatase and rutile [8], which led to a decrease in photoactivity.

For the first stage, two factors could be related to the decrease in photoactivity; increase in grain size and defects formation. For grain size effect, the increase in

grain size was observed at annealing temperature of 700 ºC, which coincided with the decrease in photoactivity. As the deposited films had an island structure, grain growth would reduce the surface area of the islands which adversely affected the photoactivity of the films. However, with the grain size increased to twice its original size, it could not account for the 75 % decrease in photoactivity experience by films annealed at 800 ºC. As such, it was not the sole cause of decline in photoactivity.

For defects formation, 3 types of defects could be formed during the annealing process; O^- subsurface defects, OH^- ions and Ti vacancies. Both O^- defects and Ti vacancies are recombination sites which results in recombination of electrons and holes. O^- anion is a hole trapping site where holes are trapped by low coordinated lattice O^{2-} [128, 129]. This leads to recombination with photogenerated electrons causing a decrease in photoactivity. Such reduction in photoactivity was observed in the degradation of trichloroethylene using nanostructure TiO_2 particles [130]. Ti vacancies, on the other hand, introduced acceptor defect state in the TiO_2 bandgap, at 1.15 eV above the valence band [131]. It also caused electrons and holes to recombine and a decrease in photoactivity [132, 133]. As a result of O^- defects and Ti vacancies, recombination centers were introduced to the annealed TiO_2 films, which reduced the degradation rate of stearic acid.

Thus the effect of annealing resulted in grain growth and defects formation in the APCVD deposited TiO_2 films. This adversely affected the photocatalytic property of the annealed films. Further annealing at higher temperature would result in the formation of large rutile grains, which further decreased its photoactivity.

5.2 Rapid thermal annealing

With the increase in grain size and defects formation caused by conventional tube furnace, rapid thermal annealing (RTA) was used to initiate the phase transition process in TiO_2 films. RTA uses fast ramp rate and short annealing time to reduce the diffusion of atoms during the annealing process. This could prevent the growth of TiO_2 grains and formation of O^- defects. As such, the effect of rapid thermal annealing on the photocatalytic property of TiO_2 films was investigated.

5.2.1 Effect of annealing temperature on anatase to rutile phase transformation

To analyze the effects of annealing temperature on the anatase to rutile phase transformation, the TiO_2 films were annealed at a ramp rate of 15 °C/sec for 60 sec at different annealing temperature (800-1000 °C). Figure 5.8 shows the XRD analysis of the annealed TiO_2 films.

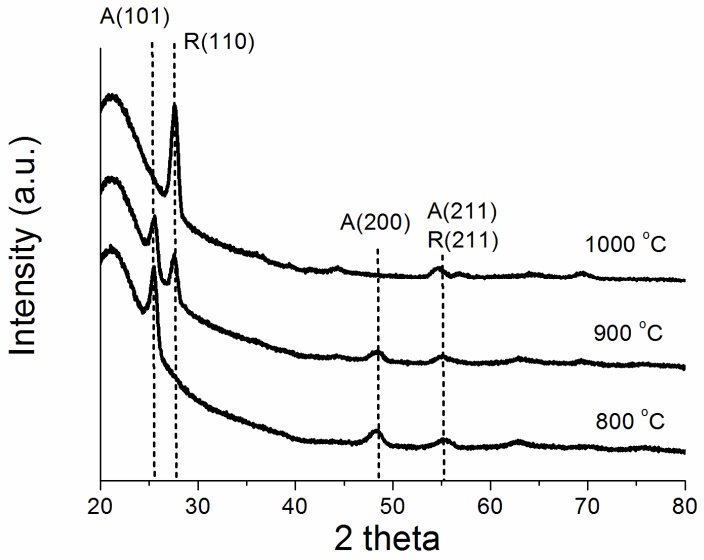

Figure 5.8 XRD analyses of TiO_2 films annealed at various temperatures using rapid thermal annealing.

In agreement with thermal annealing with conventional tube furnace, phase transformation of anatase to rutile was only observed at annealing temperature of 900 °C. At 800 °C, the films remained as pure anatase films. Rutile peaks were observed with annealing temperature at 900 °C and complete transformation into rutile was observed at annealing temperature of 1000 °C. For films annealed at 900 °C, the formation of rutile phase appeared to be more rapid with rapid thermal anneal than with conventional furnace. This was despite the short annealing time and could be due to the fast ramp rate used in rapid thermal annealing.

5.2.2 Effect of annealing time on anatase to rutile phase transformation

With the appearance of rutile phase at annealing temperature of 900 °C, the effect of annealing time on the phase transformation of TiO_2 films was investigated. The

TiO_2 films were annealed at 900 °C at a ramp rate of 15 °C/sec for 10 to 60 seconds. Figure 5.9 shows the XRD analysis of the annealed TiO_2 films while Table 5.3 shows the weight fraction of anatase in the TiO_2 films. Weight fraction of anatase were calculate based on equation 5-3 [134].

$$x_a = \frac{1}{1 + 1.265(\frac{I_r}{I_a})} \tag{5-3}$$

where x_a is the weight fraction of anatase, and I_a and I_r are the XRD intensity of anatase (101) and rutile (110) peaks.

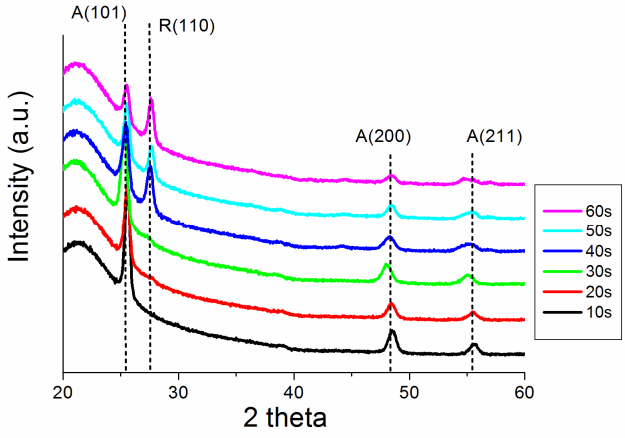

Figure 5.9 XRD analyses of TiO_2 films annealed at 900 °C for 10-60 seconds using rapid thermal annealing.

Annealing time (s)	Weight fraction of anatase (%)
10	100
20	94.6
30	95.2
40	53.7
50	58.4
60	39.9

Table 5.3 Weight fraction of Anatase in TiO_2 films annealed using rapid thermal annealing.

With 10 seconds of annealing time, phase transformation was not observed as only anatase was detected by the XRD. At 20 and 30 seconds of annealing time, a small rutile peak can be observed. This corresponded to 4-5 % rutile in the TiO_2 films. At 40 seconds of annealing time, a drastic increase in the rutile peaks was observed with almost 50 % of the anatase phase converted into rutile. Further annealing showed a smaller increase in rutile phase with 60 % anatase converted after 60 seconds of annealing. From the XRD analysis, the formation of rutile phase proceeded at a slow pace initially before experiencing a rapid transforming into rutile phase. After the fast transformation, the phase transformation rate again proceeded at a slower pace.

The rutile phase transformation process was also observed from UV-Vis spectrum. Red-shifted in the UV-Vis spectrum was observed and a decrease in optical

bandgap was found. Figure 5.10 shows the decrease in bandgap determined from the UV-Vis spectrum with annealing time of the TiO_2 films. The decrease in optical bandgap confirmed the presence of rutile phase as rutile has a lower bulk bandgap of 3 eV compared to anatase 3.2 eV.

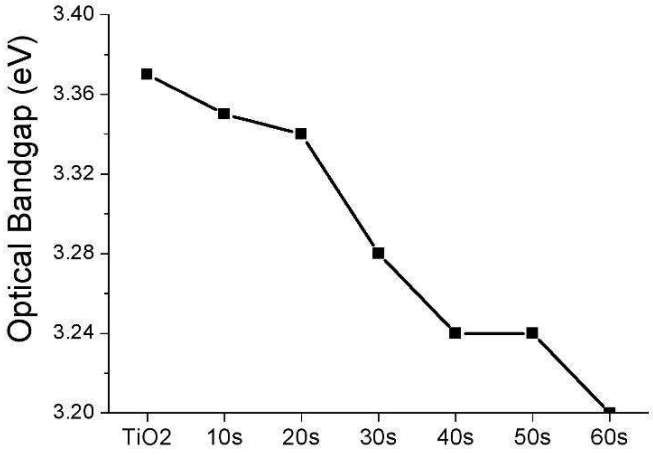

Figure 5.10 Decrease in TiO_2 bandgap with increasing annealing time.

5.2.3 Surface topography of annealed TiO_2 films (RTP)

Figure 5.11 shows the AFM images of the annealed TiO_2 films. Despite the short annealing time and fast ramp up time, growth of TiO_2 grains was still observed. With 10 seconds of annealing time, the size of TiO_2 anatase grains was comparable to films annealed by conventional tube furnace at 700 °C. With increase in annealing time, further increase in the anatase grains was observed. This showed that even with rapid thermal annealing, the growth of TiO_2 grains could not be suppressed. Furthermore, rutile grains produced with rapid thermal annealing were large and comparable to those annealed with conventional tube furnace. With the

large rutile grains produced, it should be expected that the annealed films would not exhibit enhanced photoactivity through heterojunction semiconductor effect.

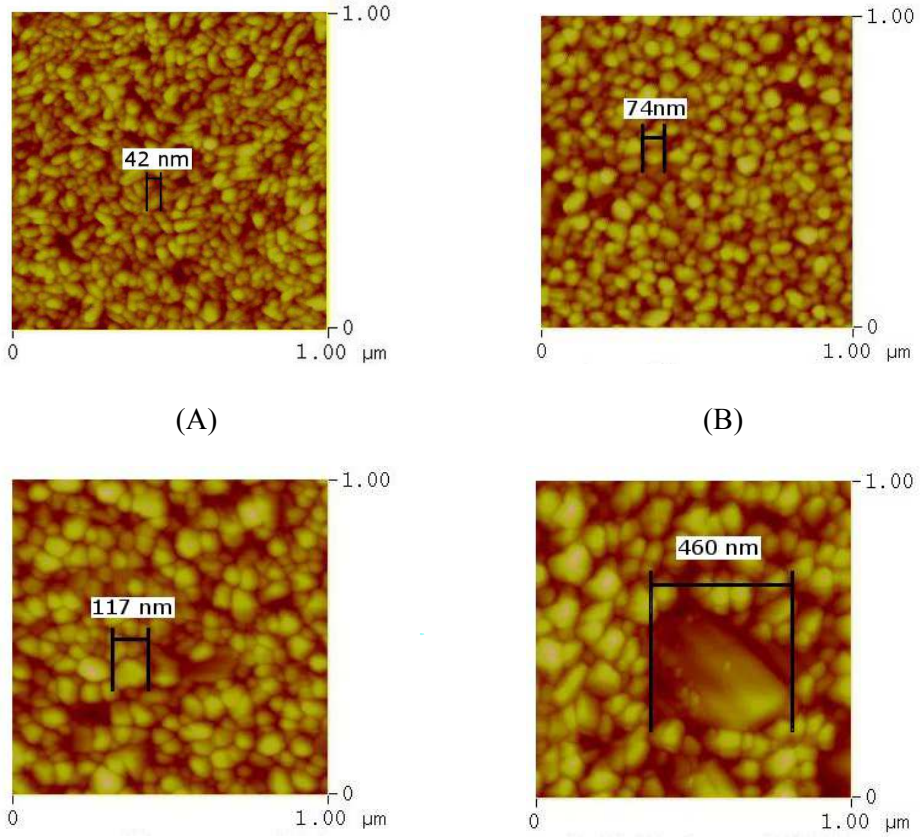

Figure 5.11 AFM images of the as-deposited films (A), and films after annealing with rapid thermal annealing at different annealing timer: 10 s (B), 30 s (C), and 60s (D).

5.2.4 Photocatalytic reaction of annealed TiO_2 films (RTP)

With the growth of anatase grains, a decrease in stearic acid degradation rate was observed (Figure 5.12). This reduction in degradation rate was observed even with only 10 second of annealing time, where rutile phase were yet to be formed. Such observation was similar to that for TiO_2 films annealed in tube furnace. Thus, this

showed that annealing TiO_2 under rapid thermal annealing produced similar effects as conventional tube furnace which resulted in deterioration of photocatalytic property of the films.

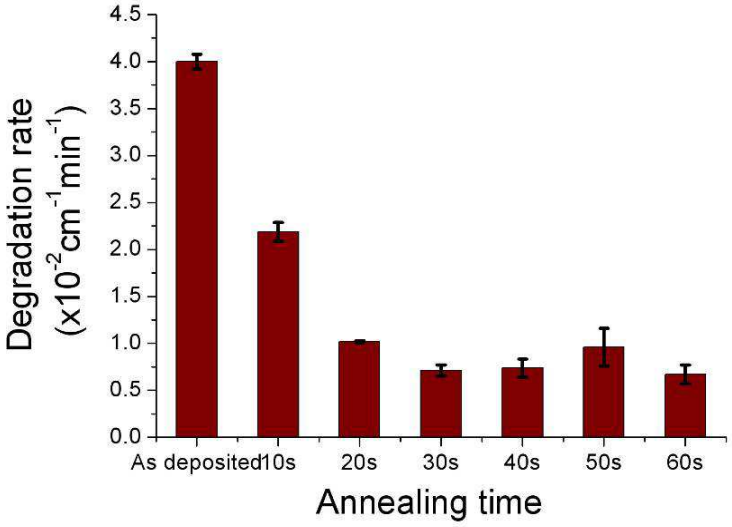

Figure 5.12 Stearic acid degradation rates for films annealed with rapid thermal annealing.

5.3 Conclusion

Thermal annealing of TiO_2 films had shown a decrease in photocatalytic reaction rate. The decrease in reaction rate occurred in 2 stages; 1) grain growth and formation of subsurface defects followed by 2) formation of large rutile grains. The formation of subsurface defects was due to the diffusion of Ti^{3+} ions, which formed new TiO_2 layers with atmospheric oxygen. This led to the formation of O^- subsurface defects and OH^- ions which act as recombination centers for photo-induced electrons and holes. Coupled with grain growth, they resulted in a decrease in photocatalytic reaction rate. Further decrease in photoactivity was due to

formation of large rutile grains with limited heterojunction semiconductor effect with anatase phase. Grain growth and formation of large rutile grains were similarly observed with rapid thermal annealing, which showed similar deterioration of photocatalytic degradation of stearic acid.

Chapter 6: Embedding particles in TiO_2 coating for enhanced photocatalytic effect

Embedding particles in TiO_2 films has the effect of enhancing the photocatalytic property of the films or provide additional functionality such as visible light photocatalytic property. In this chapter, the photocatalytic properties of TiO_2 films embedded with anatase, rutile, P25 and $SrTi_{1-x}Fe_xO_{3-\delta}$ particles were investigated. The TiO_2 films were embedded with particles through spraying of particle dispersion on the substrate followed by TiO_2 film deposition via APCVD. Anatase, rutile and P25 particles were embedded in TiO_2 films to investigate the effects on UV light photocatalytic property while a novel material, $SrTi_{1-x}Fe_xO_{3-\delta}$, was tested for its visible light photocatalytic capabilities. The particle dispersions were characterized for their particle size and zeta potential while the films embedded with particles were characterized for its surface area and surface coverage of its particles. Photocatalytic property of the embedded particle films was analyzed with stearic acid under either UV or visible light illumination.

6.1 Anatase, Rutile and P25 embedded TiO_2 films

Rutile, Anatase and P25 particles were embedded in TiO_2 films to improve the UV photocatalytic property of TiO_2 films. While the rutile particles formed heterojunction semiconductor with the TiO_2 the anatase particles increased the surface area of the TiO_2 films. P25, on the other hand, had a higher photocatalytic property than anatase or rutile particles [135]. As such, embedding P25 could

improve the photocatalytic property of TiO_2 films. Here, the effect of embedding anatase, rutile and P25 on the UV light photocatalytic effect of TiO_2 films was investigated.

6.1.1 Particle size distribution and stability for Anatase, Rutile and P25

To embed particles in the TiO_2 films via spray with APCVD, the particles were first dispersed in a solvent. However, particles tend to agglomerate when dispersed in a solvent. This is caused by constant collision between particles (Brownian motion) and attractive forces, such as Van der Waals forces, which binds the particles together. Large particles have a lower photocatalytic effect due to the reduced surface area for the transfer of photogenerated electrons and holes. To prevent the agglomeration of particles, repulsive forces, such as electrostatic charges, may be introduced to the particle surface to keep the particles apart. This can be carried out by adjusting the pH of the solution.

Anatase (Aldrich), rutile (Aldrich) and P25 (Degussa) particles were dispersed in various solvent (water, ethanol, iso-propanol and methanol) at a concentration of 0.1 g/liter. The pH of the dispersion was adjusted using acetic acid or ammonia which modified the charge on the particle surfaces. Ultrasonic agitation (Fisher Scientific sonic dismembrator model 500) was applied to the dispersion for 3 minutes to reduce the particle size in the dispersion. Particle size of dispersions was measured using the Malvern Instrument Zetasizer Nano-ZS.

Figure 6.1 shows the average particle sizes of anatase dispersed in various solvents under different pH conditions. Under the right pH condition, the various anatase

dispersions were able to achieve a particle size of ≈ 150 nm. For organic solvents (methanol, ethanol and IPA), the dispersion showed good stability in the acidic region but agglomerated at neutral to alkaline region. For water, the dispersion showed small particle size under the conditions of extreme acidic or alkaline pH. The particle size increased at neutral and slightly acidic region. The smallest particle size achieved was 150 nm.

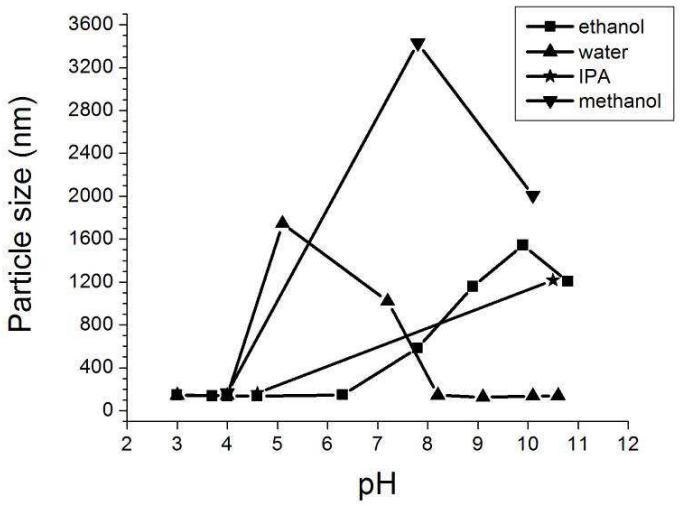

Figure 6.1 Average anatase particle size dispersed in different solvent under different pH condition.

For rutile dispersions (Figure 6.2), particles remained relatively large, at 260 nm, as compared to anatase particles. Particles were reduced in size in the alkaline region when dispersed in methanol. For ethanol, effective size reduction was achieved at both high acidic and alkaline pHs. In water, the particles remained small at neutral to alkaline region while particle size remained significantly large when dispersed in IPA.

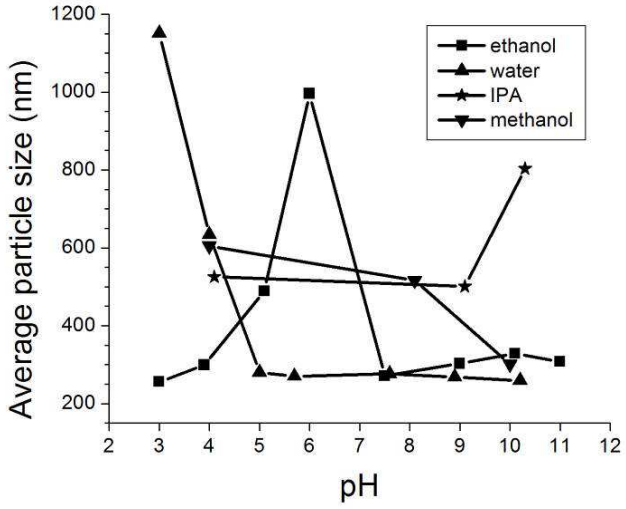

Figure 6.2 Average rutile particle sizes dispersed in different solvent under different pH condition.

P25 particles comprise a majority of anatase phase with some rutile phase. As such, its particle size would be expected to show similar trends to those of anatase. Zetasizer measurement (Figure 6.3) shows that P25 dispersed well in ethanol at neutral and acidic region and at both extreme acidic and alkaline region for water. Its average particle size reached a minimum of 200 nm.

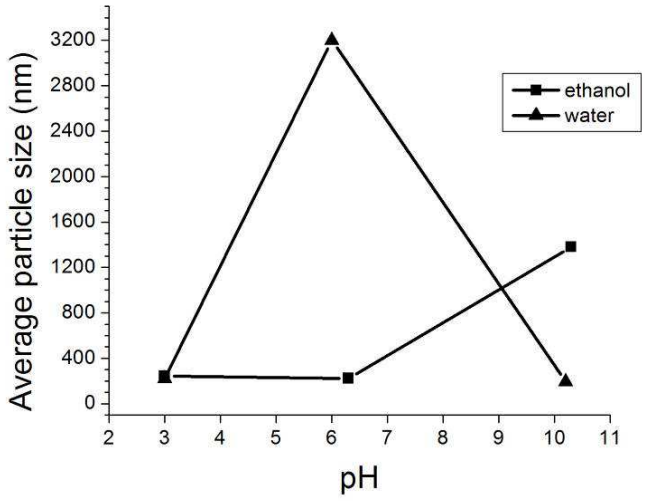

Figure 6.3 Average P25 particle size dispersed in different solvent under different pH condition.

To ensure that the particles do not agglomerate over time, a settling test was carried out for particles dispersed in water at pH 3 for anatase and P25, and at pH 10 for rutile. Dispersions were left undisturbed for a period of time before testing their particle size. Table 6.1 shows the particle size after settling. The results showed that the particle dispersions were stable and remained relatively unchanged over a period of 5 days. Rutile and P25 dispersions showed a slight decrease in the particle size probably due to large particles settling to the bottom of the container.

Zeta potential measurements also showed good dispersion stability in the various dispersions (Table 6.1). All dispersions had a zeta potential value of $\geq$ 40 mV which represented good to excellent stability under the ASTM standard D 4187-82.

	Particle size (nm)				Zeta Potential at day 0 (mV)
Dispersion	0 day	1 day	2 day	5 day	
Anatase	164	173	160	170	40
Rutile	261	268	248	221	-54
P25	233	221	218	202	53

Table 6.1 Particle size after settling test and zeta potential measurement of anatase, rutile and P25 dispersions.

From the particle size analysis, the smallest particle size achieved for anatase, rutile and P25 were 150, 260 and 200 nm respectively. For anatase and P25, the particles were dispersed in water at pH 3 with 3 minutes of ultrasonic agitation. For rutile, the particles were dispersed in water at pH 10 with 3 minutes ultrasonic agitation.

6.1.2 Embedding Anatase, Rutile and P25 particles in TiO_2 films through spray and APCVD

Using the various particle dispersions, particles (anatase, rutile and P25) were embedded in TiO_2 films through spray and APCVD deposition. The dispersions were sprayed onto the substrate for 1, 2 and 4 cycles. 2 cycles of TiO_2 films (35 nm) were deposited on top of the particles to act as matrix binding onto the particles. 35 nm of TiO_2 films was used so as to avoid the photocatalytic saturation limit of TiO_2 films and allowed electrons and holes generated in the particles to participate in the photocatalytic reaction.

6.1.3 XRD analysis of embedded particle films

Figure 6.4 shows the XRD analysis of TiO_2 films embedded with 4 cycles of particle spray. For films embedded with anatase particles, only anatase phase was observed. For P25 particles, a small rutile peak at 2 theta = 27.4 ° was observed while for films embedded with rutile particles, both anatase and rutile phase were observed from the XRD analysis.

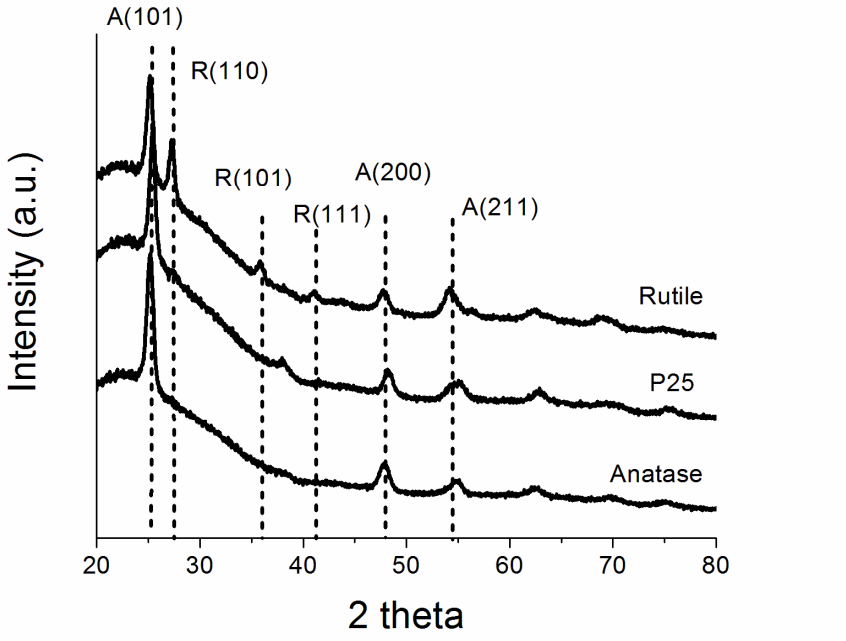

Figure 6.4 XRD analysis of TiO_2 films embedded with 4 cycles of anatase, rutile and P25.

6.1.4 Surface area of particle embedded TiO_2 films

With addition of particles in the TiO_2 films, the film's surface became rougher which could improve its photocatalytic property due to greater sites for transfer of electrons and holes to the organic contamination on the surface. Figure 6.5 shows

the AFM images of the particle embedded TiO_2 films. Films embedded with P25 particles showed a larger concentration of particles as compared to anatase and rutile. This might be related to its small particle size (average size of 238 nm) and dense particles [136] which allowed the particles to stay onto the substrate during the spray process. The AFM images also showed P25 particles having a greater amount of aggregation of the particles with some forming larger particles. Rutile, on the other hand, has a larger particle size with average particle size of 297 nm. This is related to its poor particle dispersion. Anatase shows a better separation of particles as it has the smallest particle size of 193 nm. The particle sizes measured from AFM are slightly larger those measured from zetasizer (Table 6.1) due to artifacts arising from the curvature of the AFM tip.

Surface area of TiO_2 films embedded with particles was determined from AFM measurement. Table 6.2 shows the % surface area difference for films embedded with particles as compared to plain TiO_2 films. The % surface area is defined as the increase in surface area over a flat surface. With an increase in the number of spray cycles, the % surface area difference was observed to increase for the 3 different particles. The increase in % surface area difference was generally proportional to the number of spray cycles except for TiO_2 films with 4 cycles of P25 particles, which shows a smaller increase (14.1% increase) compared to 2 cycles (32.5% increase). This was due to aggregation of particles deposited on the substrate leading to smaller increase in surface area. Films embedded with rutile and anatase generally showed a smaller increase in surface area compared to P25 particles. This was due to the larger amount of particles deposited with P25 dispersion as can be observed from the AFM images. This increase in % surface area difference can

contribute to an increase in photocatalytic property with greater number of sites for transfer of electrons and holes to the organic contamination.

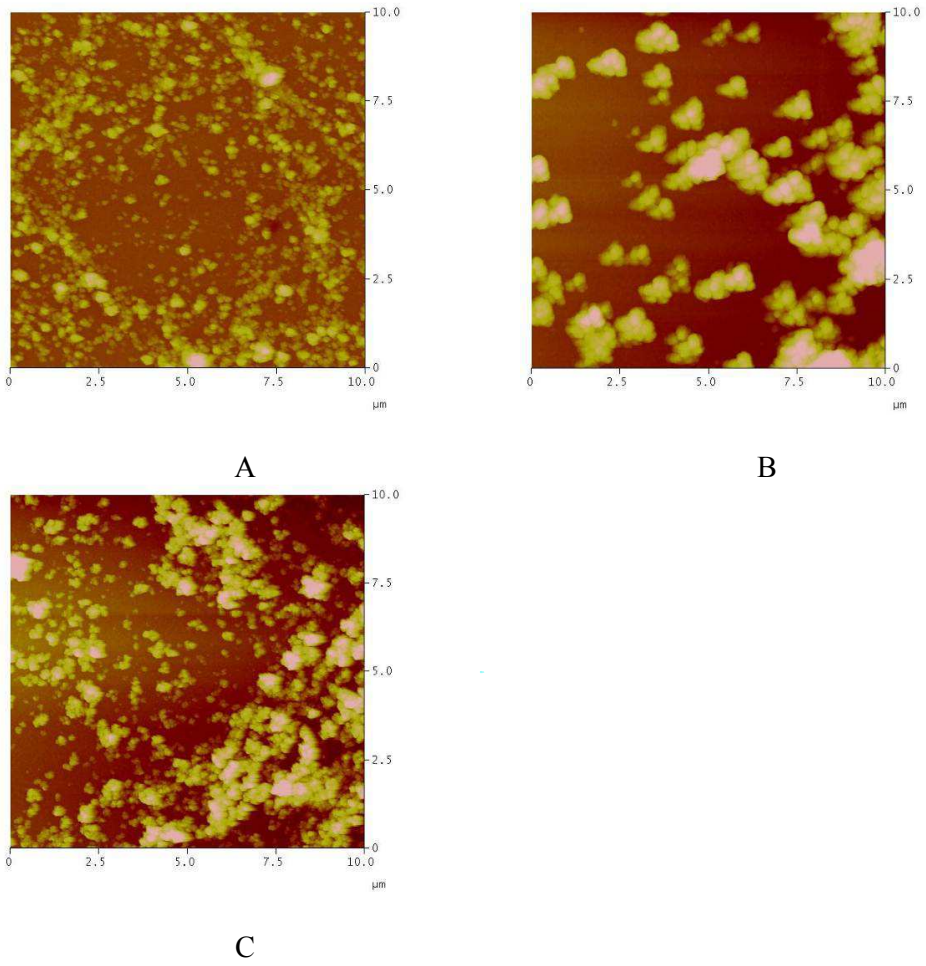

Figure 6.5 AFM images of TiO_2 films embedded with (A) anatase, (B) rutile and (C) P25 particles.

6.1.5 Surface coverage of particle embedded TiO_2 films

Particle surface coverage was determined from the SEM images using ImageJ software. The method of analyzing the surface coverage was detailed in Chapter 3. Table 6.2 shows the average surface coverage of TiO_2 films embedded with particles. The average surface coverage was calculated from the surface coverage of

10 SEM images. Similar to the % surface area difference, with more spray cycles, an increase in the particle surface coverage was observed. Also, films embedded with P25 particles showed greater amount of surface coverage as more particles were sprayed on the substrate. Generally, surface coverage as analyzed by SEM images showed a lower value compared to % surface area difference.

Embedded Particles	No of spray cycles	% surface area difference	Average particle surface coverage (%)
Anatase	1	9.7	6.4
	2	15.8	12.5
	4	33.7	32.7
Rutile	1	8.7	5.1
	2	16.9	12.5
	4	28.7	20.2
P25	1	28.9	21.9
	2	61.2	38.9
	4	75.3	46.9
TiO_2 film	-	2.0	-

Table 6.2 % surface area difference of TiO_2 films embedded with anatase, rutile and P25 particles.

6.1.6 Photocatalytic degradation of stearic acid by TiO_2 films embedded with anatase, rutile and P25 particles

Figure 6.6 shows the photocatalytic reaction rate of TiO_2 films embedded with anatase, rutile and P25 particles. Films embedded with P25 particles showed the greatest improvement to the photocatalytic degradation of stearic acid. The increase in photocatalytic reaction rate was 2 times higher compared to 60 nm of TiO_2 film, which was the highest photocatalytic reaction for plain TiO_2 films. This improvement with embedded P25 particles was due to the high photocatalytic effect of P25 particles itself. Anatase too showed improvement in stearic acid degradation rate with increased particle loading in TiO_2 films. However, the highest photocatalytic reaction rate achieved was 4 $x10^{-2}$ $cm^{-1}min^{-1}$, similar to 60 nm of plain TiO_2 film. Thus, unlike P25 particles, embedded anatase particles could not achieve a higher photocatalytic reaction than 60 nm TiO_2 film. Films embedded with rutile particles showed no effect to the photocatalytic reaction rate of TiO_2 films. The reaction rate remained constant with increase particle loading and was similar to TiO_2 films without any embedded particles (35 nm TiO_2).

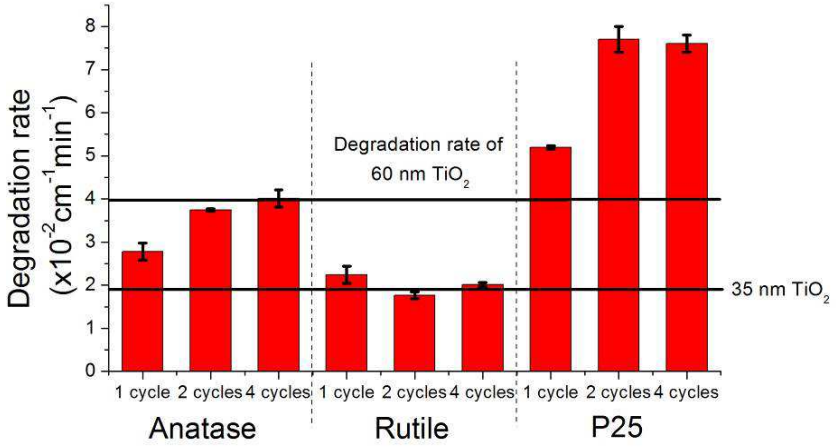

Figure 6.6 Stearic acid degradation by TiO_2 films embedded with anatase, rutile and P25. The two horizontal lines are the degradation rate by 35 nm and 60nm of TiO_2 film (without embedded particles).

From the photocatalytic test, an increase in surface area played a less crucial role to increase in photocatalytic reaction rate compared to the type of particles embedded in TiO_2 films. For films embedded with rutile particles, while an increase in surface area was observed with more embedded particles, the photocatalytic reaction rate remained relatively constant. This was due to the fact that all the electrons and holes generated from the 35 nm of deposited TiO_2 film were participating in the photocatalytic reaction. Thus, the increase in surface area did not result in more electrons and holes engaging in the photocatalytic reaction. For films embedded with 2 and 4 cycles of P25 particles, the degradation rate remained constant which suggested the photocatalytic limit of embedded P25 particle films.

6.2 $SrTi_{(1-x)}Fe_xO_3$ particles embedded in TiO_2 films for visible light photocatalytic reaction

$SrTi_{(1-x)}Fe_xO_3$ particles were embedded in TiO_2 films with the intention of adding visible light capabilities to the TiO_2 films. $SrTi_{(1-x)}Fe_xO_3$ is a solid solution of $SrTiO_3$ and $SrFeO_{3-\delta}$. The bandgap of $SrTi_{(1-x)}Fe_xO_3$ ranges from 1.9 eV ($SrFeO_{3-\delta}$) to 3.2 eV ($SrTiO_3$) depending on the x value for $SrTi_{(1-x)}Fe_xO_3$. With the decrease of bandgap for photocatalytic $SrTi_{(1-x)}Fe_xO_3$, visible light absorption capabilities could be achieved. The synthesized of $SrTi_{(1-x)}Fe_xO_3$ was described in Chapter 3. Here, the particles were named according to their iron content where STF02 represents an x value of 0.2.

6.2.1 XRD analysis of $SrTi_{(1-x)}Fe_xO_3$ particles synthesized by high temperature solid state reaction

$SrTi_{(1-x)}Fe_xO_3$ particles were synthesized using high temperature solid state reaction. The XRD analysis of the synthesized $SrTi_{(1-x)}Fe_xO_3$ particles are shown in Figure 6.7. Only perovskite phase can be observed from the XRD analysis. Peaks for its starting material were not detected. This showed that reasonable pure $SrTi_{(1-x)}Fe_xO_3$ particles were synthesized from the high temperature solid state reaction.

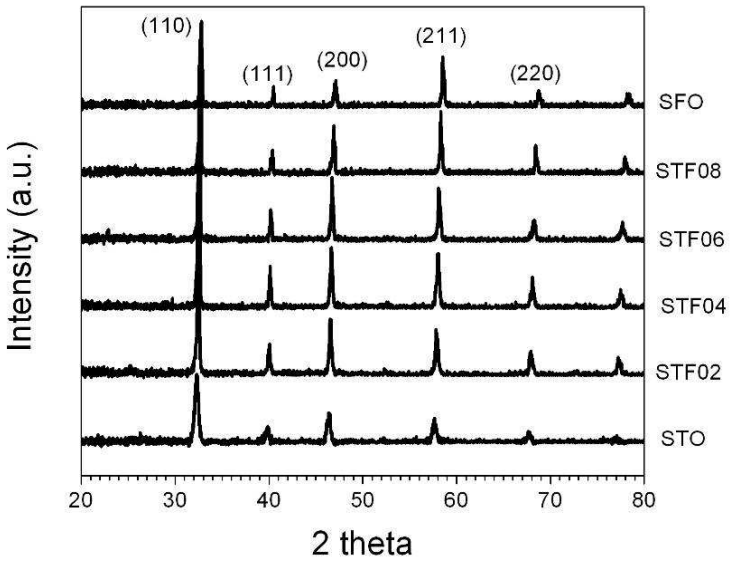

Figure 6.7 XRD analyses of $SrTi_{(1-x)}Fe_xO_3$ particles showing single perovskite phase.

6.2.2 Visible light Methylene Blue photocatalytic test

Methylene blue was used as the organic contaminant to test the visible light photocatalytic property of $SrTi_{(1-x)}Fe_xO_3$ particles. Here, methylene blue was used as it can dissolve in water and can be easily detected using UV-Vis spectrophotometer. The decrease of methylene blue concentration with STF08 particles under visible light illumination was shown in Figure 6.8. With 7 hours of visible light illumination, only 40 % of the original methylene blue was left. In comparison, the control sample (without particles) showed only a slight decrease in concentration which was due to photolysis reaction. From the methylene blue test, it suggested the possibilities of visible light photocatalytic capabilities of $SrTi_{(1-x)}Fe_xO_3$ particles.

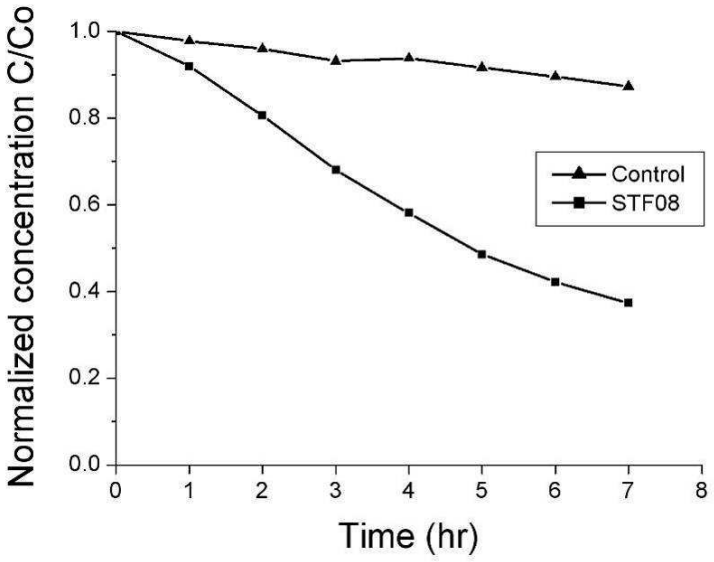

Figure 6.8 Visible light photodegradation of methylene blue with STF08 particles.

6.2.3 Dispersion of $SrTi_{(1-x)}Fe_xO_3$ particles

$SrTi_{(1-x)}Fe_xO_3$ dispersion were prepared in a different method compared to anatase, rutile or P25. As $SrTi_{(1-x)}Fe_xO_3$ decomposed into $SrCO_3$ in water, the particles were dispersed in ethanol using high energy ball milling to reduce the particle size. The balls and bowls used for high energy ball milling were made of yttrium-stabilized-zirconium.

For the dispersion process, 1 g of $SrTi_{(1-x)}Fe_xO_3$ particles was dispersed in 100 ml of ethanol. The dispersion was milled at a milling speed of 350 rpm for 16 milling cycles. Each milling cycle consisted of 10 minute milling with a 5 minute interval for cooling down. After milling, the dispersion was diluted to 1 g/l before used for the spray process.

Table 6.3 shows the average particle size for the different $SrTi_{(1-x)}Fe_xO_3$ dispersions. The dispersions showed an average particle size of between 180 to 300 nm. This was comparable to the anatase, rutile and P25 dispersion in section 6.1.1. Also, the zeta potential values showed good stability of the dispersions. Using the dispersions, $SrTi_{(1-x)}Fe_xO_3$ were embedded in TiO_2 films using the spray and APCVD method.

Particles	Average particle size (nm)	Zeta potential (mW)
STO	294.3	42.5
STF02	233.2	50.8
STF04	290.9	36.4
STF06	256	44.7
STF08	210	50.9
SFO	188.4	52.6

Table 6.3 Average particle sizes and zeta potential of $SrTi_{(1-x)}Fe_xO_3$ particles in ethanol.

6.2.4 XRD analysis of $SrTi_{(1-x)}Fe_xO_3$ particles embedded in TiO_2 films

Figure 6.9 presents the XRD analysis of $SrTi_{(1-x)}Fe_xO_3$ particles embedded in TiO_2 films. Other than the anatase phase detected for TiO_2 films, XRD analysis also showed $SrTi_{(1-x)}Fe_xO_3$ perovskite phase. Peaks such as $SrCO_3$ were not observed.

This showed that the crystallographic phase of $SrTi_{(1-x)}Fe_xO_3$ particles was preserved with no decomposition of particles occurring during the deposition process.

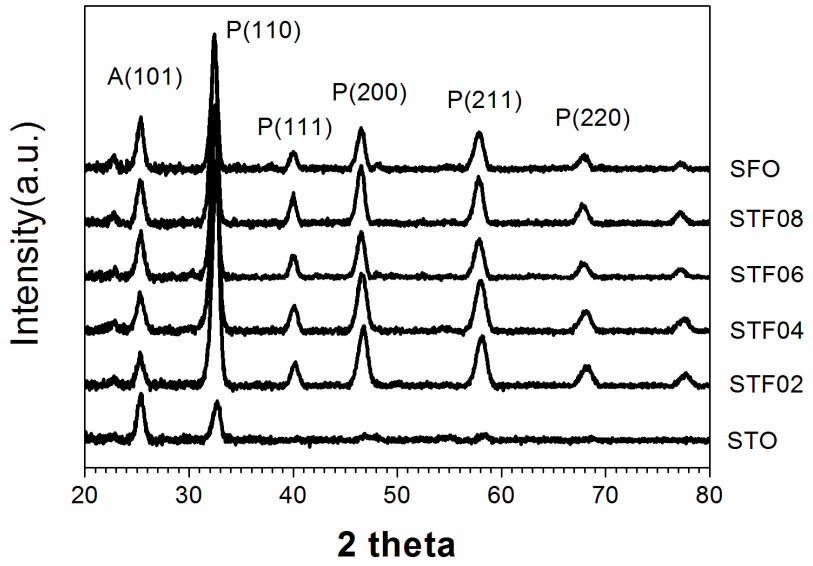

Figure 6.9 XRD analysis of $SrTi_{(1-x)}Fe_xO_3$ particles embedded in TiO_2 films. A: anatase, P: perovskite.

6.2.5 UV-Vis analysis of $SrTi_{(1-x)}Fe_xO_3$ particles embedded in TiO_2 films

Figure 6.10 shows the absorbance spectrum of the TiO_2 films embedded with $SrTi_{(1-x)}Fe_xO_3$ particles. With increasing iron content in the $SrTi_{(1-x)}Fe_xO_3$ particles, the absorbance spectrum showed an increase at higher wavelength (340-440 nm). Films embedded with SFO particles showed a red shift in the absorbance spectrum. While the absorbance spectrum could not confirm the visible light photoactivity of $SrTi_{(1-x)}Fe_xO_3$ particles, it indicated that the particle could absorb longer wavelength light and could be capable of visible light photocatalytic reaction.

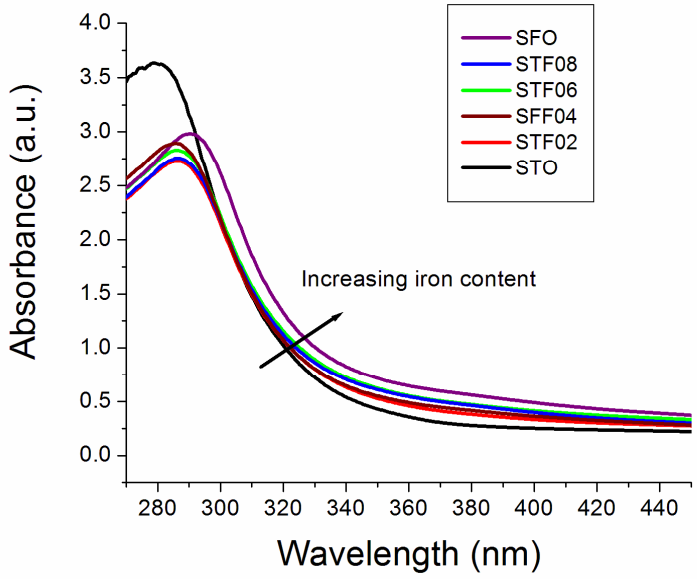

Figure 6.10 Absorption spectra of TiO_2 films embedded with $SrTi_{(1-x)}Fe_xO_3$ particles.

6.2.6 UV light photocatalytic reaction of $SrTi_{(1-x)}Fe_xO_3$ particles embedded in TiO_2 films

Figure 6.11 gives the results of UV light stearic acid tests carried out on embedded particle films. Results were compared to those of plain TiO_2 films. It was observed that $SrTi_{(1-x)}Fe_xO_3$ embedded particle films showed poorer stearic acid degradation as compared to TiO_2 films. This was despite the fact that all the films have 35 nm of TiO_2 film deposited on the substrate. Films embedded with STO particle films were observed to have similar degradation rate as TiO_2 films. With an increase in the iron content in embedded $SrTi_{(1-x)}Fe_xO_3$ particle, the degradation rate was found to decrease with embedded STF08 and SFO particles showing a degradation rate of 0.2 $x10^{-2}$ $cm^{-1}min^{-1}$. Furthermore, the decrease in degradation rate was also observed when there was an increase in the number of spray cycles.

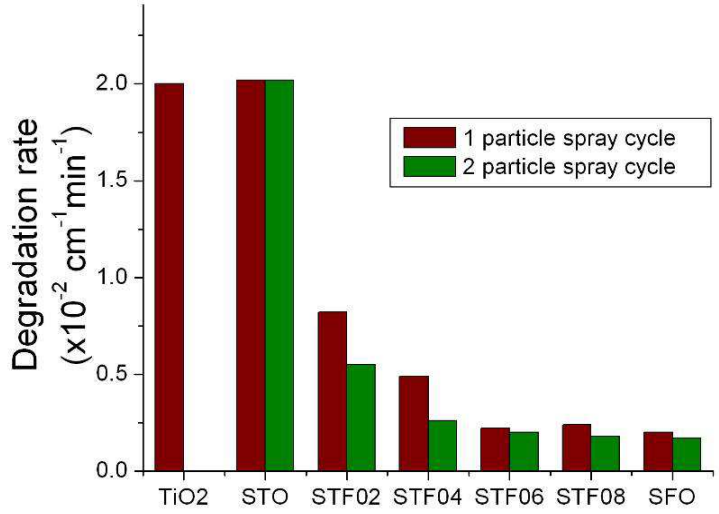

Figure 6.11 Stearic acid degradation under UV illumination by TiO_2 films embedded with $SrTi_{(1-x)}Fe_xO_3$.

Such reduction in photoactivity of $SrTi_{(1-x)}Fe_xO_3$ particle embedded TiO_2 films bored similarity to the Fe_2O_3/TiO_2 couple semiconductor. For Fe_2O_3/TiO_2 semiconductor, several reasons had been proposed to explain the reduction in photocatalytic properties: 1) loss of oxidation power for photogenerated holes [137], 2) recombination centers caused by Fe^{3+} ions [82], and 3) optical screening effect of Fe_2O_3 particles [82]. Optical screening was unlikely to cause any decrease in photoactivity for $SrTi_{(1-x)}Fe_xO_3$ particle films as the particles were located underneath the TiO_2 layer. Thus it could not cause any screening effect to TiO_2 films. For the loss in oxidation power, the valence band position of Fe_2O_3 which was at a lower potential than that of TiO_2. Thus, as photogenerated holes migrated to the valence band of Fe_2O_3, it suffered from a reduction in oxidation power which inadvertently caused the reduction in photoactivity. Similar valence band position for $SrTi_{(1-x)}Fe_xO_3$ had been predicted by Rothschild et al. [82], as such, similar loss

of oxidation power would be expected. In addition to the loss of oxidation power, electron hole pair recombination had been reported to occur at the Fe^{3+} sites. The ease of transfer of electrons to Fe^{3+} ions and the lower bandgap of Fe_2O_3 facilitated the electron hole recombination effect [138]. Similar condition was found in $SrTi_{(1-x)}Fe_xO_3$ particles where its small bandgap and continuous hopping of electrons at Fe^{4+} sites resulted in its recombination effect. Thus, the lower oxidation power of holes and recombination centers in Fe^{4+} ions resulted in the decrease in photoactivity of $SrTi_{(1-x)}Fe_xO_3$ particle embedded TiO_2 films.

6.2.7 Visible light photocatalytic reaction of $SrTi_{(1-x)}Fe_xO_3$ particles embedded in TiO_2 films

Degradation of stearic acid under visible light is presented in Figure 6.12. Despite the long illumination time (7 hr) and the high lamp intensity (10 klux), all the TiO_2 films could not fully decomposed the stearic acid. TiO_2 films embedded with $SrTi_{(1-x)}Fe_xO_3$ particle did not showed obvious visible light photocatalytic effect. This was despite the visible light respond observed with methylene blue and absorption capabilities from the absorbance spectrum. This lack of visible light photocatalytic effect was likely to be cause by lower oxidation power and presence of recombination sites as encountered with the photocatalytic test under UV illumination.

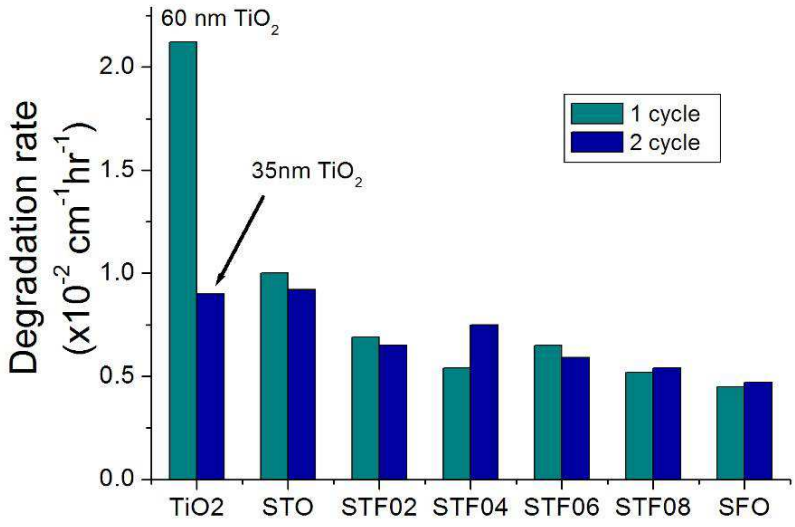

Figure 6.12 Stearic acid degradation under visible light (10k lux) by TiO_2 films embedded with $SrTi_{(1-x)}Fe_xO_3$.

6.3 Conclusion

Four different particles have been embedded in TiO_2 to enhance the photocatalytic effect of the films. Among them, P25 showed the greatest improvement with a 2 times increase in the UV light photoactivity compared to 60 nm of bare TiO_2 film. Anatase showed improvement in photoactivity but the photoactivity did not exceed that of 60 nm TiO_2 film. Rutile, on the other hand, did not show any improvement to its photoactivity. $SrTi_{(1-x)}Fe_xO_3$ particles have the purpose of providing visible light photoactivity to the films, however, caused a decrease in photoactivity under UV illumination. The decrease was caused by a lowered oxidation power and the presence of Fe^{4+} recombination centers. This similarly affected the visible light performance of $SrTi_{(1-x)}Fe_xO_3$ particle embedded TiO_2 films.

Chapter 7: Enhancing photoactivity of TiO_2 films via tin doping

Transition metal doping in TiO_2 has been demonstrated effective for enhancing the photocatalytic property. Among the various metal dopants, tin doping has shown great promise as it helped to suppress recombination of photogenerated electrons and holes. Sn^{4+} dopants introduced an energy state in the bandgap of TiO_2, at 0.4 eV below its conduction band [138]. Furthermore, the incorporation of Sn^{4+} ions promoted the crystallization of rutile phase as cassiterite SnO_2 crystallized in the same tetragonal crystal structure as rutile TiO_2 [139, 140]. The crystallization of rutile phase formed anatase-rutile mixed phase TiO_2 films [97], which could enhance the photoactivity of the films as had been observed in P25 particles. In this chapter, tin was doped into TiO_2 films using AACVD. In addition, TiO_2 films coated on top of tin dioxide film to form the dual TiO_2/SnO_2 layer. The dual layer induced the formation of rutile phase in the TiO_2 layer and improved the photocatalytic property through heterojunction semiconductor effect. The films were tested for their UV light photocatalytic properties. UV-Vis spectroscopy was also carried out to investigate the effects of Sn^{4+} dopants on the absorbance spectrum of the tin-doped TiO_2 films. The amount of Sn^{4+} dopants was determined using XPS while AFM was used to analyze the grain size of the films.

7.1 Tin-doped TiO_2 films deposited via AACVD

Tin-doped TiO_2 films were deposited on soda lime glass pre-coated with SiO_2 barrier layer using AACVD. The precursor used was a mixture of titanium tetraisopropoxide and tetrabutyl tin. The tin-doped TiO_2 films were deposited from a precursor mixture containing 0-10 % by volume of tin precursor. The deposited films were labeled according to the tin precursor concentration used with 1 % precursor concentration named as $Sn01TiO_2$ and 2 % as $Sn02TiO_2$.

7.1.1. XPS analysis of tin-doped TiO_2 films

Figure 7.1 shows the detailed XPS spectra of Ti 2p peaks. The Ti $2p_{3/2}$ and $2p_{1/2}$ peaks were located at 458.7 and 464.4 eV, which was in agreement with reported work [141]. The intensity of these peaks decreased with the increase of tin precursor concentration used for the deposition indicating that a greater amount of Ti^{4+} ions were substituted by the Sn^{4+} ions. In addition, a slight shift to higher binding energy of the Ti 2p XPS spectrum was observed with increasing Sn precursor concentration used. In addition, a slight shift to higher binding energy of the Ti 2p XPS spectrum was observed with increasing Sn precursor. As Sn^{4+} ions is more electronegative than Ti^{4+} ions, the incorporation of Sn^{4+} ions was believed to be responsible for this shift in the binding energy [142].

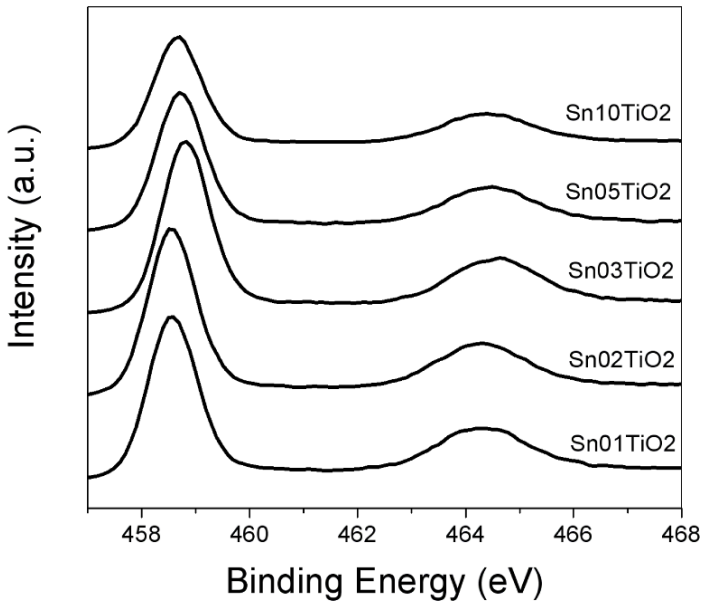

Figure 7.1 High resolution Ti 2p XPS spectra of the tin-doped TiO_2 films.

Figure 7.2 shows the Sn 3d XPS spectra of the deposited films, where Sn $3d_{5/2}$ and $3d_{3/2}$ peaks were located at around 486.5 and 495.3 eV respectively. With increase Sn precursor concentration used for the deposition, a gradual increase of the Sn 3d peaks intensity was observed. This indicated an increased in the Sn content in the deposited films. Figure 7.3 shows the percentage tin concentration of Sn^{4+} ions in the TiO_2 films. The percentage tin concentration was determined from the atomic concentration of Sn^{4+} and Ti^{4+} ions, which was generated from the XPS analysis. This increase in Sn^{4+} ions was expected given that more tetrabutyl tin precursor was available during the deposition process.

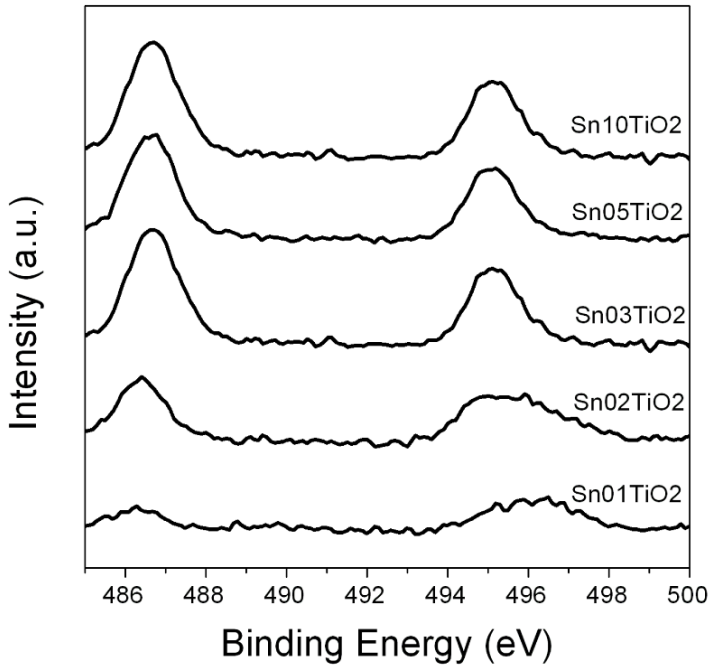

Figure 7.2 High resolution Sn 3d XPS spectra of the tin-doped TiO_2 films.

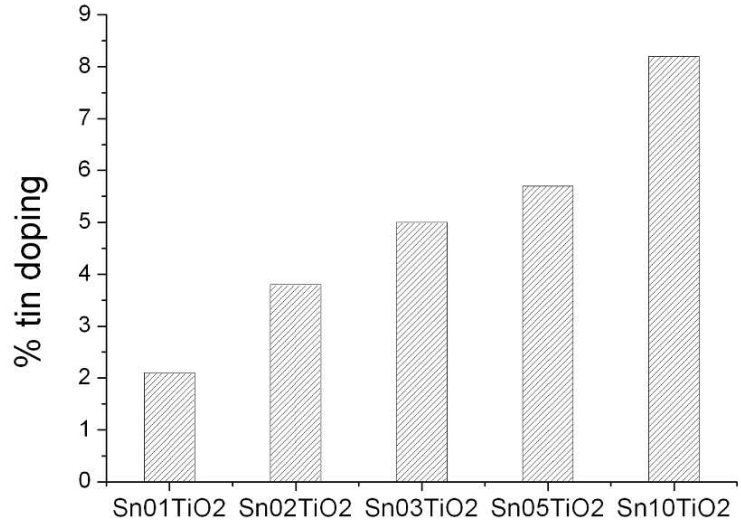

Figure 7.3 Percentage tin dopants in TiO_2 films

7.1.2 XRD analysis of tin-doped TiO_2 films

Figure 7.4 shows the XRD pattern of the deposited tin-doped TiO_2 films. It was found that all the films comprise of only anatase phase. The diffraction peaks observed at 2θ value of 25.9º, 48.9º and 56.0º can be assigned to (101), (200) and (211) planes of anatase TiO_2. No rutile TiO_2 and SnO_2 peaks were detected from the XRD patterns. Generally, with an increase of tin precursor concentration used for film deposition, all the XRD peaks shifted to a lower angle side. This shift in peak position was the result of the substitution of Ti^{4+} ions (ionic radius of 0.68 Å) by the larger Sn^{4+} ions (ionic radius of 0.71 Å), which led to the increase in crystal cell volume and the shift in XRD pattern. The Sn^{4+} ions were more likely to be doped into TiO_2 via substitution mode due to similarity in electronegativity and ionic radius of Sn^{4+} and Ti^{4+} ions [143].

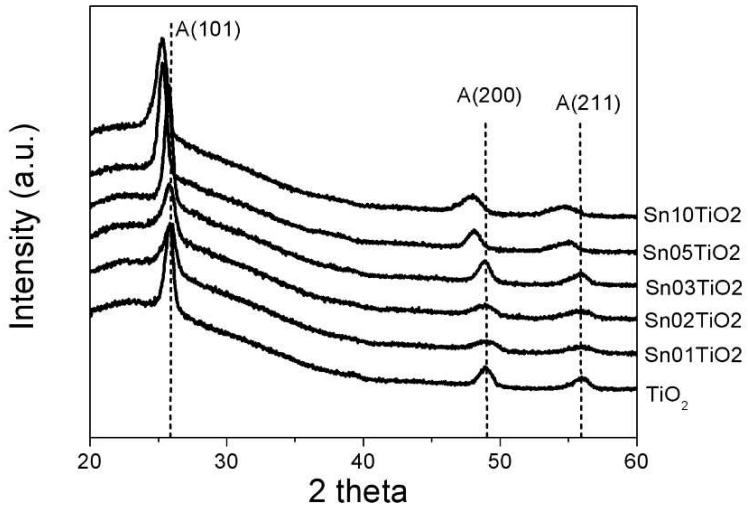

Figure 7.4 XRD analyses of tin-doped TiO_2 films.

7.1.3 Absorption spectrum analysis of tin-doped TiO_2 films

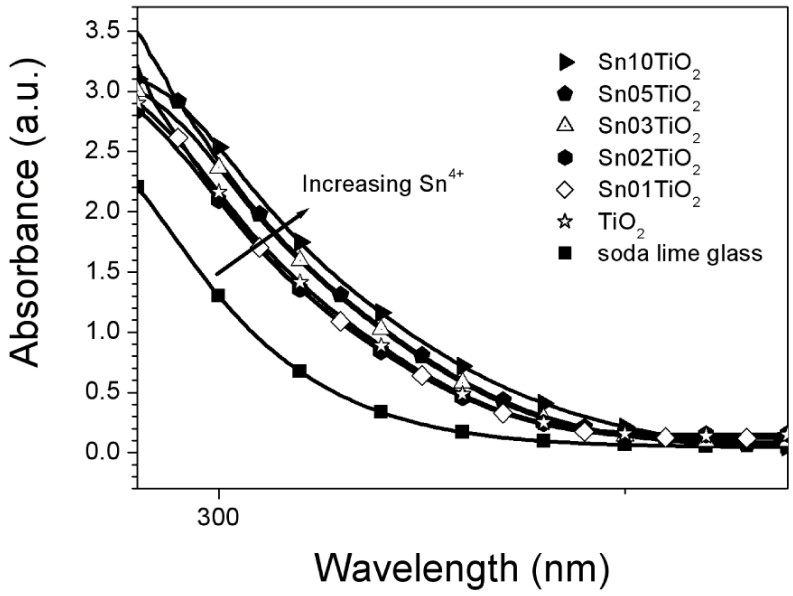

Figure 7.5 Absorbance spectrum of tin-doped TiO_2 films.

UV-Vis absorption spectra of plain soda lime glass, pure TiO_2 coating and tin-doped TiO_2 films are presented in Figure 7.5. Plain soda lime glass showed absorption in the UV region at wavelength below 330 nm. After deposition with TiO_2 films, the absorption edge was shifted to higher wavelength to 350 nm. Bulk anatase TiO_2 has a bandgap of 3.2 eV which allowed the absorption of photons with wavelength below 387 nm. Here, the absorption occurred at a lower wavelength due to quantum effect on nanocrystalline TiO_2 films [97]. With increasing tin content in the coatings, the absorption edge was observed to gradually shift to higher wavelength. This shift in absorption edge was caused by Sn^{4+} dopants, which has an energy level at 0.4 eV below the conduction band of TiO_2 [138]. This suggested that with tin doping, photons with lower energy could be absorbed by TiO_2 films for

photocatalytic reaction. However, the shift in absorption spectrum was insufficient for the absorption of visible light.

7.1.4. Surface topography of tin-doped TiO_2 films

Figure 7.6 shows the surface morphology of the deposited tin-doped TiO_2 films. The grain size of pure TiO_2 films was about 40 nm. With tin doping of up to about 3.8 at.%, grain size remained unchanged. But with further of Sn-doping, grain size increased evidently. The grain size in the $Sn03TiO_2$ was about 50 nm. For $Sn10TiO_2$ coating sample, some of its grains reached a size of more than 80 nm.

The increase in grain size would have a detrimental effect to the photocatalytic property of the films as it reduced the specific surface area of the films. With a decrease in surface area, less active sited were available for the transfer of photogenerated electrons and holes to initiate the degradation process on the organic contamination.

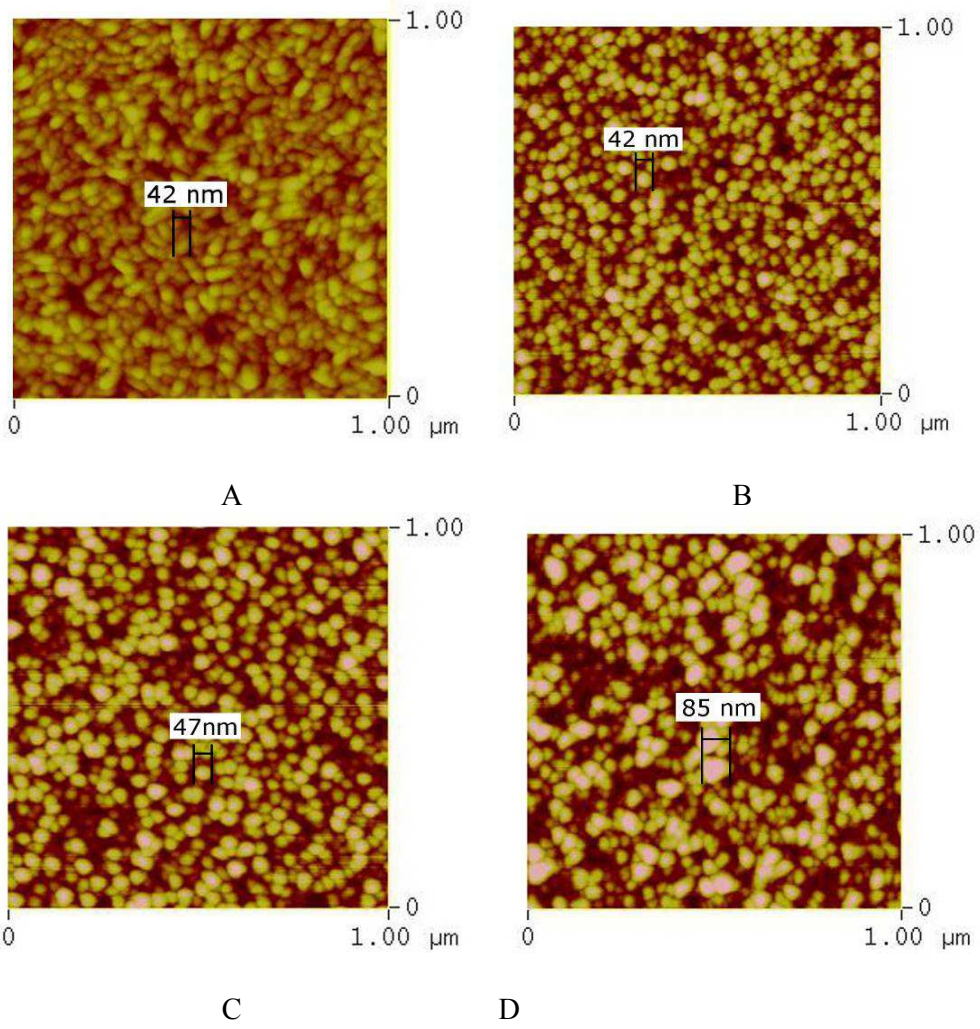

Figure 7.6 AFM images of the tin-doped TiO_2 films. (A) TiO_2, (B) $Sn02TiO_2$, (C) $Sn03TiO_2$ and (D) $Sn10TiO_2$.

7.1.5. Photocatalytic properties of tin-doped TiO_2 films

Degradation rates of stearic acid by tin-doped TiO_2 films are presented in Figure 7.7. At low tin doping concentration, a gradual increase in photoactivity was observed with increasing tin doping concentration. The increase in photoactivity reached a maximum with $Sn02TiO_2$, and this corresponded to 3.8 at.% tin doping in the TiO_2 films. Further increase in tin doping had an adverse effect in the

photoactivity with $Sn10TiO_2$ sample having a photoactivity of only 30 % of the original degradation rate with TiO_2 films.

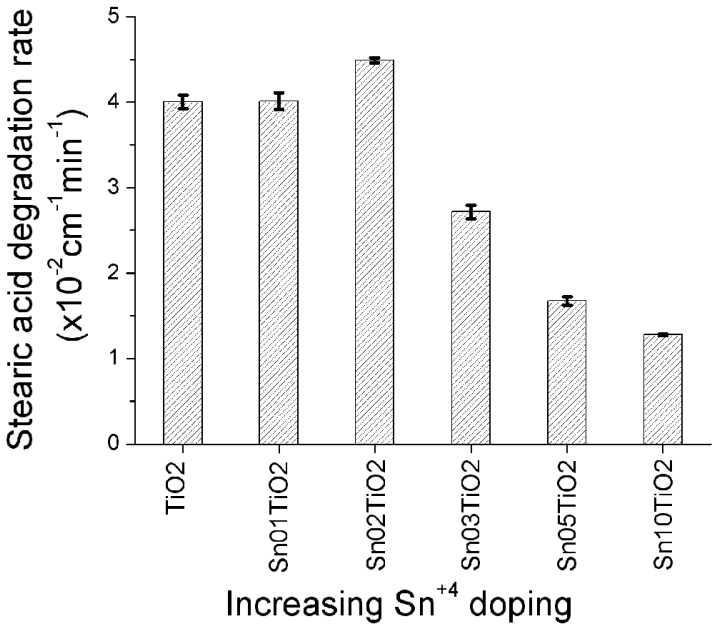

Figure 7.7 Stearic acid degradation rates by various tin-doped TiO_2 films.

The initial increase in photoactivity was the results of Sn^{4+} dopants, which introduced additional band states into the bandgap of TiO_2. The band states were located at 0.4 eV below the conduction band of TiO_2. This allowed photogenerated electrons to be trapped in the Sn band states, thus, resulting in a separation of electrons and holes. With the separation of electrons and holes, its recombination rate decreased. As a result, a greater amount of electrons and holes were available for the photocatalytic reaction process. Thus, a faster stearic acid degradation rate was observed.

At tin-doping concentration of above 5 at.%, the photoactivity of the TiO_2 films decreased. This decrease was the result of both an increase in grain size of the TiO_2

films and the introduction of recombination sites by the Sn^{4+} dopants. The increase in grain size was first observed for $Sn03TiO_2$ sample (Figure 7.6C), which coincided with the decrease in photoactivity. As such, grain size played a major role in determining the photoactivity of the TiO_2 films. In addition to the increase in grain size, the increase in tin dopants led to a decrease in the average distance between the electron trapping sites. As the distance between the trapping sites decreased, the tin dopants act as recombination sites leading to the decrease in photoactivity [144]. Such decrease in photoactivity due to excessive doping in TiO_2 was also reported for other metal ions such as Fe^{3+} [145], Co^{2+} [146], V^{5+} [147] and Mn^{3+} [148]. Choi et al. had compared several metal doped TiO_2 colloids (Fe^{3+}, V^{4+}, V^{3+}, Re^{5+}, Mo^{5+}, Ru^{3+}, Mn^{3+}, Co^{3+}, Rh^{3+}) and found similar decrease in photoactivity with doping concentration of more than 1 at.%. Thus, with the increase in grain size and recombination sites, the photoactivity of TiO_2 films decreased at tin doping levels of more than 5 at.%.

7.2 TiO_2/SnO_2 bilayer films

To induce the formation of rutile phase in TiO_2 films, the TiO_2 films were deposited on top of SnO_2 layer. Due to the similar crystal structure of cassiterite SnO_2 and rutile TiO_2, the SnO_2 layer served as nucleation sites for formation of rutile TiO_2. This led to the presence of mixed anatase and rutile phase in the TiO_2 layer. Through heterojunction semiconductor effect, the photocatalytic property of TiO_2 layer could be enhanced. Here, the deposition and photocatalytic property of TiO_2/SnO_2 bilayer were investigated.

7.2.1 Deposition of TiO_2 on SnO_2

SnO_2 layer was deposited via AACVD system using only tetrabutyl tin as the precursor while TiO_2 films was deposited using APCVD as described in chapter 4. For deposition of SnO_2 layer, oxygen gas was used as the carrier gas instead of N_2 while other parameters remained unchanged. Ellipsometer measurement had showed that 22 nm of SnO_2 were deposited with 10 cycles of APCVD. As such, each deposition cycle deposited 2.2 nm of SnO_2 layer. The TiO_2 films (60 nm) were deposited on 1-4 cycles of SnO_2 layer. The synthesized samples were named according to the number of SnO_2 cycles with TiO2-1SnO2 for 1 cycle of SnO_2 coating and etc.

7.2.2 XRD analysis of SnO_2 and TiO_2 on SnO_2 layer

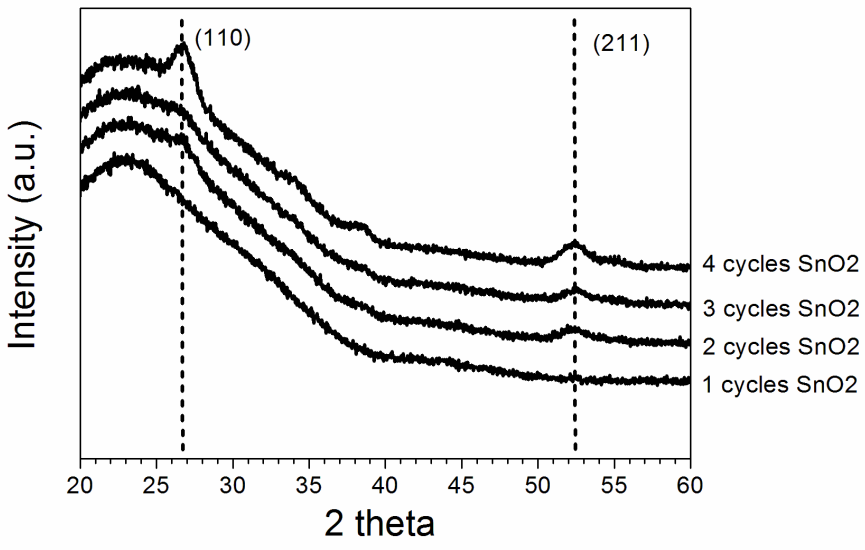

Figure 7.8 XRD analyses of SnO_2 films.

XRD analysis of SnO_2 films (Figure 7.8) showed two small peak at 2 theta = 26.7° and 52.4° which corresponded to (110) and (211) plane of cassiterite SnO_2 phase. The two peaks decreases with lesser number of deposition cycles. For 1 deposition cycle, the two SnO_2 peaks could not be detected by XRD. The low XRD intensity of SnO_2 films showed that the deposited films were very thin. This agreed with ellipsometer measurement where the deposited films were estimated to be <10 nm in thickness.

Despite the thin SnO_2 layers, TiO_2 films deposited on top of SnO_2 layers showed a changed in crystallographic structure. Figure 7.9 shows the XRD analysis of the TiO_2/SnO_2 bilayer films. Previously without any deposited SnO_2 layers, only anatase phase had been detected. Here, both anatase and rutile phase were observed in TiO_2 films. The rutile peak increased in intensity with increased number of SnO_2 deposition cycles. However, at 4 cycles of SnO_2 layers, a decrease in rutile peaks was observed. This decrease was likely to be due to greater interaction between rutile and SnO_2 leading to a broadening and peak shift in the rutile peaks.

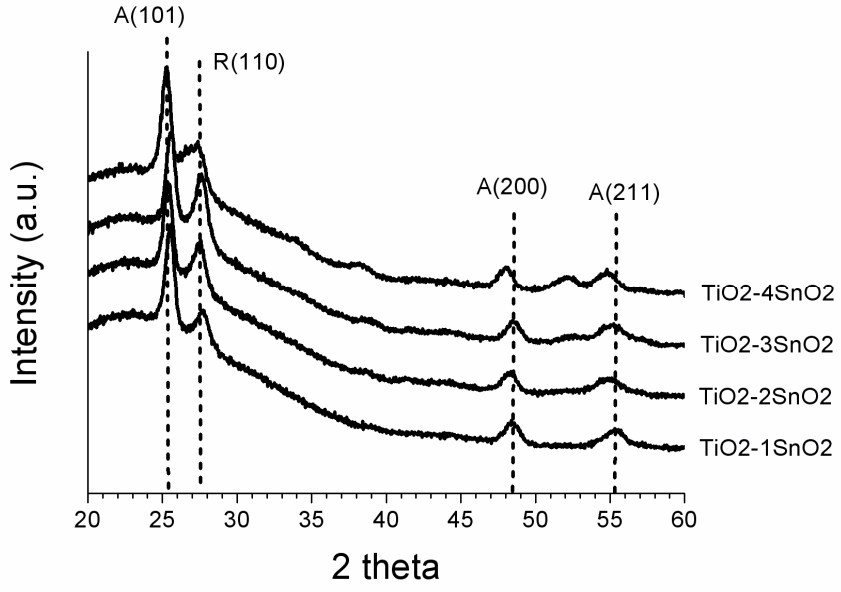

Figure 7.9 XRD analysis of TiO_2 deposited on SnO_2 films.

Table 7.3 presents the weight fraction of anatase and rutile phase for the respective TiO_2/SnO_2 bilayer films. The weight fraction of rutile increased with increasing SnO_2 layer but showed a drop with 4 cycles of SnO_2. The decrease in rutile weight fraction could be caused by the close proximity between of rutile and SnO_2 peaks in the XRD pattern.

samples	% anatase phase	% rutile phase
TiO2-1SnO2	71	29
TiO2-2SnO2	60	40
TiO2-3SnO2	52	48
TiO2-4SnO2	63	37

Table 7.1 Percentage composition of anatase and rutile phase in TiO_2 films deposited on top of SnO_2.

7.2.3 Absorbance spectrum of TiO_2 on SnO_2 layers

Absorbance spectrum of TiO_2/SnO_2 bilayer films are presented in Figure 7.10. The absorbance spectrum of all bilayer films showed a red shift compared to TiO_2 films. The red shift was caused by the presence of rutile phase in the TiO_2 films. The absorbance spectrum showed that all the TiO_2 layers on SnO_2 films were capable of absorbing light with a higher wavelength for photocatalytic reaction and possibly emulating the high photocatalytic property of P25.

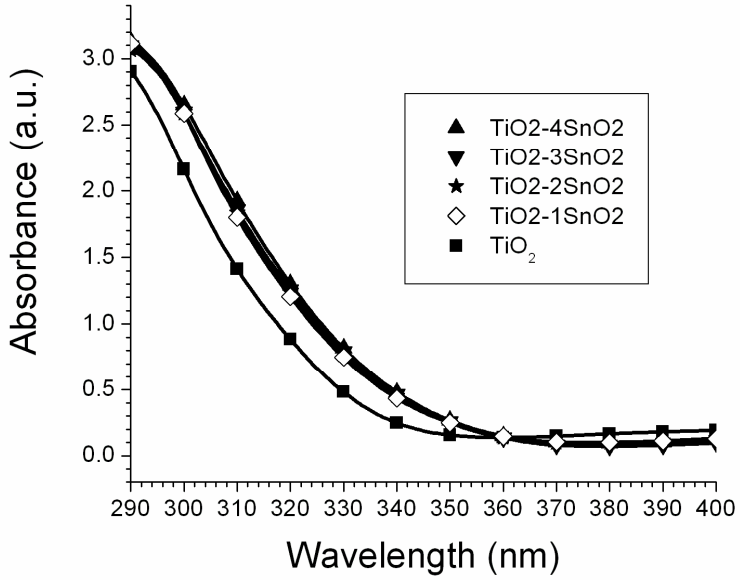

Figure 7.10 UV-Vis absorbance spectrum of TiO_2 films deposited on SnO_2 layers.

7.2.4 Surface topography of TiO_2/SnO_2 films

Surface topography of the various TiO_2/SnO_2 films is shown in Figure 7.11. Compared to the TiO_2 films deposited on glass, the films showed an elongated shape. The grain size was also larger at about 60 nm. For films deposited on 1 to 3 cycles of SnO_2 layers, the films showed similar surface topography with a grain size of about 60 nm in diameter. An increase in grain size was observed for TiO2-4SnO2 which reached to about 90 nm in size. Furthermore, the grains appeared to be round rather than elongated compared to the other films. Such increase in grain size would have a negative impact on the photoactivity.

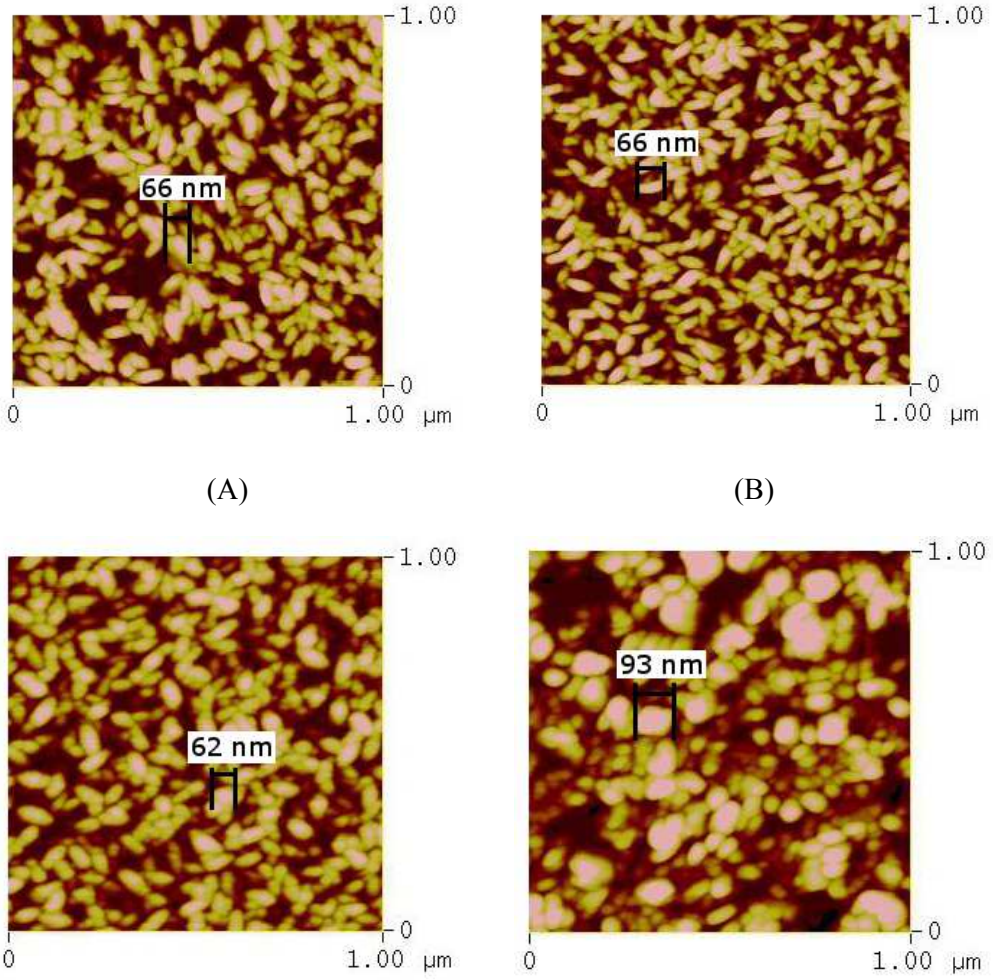

Figure 7.11 AFM images of TiO_2 deposited on SnO_2 layers. (A) TiO2-1SnO2, (B) TiO2-2SnO2, (C) TiO2-3SnO2 and (D) TiO2-4SnO2.

7.2.5 Photocatalytic property of TiO_2/SnO_2 films

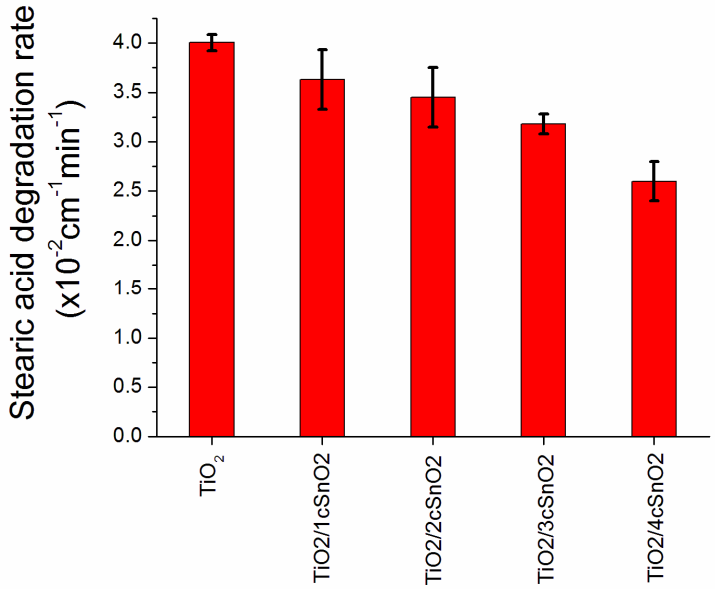

Figure 7.12 Stearic acid degradation rates of TiO_2/SnO_2 films.

Stearic acid degradation rate (Figure 7.12) showed that with increasing SnO_2 layer, a gradual decrease in the photocatalytic reaction rate was observed. The decrease was related to the migration of electrons and holes between TiO_2 and SnO_2 layers. Figure 7.13 shows the bandgap diagram of TiO_2 and SnO_2 layer. In the TiO_2/SnO_2/glass layer, holes were accumulated in the TiO_2 layer and could participate in the photocatalytic reaction process [149]. On the other hand, electrons were accumulated and trapped in the SnO_2 layer. As the SnO_2 layer was sandwiched between TiO_2 and glass, the accumulated electrons were unable to react with absorbed oxygen for photocatalytic reaction [150]. Furthermore, increase in grain size would have caused further decrease in photoactivity of the films. As a result, films deposited on SnO_2 layer suffer from a loss in its photocatalytic property.

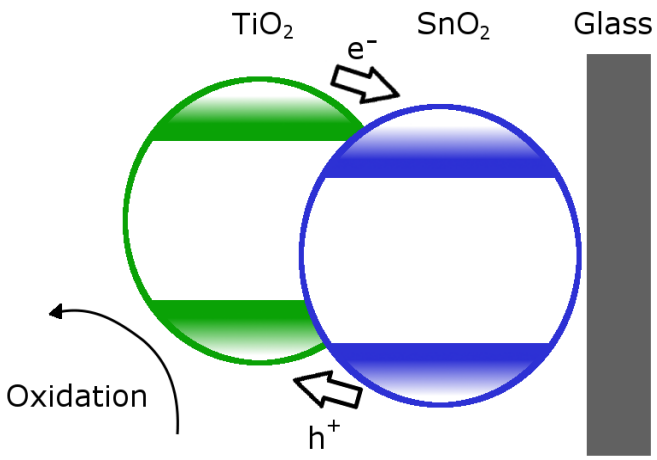

Figure 7.13 Band diagram of TiO_2/SnO_2 films.

Due to the trapping of electrons in the SnO_2 layer, the effect of rutile formation on the photoactivity was less clear. From the XRD analysis, 30-50% of the anatase had been converted into rutile phase. In the previous chapter, Figure 6.6 shows that embedded rutile particles did not enhance the photoactivity of the TiO_2 films. Thus, with a 30-50% conversion of anatase to rutile phase, the photoactivity of the films was expected to decrease by an equal amount. However, Figure 7.12 shows that the decrease in photoactivity was more gradual at 10-26%. This suggested that rutile had a positive effect to the photoactivity. With the effect of trapped electrons in SnO_2 and grain size, the positive heterojunction effect was, however, overshadowed and a net gradual decrease in photoactivity was observed.

7.3 Conclusion

Tin-doped TiO_2 and TiO_2/SnO_2 bilayer films had been deposited. Tin-doped TiO_2 showed an improvement to the photoactivity of TiO_2 at low level of tin doping. The

enhancement was due to the introduction of Sn^{4+} band states in the bandgap of TiO_2, which facilitates the separation of electron hole pairs. On the other hand, TiO_2/SnO_2 showed a mixed phase of anatase and rutile in the TiO_2 films. The heterojunction effect of anatase and rutile was overshadowed by the trapping of electrons in the SnO_2 layer and increase in grain size. Thus, an overall net decrease in photoactivity was observed.

Chapter 8: Conclusion and Recommendations

8.1 Conclusion

In this thesis, the enhancement of photocatalytic property of APCVD deposited TiO_2 films has been reported. The contributions of this research can be summarized as follows.

- Deposition of thin uniform TiO_2 films by APCVD coater. The deposited films showed UV light photocatalytic capability through degradation of stearic acid and ethyl cellulose. An underlying SiO_2 barrier layer was coated which improved the film's photocatalytic property by reducing sodium poisoning. Stearic acid test carried out on 25-90 nm thick TiO_2 films showed saturation of the degradation rate at a film thickness of 60 nm. The deposited TiO_2 films showed good integrity with its photocatalytic effect remaining intact after a 6 months storage period.
- Deteriorative effect of thermal annealing on TiO_2 films. TiO_2 films deposited on quartz glass undergo thermal annealing to initiate a partial phase transformation and achieved a mixed anatase and rutile phase for an expected enhanced photocatalytic effect. The annealing effect, however, resulted in an increase in grain size in the TiO_2 films. Furthermore defects sites, such as OH^- and O^- were formed in the TiO_2 films as Ti ions diffused to the surface and formed new TiO_2 layers. This resulted in a 2 stage decrease in photoactivity of the annealed films where the first stage was

cause by grain growth and defects formation. The second stage was due to the formation of large rutile grains which had limited heterojunction semiconductor effect with anatase films.

- Embedding particles (Anatase, Rutile, P25 and $SrTi_{(1-x)}Fe_xO_3$) into TiO_2 thin films. Particles were embedded into TiO_2 films through particle dispersion spray and APCVD thin film deposition. Among Anatase, Rutile and P25, P25 particles showed the greatest enhancement to the UV light photocatalytic property with 2 times increase in stearic acid degradation rate compared to 60 nm TiO_2 film. Rutile particles showed no improvement in photoactivity due to the large rutile particle size which had limited heterojunction effect with anatase films. Anatase particles, while showing improvement in photoactivity, could not exceed the photoactivity achieved by 60 nm TiO_2 film. $SrTi_{(1-x)}Fe_xO_3$ particles meant to improve the visible light photocatalytic property, however, caused a deterioration of UV photocatalytic effect. The deterioration was due to loss of oxidation power of the generated holes and recombination centers caused by Fe ions. The deterioration in UV light photoactivity also adversely impacted the visible light photoactivity of the films.
- Incorporation of tin into TiO_2 films. Tin was incorporated into TiO_2 through AACVD. The tin dopants did not result in formation of rutile phase but show an improvement in the photoactivity of the films with 3.8 at.% tin dopants. The improvement was due to electron traps which helped to reduce electron hole recombination. Further doping resulted in the formation of recombination centers leading to a decrease in photoactivity.

- Deposition of SnO_2/TiO_2 bilayer photocatalyst. The SnO_2 layer underneath the TiO_2 films induced the formation of rutile phase, leading to the heterojunction semiconductor in the TiO_2 films. However, due to the trapping of electrons in the sandwiched SnO_2 layer, the films showed an overall decrease in the photocatalytic property.

8.2 Recommendations for future studies

The following recommendations are made to extend the research on nanostructure photocatalytic TiO_2 films.

- Patterned bilayer semiconductor thin films. Bilayer heterojunction semiconductor (i.e. TiO_2/SnO_2) led to the trapping of holes or electrons in the sandwich layer between the substrate and the layer exposed to air. Instead, the top TiO_2 layer may be patterned with photolithography to expose the underlying SnO_2 layer as shown in Figure 8.1. This would allow photogenerated charges trapped in underlying layers to participate in the photocatalytic reaction process and achieve higher photocatalytic reaction rate. Tada et al. [149] had reported high photoactivity of patterned TiO_2/SnO_2 bilayer photocatalyst for both gas and liquid phase reaction. While Tada et al. [149] had deposited anatase TiO_2 films on the bilayer semiconductor, further works could be carried out by depositing mixed phase TiO_2 films on the SnO_2 layer. This could be achieved by depositing the TiO_2 films through the APCVD coater as mentioned in Chapter 7.

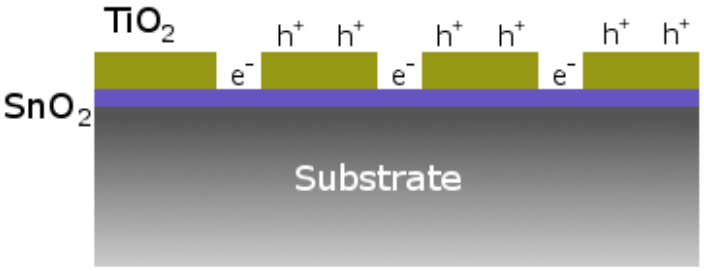

Figure 8.1 Bilayer TiO_2/SnO_2 with exposed regions in the TiO_2 layer.

- Doping of metal ions to reduce the grain size of TiO_2. Metal ions, such as tungsten [151] and aluminum [152], are reported to reduce the grain size of TiO_2 particles. By doping these ions into TiO_2 films, the grain size of TiO_2 films could be preserved or even reduced. Furthermore, through thermal annealing or through co-doping with Sn^{4+} ions, the grain size of anatase could be preserved while that of rutile may be reduced. As such, this would enhance the photocatalytic property of the films through anatase/rutile heterojunction effect or through the addition of Sn^{4+} band states in TiO_2 bandgap.
- Visible light photocatalyst. Most research focuses on fabricating visible light photocatalysts as there were many applications to be exploited. However, while metal and non-metal doping of TiO_2 were used to narrow its bandgap, its photocatalytic efficiency and visible light absorption capability was limited. Further research should concentrate on novel photocatalyst such as $BiVO_4$ [153] or WO_3 [154].
- Deposition on other substrate. TiO_2 films may be deposit with APCVD on substrate such as stainless steel [155]. The TiO_2 coated metal substrate can

be used for in many applications such as self-cleaning/sterilizing hospital equipment, antimicrobial coatings for inclusion in air-conditioning.

- Further photocatalytic test can be conducted on various contaminations such as E.Coli [156] or on volatile organic compounds [157]. This allows the TiO_2 films to be used for applications such as antibacterial coating and indoor air quality control.

Author's Publications

Journals and Conferences

1) **C.S. Chua**, O.K. Tan, M.S. Tse, X. Ding, "Photocatalytic activity of tin-doped TiO_2 film deposited via Aerosol Assisted Chemical Vapor deposition", Thin Solid Films (2013), 10.1016/j.tsf.2012.12.066
2) **C.S. Chua**, X. Fang, X. Chen, O.K. Tan, M.S. Tse, A.M. Soutar, X. Ding, "Effect of annealing temperature on structure and photocatalytic property of Atmospheric pressure chemical vapor deposition TiO_2 film", Chemical Vapor Deposition (submitted)
3) **C.S. Chua**, O.K. Tan, M.S. Tse, A.M. Soutar. "Nanocomposite Films as matrix for Photocatalytic particles", 6th European Meeting on Solar Chemistry and Photocatalysis: Environmental Applications, 13-16 June 2010, Prague, Czech Republic.
4) **C.S. Chua**, O.K. Tan, M.S. Tse, X. Ding. "Photocatalytic activity of tin-doped TiO_2 film deposited via Aerosol Assisted Chemical Vapor Deposition", 6th International Conference on Technological Advances of Thin Films & Surface Coatings, 14-17 July 2012, Singapore.
5) P.Y. Tan, **C.S. Chua**, A. Soutar, O.K. Tan. Barrier coatings on glass for enhanced TiO_2 thin film photocatalytic performance", 6th International Conference on Technological Advances of Thin Films & Surface Coatings, 14-17 July 2012, Singapore.

Bibliography

[1] A. Fujishima, K. Honda, Nature 238/5358 (1972) 37.

[2] M. Ni, M.K.H. Leung, D.Y.C. Leung, K. Sumathy, Renewable & Sustainable Energy Reviews 11/3 (2007) 401.

[3] V. Puddu, H. Choi, D.D. Dionysiou, G.L. Puma, Applied Catalysis B-Environmental 94/3-4 (2010) 211.

[4] W.Y. Su, S.C. Wang, X.X. Wang, X.Z. Fu, J.N. Weng, Surface & Coatings Technology 205/2 (2010) 465.

[5] M. Sokmen, I. Tatlidil, C. Breen, F. Clegg, C.K. Buruk, T. Sivlim, S. Akkan, Journal of Hazardous Materials 187/1-3 (2011) 199.

[6] http://www.pilkingtonselfcleaningglass.co.uk/.

[7] http://www.selfcleaningglass.com/.

[8] D.C. Hurum, A.G. Agrios, K.A. Gray, T. Rajh, M.C. Thurnauer, Journal of Physical Chemistry B 107/19 (2003) 4545.

[9] P. Evans, S. Mantke, A. Mills, A. Robinson, D.W. Sheel, Journal of Photochemistry and Photobiology a-Chemistry 188/2-3 (2007) 387.

[10] J.H. Sun, S.Y. Dong, Y.K. Wang, S.P. Sun, Journal of Hazardous Materials 172/2-3 (2009) 1520.

[11] T. Arai, M. Horiguchi, M. Yanagida, T. Gunji, H. Sugihara, K. Sayama, Chemical Communications/43 (2008) 5565.

[12] L. Jia, D.H. Wang, Y.X. Huang, A.W. Xu, H.Q. Yu, Journal of Physical Chemistry C 115/23 (2011) 11466.

[13] Y. Chen, G.F. Huang, W.Q. Huang, L.L. Wang, Y. Tian, Z.L. Ma, Z.M. Yang, Materials Letters 75 (2012) 221.

[14] A. Mills, S. LeHunte, Journal of Photochemistry and Photobiology a-Chemistry 108/1 (1997) 1.

[15] M. Pera-Titus, V. Garcia-Molina, M.A. Banos, J. Gimenez, S. Esplugas, Applied Catalysis B-Environmental 47/4 (2004) 219.

[16] J.F. Zhu, M. Zach, Current Opinion in Colloid & Interface Science 14/4 (2009) 260.

[17] A.L. Linsebigler, G.Q. Lu, J.T. Yates, Chemical Reviews 95/3 (1995) 735.

[18] B. Neppolian, S. Sakthivel, B. Arabindoo, M. Palanichamy, V. Murugesan, Journal of Environmental Science and Health Part a-Toxic/Hazardous Substances & Environmental Engineering 34/9 (1999) 1829.

[19] A.P. Davis, C.P. Huang, Water Research 25/10 (1991) 1273.

[20] P. Allongue, R. Tenne, Journal of the Electrochemical Society 138/1 (1991) 261.

[21] Y. Bessekhouad, D. Robert, J.V. Weber, Catalysis Today 101/3-4 (2005) 315.

[22] E. Kikuchi, K. Iida, A. Fujishima, K. Itoh, Journal of Electroanalytical Chemistry 351/1-2 (1993) 105.

[23] A. Fujishima, T. Kato, E. Maekawa, K. Honda, Bulletin of the Chemical Society of Japan 54/6 (1981) 1671.

[24] D.S. Muggli, J.T. McCue, J.L. Falconer, Journal of Catalysis 173/2 (1998) 470.

[25] P. Sawunyama, L. Jiang, A. Fujishima, K. Hashimoto, Journal of Physical Chemistry B 101/51 (1997) 11000.

[26] D.W. Chen, A.K. Ray, Applied Catalysis B-Environmental 23/2-3 (1999) 143.

[27] A.H. Boonstra, C. Mutsaers, Journal of Physical Chemistry 79/16 (1975) 1694.

[28] J. Augustynski, Electrochimica Acta 38/1 (1993) 43.

[29] M.C. Xu, Y.K. Gao, E.M. Moreno, M. Kunst, M. Muhler, Y.M. Wang, H. Idriss, C. Woll, Physical Review Letters 106/13 (2011).

[30] B.R. Sankapal, M.C. Lux-Steiner, A. Ennaoui, Applied Surface Science 239/2 (2005) 165.

[31] C.Y. Wu, Y.H. Yue, X.Y. Deng, W.M. Hua, Z. Gao, Catalysis Today 93-5 (2004) 863.

[32] R.I. Bickley, T. Gonzalezcarreno, J.S. Lees, L. Palmisano, R.J.D. Tilley, Journal of Solid State Chemistry 92/1 (1991) 178.

[33] M.R. Hoffmann, S.T. Martin, W.Y. Choi, D.W. Bahnemann, Chemical Reviews 95/1 (1995) 69.

[34] C.B. Almquist, P. Biswas, Journal of Catalysis 212/2 (2002) 145.

[35] D.S. Kim, S.J. Han, S.Y. Kwak, Journal of Colloid and Interface Science 316/1 (2007) 85.

[36] G.H. Tian, H.G. Fu, L.Q. Jing, C.G. Tian, Journal of Hazardous Materials 161/2-3 (2009) 1122.

[37] M. Adachi, Y. Murata, M. Harada, S. Yoshikawa, Chemistry Letters/8 (2000) 942.

[38] H.M. Zhang, C.H. Liang, J. Liu, Z.F. Tian, G.Z. Wang, W.P. Cai, Langmuir 28/8 (2012) 3938.

[39] V. Iliev, D. Tomova, L. Bilyarska, A. Eliyas, L. Petrov, Applied Catalysis B-Environmental 63/3-4 (2006) 266.

[40] G.R. Bamwenda, S. Tsubota, T. Nakamura, M. Haruta, Catalysis Letters 44/1-2 (1997) 83.

[41] S. Sakthivel, M.V. Shankar, M. Palanichamy, B. Arabindoo, D.W. Bahnemann, V. Murugesan, Water Research 38/13 (2004) 3001.

[42] B.L. Zhu, K.R. Li, J. Zhou, S.R. Wang, S.M. Zhang, S.H. Wu, W.P. Huang, Catalysis Communications 9/14 (2008) 2323.

[43] M. Jakob, H. Levanon, P.V. Kamat, Nano Letters 3/3 (2003) 353.

[44] V. Subramanian, E.E. Wolf, P.V. Kamat, Journal of the American Chemical Society 126/15 (2004) 4943.

[45] V. Subramanian, E. Wolf, P.V. Kamat, Journal of Physical Chemistry B 105/46 (2001) 11439.

[46] K.K. Akurati, A. Vital, J.P. Dellemann, K. Michalow, T. Graule, D. Fetti, A. Baiker, Applied Catalysis B-Environmental 79/1-2 (2008) 53.

[47] T.P. Cao, Y.J. Li, C.H. Wang, C.L. Shao, Y.C. Liu, Langmuir 27/6 (2011) 2946.

[48] L.L. Peng, T.F. Xie, Y.C. Lu, H.M. Fan, D.J. Wang, Physical Chemistry Chemical Physics 12/28 (2010) 8033.

[49] Y. Bessekhouad, N. Chaoui, M. Trzpit, N. Ghazzal, D. Robert, J.V. Weber, Journal of Photochemistry and Photobiology a-Chemistry 183/1-2 (2006) 218.

[50] A. Mills, S. Morris, Journal of Photochemistry and Photobiology a-Chemistry 71/3 (1993) 285.

[51] R.R. Bacsa, J. Kiwi, Applied Catalysis B-Environmental 16/1 (1998) 19.

[52] G. Liu, X.X. Yan, Z.G. Chen, X.W. Wang, L.Z. Wang, G.Q. Lu, H.M. Cheng, Journal of Materials Chemistry 19/36 (2009) 6590.

[53] S. Liu, E.Y. Guo, L.W. Yin, Journal of Materials Chemistry 22/11 (2012) 5031.

[54] H. Wang, J.P. Lewis, Journal of Physics-Condensed Matter 18/2 (2006) 421.

[55] G.M. Wang, H.Y. Wang, Y.C. Ling, Y.C. Tang, X.Y. Yang, R.C. Fitzmorris, C.C. Wang, J.Z. Zhang, Y. Li, Nano Letters 11/7 (2011) 3026.

[56] W.Y. Choi, A. Termin, M.R. Hoffmann, Journal of Physical Chemistry 98/51 (1994) 13669.

[57] A. Milis, J. Peral, X. Domenech, J.A. Navio, Journal of Molecular Catalysis 87/1 (1994) 67.

[58] X.W. Zhang, L.C. Lei, Materials Letters 62/6-7 (2008) 895.

[59] J.C. Yu, G.S. Li, X.C. Wang, X.L. Hu, C.W. Leung, Z.D. Zhang, Chemical Communications/25 (2006) 2717.

[60] J.C.S. Wu, C.H. Chen, Journal of Photochemistry and Photobiology a-Chemistry 163/3 (2004) 509.

[61] F. Sayilkan, M. Asiltuerk, P. Tatar, N. Kiraz, S. Sener, E. Arpac, H. Sayilkan, Materials Research Bulletin 43/1 (2008) 127.

[62] S.T. Martin, C.L. Morrison, M.R. Hoffmann, Journal of Physical Chemistry 98/51 (1994) 13695.

[63] R. Asahi, T. Morikawa, T. Ohwaki, K. Aoki, Y. Taga, Science 293/5528 (2001) 269.

[64] H. Nishikiori, Y. Fukasawa, Y. Yokosuka, T. Fujii, Research on Chemical Intermediates 37/8 (2011) 869.

[65] Y. Wang, C.X. Feng, M. Zhang, J.J. Yang, Z.J. Zhang, Applied Catalysis B-Environmental 104/3-4 (2011) 268.

[66] D.Y. Wu, M.C. Long, W.M. Cai, C. Chen, Y.H. Wu, Journal of Alloys and Compounds 502/2 (2010) 289.

[67] Y. Choi, T. Umebayashi, M. Yoshikawa, Journal of Materials Science 39/5 (2004) 1837.

[68] C. Han, M. Pelaez, V. Likodimos, A.G. Kontos, P. Falaras, K. O'Shea, D.D. Dionysiou, Applied Catalysis B-Environmental 107/1-2 (2011) 77.

[69] H. Irie, Y. Watanabe, K. Hashimoto, Journal of Physical Chemistry B 107/23 (2003) 5483.

[70] T. Yamamoto, F. Yamashita, I. Tanaka, E. Matsubara, A. Muramatsu, Materials Transactions 45/7 (2004) 1987.

[71] T. Ihara, M. Miyoshi, M. Ando, S. Sugihara, Y. Iriyama, Journal of Materials Science 36/17 (2001) 4201.

[72] I. Nakamura, N. Negishi, S. Kutsuna, T. Ihara, S. Sugihara, E. Takeuchi, Journal of Molecular Catalysis a-Chemical 161/1-2 (2000) 205.

[73] D.S. Muggli, J.L. Falconer, Journal of Catalysis 191/2 (2000) 318.

[74] N. Wang, D.T. Kong, H.C. He, Powder Technology 207/1-3 470.

[75] U. Sulaeman, S. Yin, T. Sato, Applied Physics Letters 97/10.

[76] T.H. Xie, X. Sun, J. Lin, Journal of Physical Chemistry C 112/26 (2008) 9753.

[77] S. Ahuja, T.R.N. Kutty, Journal of Photochemistry and Photobiology a-Chemistry 97/1-2 (1996) 99.

[78] C.H. Chang, Y.H. Shen, Materials Letters 60/1 (2006) 129.

[79] J.S. Wang, S. Yin, M. Komatsu, T. Sato, Journal of the European Ceramic Society 25/13 (2005) 3207.

[80] Y. Yang, Z.Q. Cao, Y.S. Jiang, L.H. Liu, Y.B. Sun, Materials Science and Engineering B-Solid State Materials for Advanced Technology 132/3 (2006) 311.

[81] M. Ghaffari, P.Y. Tan, M.E. Oruc, O.K. Tan, M.S. Tse, M. Shannon, Catalysis Today 161/1 (2011) 70.

[82] A. Rothschild, S.J. Litzelman, H.L. Tuller, W. Menesklou, T. Schneider, E. Ivers-Tiffee, Sensors and Actuators B-Chemical 108/1-2 (2005) 223.

[83] C.J. Tavares, S.M. Marques, L. Rebouta, S. Lanceros-Mendez, V. Sencadas, C.M. Costa, E. Alves, A.J. Fernandes, Thin Solid Films 517/3 (2008) 1161.

[84] S. Costacurta, G. Dal Masco, R. Gallo, M. Guglielmi, G. Brusatin, P. Falcaro, Acs Applied Materials & Interfaces 2/5 (2010) 1294.

[85] A. Mills, S.K. Lee, A. Lepre, I.P. Parkin, S.A. O'Neill, Photochemical & Photobiological Sciences 1/11 (2002) 865.

[86] A. Mills, J.S. Wang, M. Crow, G. Taglioni, L. Novella, Journal of Photochemistry and Photobiology a-Chemistry 187/2-3 (2007) 370.

[87] A. Mills, G. Hill, M. Crow, S. Hodgen, Journal of Applied Electrochemistry 35/7-8 (2005) 641.

[88] M. Vergohl, H. Althues, P. Frach, D. Glob, T. Graumann, C. Hubner, F. Neumann, T. Neubert, G. Schottner, D.K. Song, Vakuum 23 (2011) 17.

[89] H.O. Pierson, Handbook of Chemical Vapor Deposition - Principles, Technology and Applications Noyes Publications, Norwich, NY, 1999.

[90] C.W. Pearce, "Epitaxy," VLSI Technology, McGraw-Hill Book Co., New York, 1983.

[91] I. Parkin, M. Wilson, R. Palgrave Patent No. US 2009/0147370 A12009.

[92] X.H. Hou, K.L. Choy, Chemical Vapor Deposition 12/10 (2006) 583.

[93] R.G. Palgrave, I.P. Parkin, Journal of the American Chemical Society 128/5 (2006) 1587.

[94] U. Qureshi, C.W. Dunnill, I.P. Parkin, Applied Surface Science 256/3 (2009) 852.

[95] U. Qureshi, C. Blackman, G. Hyett, I.P. Parkin, European Journal of Inorganic Chemistry/10 (2007) 1415.

[96] G. Battaglin, Nuclear Instruments & Methods in Physics Research Section B-Beam Interactions with Materials and Atoms 116/1-4 (1996) 102.

[97] P.M. Kumar, S. Badrinarayanan, M. Sastry, Thin Solid Films 358/1-2 (2000) 122.

[98] E.M.V. Hoek, S. Bhattacharjee, M. Elimelech, Langmuir 19/11 (2003) 4836.

[99] H.L. Liu, B.Y. Chen, Y.W. Lan, Y.C. Cheng, Applied Microbiology and Biotechnology 62/4 (2003) 414.

[100] J. Bisschop, D.K. Dysthe, C.V. Putnis, B. Jamtveit, Geochimica Et Cosmochimica Acta 70/7 (2006) 1728.

[101] G. Poletti, E. Orsini, A. Raffaele-Addamo, C. Riccardi, E. Selli, Applied Surface Science 219/3-4 (2003) 311.

[102] S.M. Zhu, W.G. Fahrenholtz, G.E. Hilmas, Journal of the European Ceramic Society 27/4 (2007) 2077.

[103] A. Ceylan, C.C. Baker, S.K. Hasanain, S.I. Shah, Journal of Applied Physics 100/3 (2006).

[104] I. Doron-Mor, Z. Barkay, N. Filip-Granit, A. Vaskevich, I. Rubinstein, Chemistry of Materials 16/18 (2004) 3476.

[105] G. Costrini, J.J. Coleman, Journal of Applied Physics 57/6 (1985) 2249.

[106] T. Ohno, K. Sarukawa, M. Matsumura, New Journal of Chemistry 26/9 (2002) 1167.

[107] M. Lazzeri, A. Vittadini, A. Selloni, Physical Review B 65/11 (2002).

[108] H. Yoshiki, T. Mitsui, Surface & Coatings Technology 202/22-23 (2008) 5266.

[109] H.G. Yu, S.C. Lee, C.H. Ao, J.G. Yu, Journal of Crystal Growth 280/3-4 (2005) 612.

[110] Y. Paz, A. Heller, Journal of Materials Research 12/10 (1997) 2759.

[111] A. Fujishima, T.N. Rao, D.A. Tryk, Electrochimica Acta 45/28 (2000) 4683.

[112] E. Aubry, M.N. Ghazzal, V. Demange, N. Chaoui, D. Robert, A. Billard, Surface & Coatings Technology 201/18 (2007) 7706.

[113] J.G. Yu, X.J. Zhao, Materials Research Bulletin 35/8 (2000) 1293.

[114] H. Tada, M. Tanaka, Langmuir 13/2 (1997) 360.

[115] T. Ohno, K. Sarukawa, K. Tokieda, M. Matsumura, Journal of Catalysis 203/1 (2001) 82.

[116] C. Su, B.Y. Hong, C.M. Tseng, Catalysis Today 96/3 (2004) 119.

[117] J.Y. Kim, H.S. Jung, J.H. No, J.R. Kim, K.S. Hong, Journal of Electroceramics 16/4 (2006) 447.

[118] G.A. Battiston, R. Gerbasi, M. Porchia, A. Marigo, Thin Solid Films 239/2 (1994) 186.

[119] M.D. Wiggins, M.C. Nelson, C.R. Aita, Journal of Vacuum Science & Technology a-Vacuum Surfaces and Films 14/3 (1996) 772.

[120] J.C. Dupin, D. Gonbeau, P. Vinatier, A. Levasseur, Physical Chemistry Chemical Physics 2/6 (2000) 1319.

[121] L. Miao, P. Jin, K. Kaneko, A. Terai, N. Nabatova-Gabain, S. Tanemura, Applied Surface Science 212 (2003) 255.

[122] E. Konstantinova, J. Weidmann, T. Dittrich, Journal of Porous Materials 7/1-3 (2000) 389.

[123] T. Berger, M. Sterrer, O. Diwald, E. Knozinger, D. Panayotov, T.L. Thompson, J.T. Yates, Journal of Physical Chemistry B 109/13 (2005) 6061.

[124] R. Hengerer, B. Bolliger, M. Erbudak, M. Gratzel, Surface Science 460/1-3 (2000) 162.

[125] M. Bowker, R.A. Bennett, Journal of Physics-Condensed Matter 21/47 (2009).

[126] R.E. Tanner, Y. Liang, E.I. Altman, Surface Science 506/3 (2002) 251.

[127] I.E. Grey, N.C. Wilson, Journal of Solid State Chemistry 180/2 (2007) 670.

[128] M.A. Henderson, Surface Science Reports 66/6-7 (2011) 185.

[129] J.M. Coronado, A.J. Maira, J.C. Conesa, K.L. Yeung, V. Augugliaro, J. Soria, Langmuir 17/17 (2001) 5368.

[130] K.L. Yeung, A.J. Maira, J. Stolz, E. Hung, N.K.C. Ho, A.C. Wei, J. Soria, K.J. Chao, Journal of Physical Chemistry B 106/18 (2002) 4608.

[131] J. Nowotny, T. Bak, M.K. Nowotny, L.R. Sheppard, Journal of Physical Chemistry B 110/37 (2006) 18492.

[132] P.A. DeSario, M.E. Graham, R.M. Gelfand, K.A. Gray, Thin Solid Films 519/11 (2011) 3562.

[133] A. Mattsson, M. Leideborg, K. Larsson, G. Westin, L. Osterlund, Journal of Physical Chemistry B 110/3 (2006) 1210.

[134] R.A. Spurr, H. Myers, Analytical Chemistry 29/5 (1957) 760.

[135] T. Ohno, K. Tokieda, S. Higashida, M. Matsumura, Applied Catalysis a-General 244/2 (2003) 383.

[136] Y.J. Chen, D.D. Dionysiou, Applied Catalysis B-Environmental 62/3-4 (2006) 255.

[137] M.I. Litter, J.A. Navio, Journal of Photochemistry and Photobiology a-Chemistry 84/2 (1994) 183.

[138] E.J. Wang, T. He, L.S. Zhao, Y.M. Chen, Y.A. Cao, Journal of Materials Chemistry 21/1 (2011) 144.

[139] X.Z. Ding, Z.A. Qi, Y.Z. He, Nanostructured Materials 4/6 (1994) 663.

[140] S. Mahanty, S. Roy, S. Sen, Journal of Crystal Growth 261/1 (2004) 77.

[141] S.G. Seong, E.J. Kim, Y.S. Kim, K.E. Lee, S.H. Hahn, Applied Surface Science 256/1 (2009) 1.

[142] M. Xu, P. Da, H. Wu, D. Zhao, G. Zheng, Nano Letters 12/3 (2012) 1503.

[143] Y.A. Cao, W.S. Yang, W.F. Zhang, G.Z. Liu, P.L. Yue, New Journal of Chemistry 28/2 (2004) 218.

[144] S.Z. Chen, P.Y. Zhang, D.M. Zhuang, W.P. Zhu, Catalysis Communications 5/11 (2004) 677.

[145] K.T. Ranjit, B. Viswanathan, Journal of Photochemistry and Photobiology a-Chemistry 108/1 (1997) 79.

[146] M. Iwasaki, M. Hara, H. Kawada, H. Tada, S. Ito, Journal of Colloid and Interface Science 224/1 (2000) 202.

[147] D.E. Gu, B.C. Yang, Y.D. Hu, Catalysis Letters 118/3-4 (2007) 254.

[148] Y.H. Xu, B. Lei, L.Q. Guo, W.Y. Zhou, Y.Q. Liu, Journal of Hazardous Materials 160/1 (2008) 78.

[149] H. Tada, A. Hattori, Y. Tokihisa, K. Imai, N. Tohge, S. Ito, Journal of Physical Chemistry B 104/19 (2000) 4585.

[150] Y. Cao, X.T. Zhang, W.S. Yang, H. Du, Y.B. Bai, T.J. Li, J.N. Yao, Chemistry of Materials 12/11 (2000) 3445.

[151] C. Garzella, E. Comini, E. Bontempi, L.E. Depero, C. Frigeri, G. Sberveglieri, Sensors and Actuators B-Chemical 83/1-3 (2002) 230.

[152] L.Y. Shi, C.Z. Li, A.P. Chen, Y.H. Zhu, D.Y. Fang, Chemical Engineering Journal 84/3 (2001) 405.

[153] M.D. Han, X.F. Chen, T. Sun, O.K. Tan, M.S. Tse, Crystengcomm 13/22 (2011) 6674.

[154] J. Kim, C.W. Lee, W. Choi, Environmental Science & Technology 44/17 (2010) 6849.

[155] P. Evans, M.E. Pemble, D.W. Sheel, Chemistry of Materials 18/24 (2006) 5750.

[156] A.C. de Souza Cordeiro, S.G.F. Leite, M. Dezotti, Quimica Nova 27/5 (2004) 689.

[157] S.B. Kim, S.C. Hong, Applied Catalysis B-Environmental 35/4 (2002) 305.